UNIVERSIDAD POLITÉCNICA DE MADRID
Escuela Técnica Superior de Ingeniería Aeronáutica y del Espacio

Models for topological optimization of structures by additive manufacturing and their application to acoustic devices

D O C T O R A L T H E S I S

Submitted for the degree of Doctor by:

María Blanca Boado Cuartero
Máster Universitario en Sistemas Espaciales

Madrid, 2025

UNIVERSIDAD POLITÉCNICA DE MADRID
Escuela Técnica Superior de Ingeniería Aeronáutica y del Espacio

Doctoral Degree in Aerospace Engineering

Models for topological optimization of structures by additive manufacturing and their application to acoustic devices

D O C T O R A L T H E S I S

Submitted for the degree of Doctor by:

María Blanca Boado Cuartero
Máster Universitario en Sistemas Espaciales

Under the supervision of:
Dr. Javier Pérez Álvarez
Dr. Elena Roibás Millán

Madrid, 2025

Title: Models for topological optimization of structures by additive manufacturing and their application to acoustic devices

Author: María Blanca Boado Cuartero

Doctoral Programme: Aerospace Engineering

Thesis Supervision:

Dr. Javier Pérez Álvarez, Doctor en Ingeniería Aeroespacial, Universidad Politécnica de Madrid(Supervisor)

Dr. Elena Roibás Millán, Doctora en Ingeniería Aeroespacial, Universidad Politécnica de Madrid(Co-supervisor)

External Reviewers:

Thesis Defense Committee:

Thesis Defense Date:

To my parents, thank you for your endless encouragement, your love and patience kept me grounded through the many ups and downs.

To Rafa, you are greatly missed.

Acknowledgement

First and foremost, I would like to express my deepest gratitude to my supervisors, Dr. Javier Pérez Álvarez and Dr. Elena Roibás Millán, for their continuous support, invaluable advice, and guidance throughout my doctoral journey.

Special thanks to María Jesús Casati and the Graphic Design Department, and to Pablo Rodriguez and the Materials Department at E.T.S.I.A.E., whose collaboration made the research process possible, both in the manufacturing of the samples and the mechanical testings.

To the researchers of CSIC, Francisco Hidalgo and Alvaro Espinoza, thank you for allowing me to use the facilities and helping me do the acoustic tests.I am equally grateful to Santiago Pindado for his insightful feedback and suggestions, which helped refine my research.

I'm grateful to my colleagues from IDR, to María José and the people of administration, for their help in all these years we have worked together, even before I started my PhD. You have shown me kindness and made me feel at home.

To my friends and colleagues, especially Sergio, Ángel, Carlos, Alejandro, and David, and to those who no longer work in the university, Laura and Miki. Thank you all for the laughter and shared moments that kept me going during challenging times, for hearing my complaints and offering your support.

Abstract

In the space industry, minimizing weight is essential for reducing launch costs and improving fuel efficiency. However, lighter structures have lower stiffness, making them more susceptible to vibroacoustic excitation during rocket launches, which can cause mechanical stress and potential damage. To mitigate this, absorbing materials are commonly applied in the launch vehicle fairing to convert acoustic energy into heat, reducing sound transmission and protecting sensitive payloads. However, this solution increases mass and volume, creating a trade-off. Microperforated panels (MPPs) have emerged as a promising alternative. These panels, made from metal, plastic, or wood, feature tiny perforations (0.1–1 mm in diameter) that dissipate sound energy through frictional losses, acting like Helmholtz resonators to enhance absorption at specific frequencies. While effective, MPPs are costly and require complex manufacturing. To address this, researchers are exploring 3D printing, which offers weight, time, and cost savings while enabling intricate designs. However, material selection remains a challenge due to mechanical property limitations and outgassing concerns in aerospace applications. In the past decade, extensive research has been conducted on materials suitable for aerospace applications, one of them being ULTEM™. This material is a high-performance polymer widely utilized in aerospace due to its exceptional strength, durability, and heat resistance. This thesis aims to apply the 3D fabrication techniques, using materials certified for space applications, for the fabrication of MPPs, looking for characteristics such as speed of fabrication, precision, and low cost, for different topologies of the resulting structure. The first part of this dissertation analyzes the mechanical properties of the materials through tensile, flexural, compression, and Charpy impact tests, as polymers are anisotropic, and their properties can change easily. The mechanical tests show interesting results, with the samples obtaining a lower elastic modulus than in the datasheet, but a similar or higher strength. The samples with the best overall mechanical properties were those printed on-edge at a 45-degree angle, which matches the datasheet. The second part is the acoustic test performed on printed samples to study their absorption coefficient. When performing these tests, other issues arose involving the quality of the print. The material used can only be used with an industrial printer that limits the user's input in the printing process, which led to some of the perforations coming out obstructed and the diameters being smaller than the nominal values. The comparison of their performance with the theoretical curve was not ideal, even after adjusting the parameters and equations to take into account the porosity and other parameters. This led to the decision to print the acoustic test samples with two other materials: PEEK and ceramic resin. The PEEK samples showed the same issues as ULTEM™ in the quality of the print, but the ceramic resin samples used another additive manufacturing fabrication method and the perforations were of better quality and precision, only slightly oval. This also meant a better acoustic absorption performance than the other two materials, although they still differ from the theoretical curves. Overall, even with the issues, all three materials show good absorption capabilities and a broad peak without requiring a small perforation diameter. With time, with the creation of better printers, FDM could be a great alternative, but resin and CNC appear to be a better option at the moment for the production of MPPs, while FDM could also be a great alternative to metals in other types of acoustic vibration reducers, like Helmholtz resonators, for their good mechanical properties of ULTEM™ and capability for complex geometries.

Resumen

En la industria espacial, minimizar el peso es clave para reducir costes de lanzamiento y mejorar la eficiencia del combustible. Sin embargo, las estructuras más ligeras tienen menor rigidez, lo que las hace más vulnerables a la excitación vibroacústica durante el lanzamiento, generando tensiones mecánicas y posibles daños. Para mitigarlo, se aplican materiales absorbentes en el carenado del vehículo, que convierten la energía acústica en calor, reduciendo la transmisión del sonido y protegiendo las cargas útiles. Sin embargo, esta solución aumenta la masa y el volumen, lo que supone una limitación. Los paneles microperforados (MPP) han surgido como una alternativa prometedora. Estos paneles, fabricados en metal, plástico o madera, contienen pequeñas perforaciones (0,1-1 mm) que disipan la energía sonora mediante pérdidas por fricción, actuando como resonadores de Helmholtz para mejorar la absorción en ciertas frecuencias. Aunque eficaces, los MPP son costosos y su fabricación es compleja. Para abordar este problema, se ha propuesto la impresión 3D, que reduce peso, tiempo y costes, además de permitir diseños más complejos. No obstante, la selección de materiales sigue siendo un desafío debido a sus propiedades mecánicas y los problemas de desgasificación en aplicaciones espaciales. En los últimos años, se ha investigado el uso de materiales adecuados para el sector aeroespacial, destacando ULTEM™, un polímero de alto rendimiento utilizado por su resistencia, durabilidad y tolerancia al calor. Esta tesis busca aplicar la impresión 3D con materiales certificados para fabricar MPP, evaluando velocidad de producción, precisión y coste en distintas topologías. La primera fase analiza las propiedades mecánicas de los materiales mediante ensayos de tracción, flexión, compresión e impacto Charpy, ya que los polímeros son anisótropos y sus propiedades pueden variar. Los resultados mostraron que las muestras impresas de canto en ángulo de 45 grados ofrecieron las mejores propiedades mecánicas globales, en línea con la ficha técnica. Sin embargo, el módulo elástico fue menor al esperado, aunque la resistencia fue similar o superior. La segunda fase evaluó el coeficiente de absorción acústica de los MPP impresos. Surgieron problemas con la calidad de impresión: algunas perforaciones estaban obstruidas y los diámetros eran menores a los valores nominales. Como el material solo podía imprimirse con una impresora industrial que limita la intervención del usuario, no se pudieron optimizar del todo los parámetros de impresión. En consecuencia, el rendimiento acústico no coincidió con la teoría, incluso tras ajustar ecuaciones para considerar la porosidad y otros parámetros. Para mejorar la precisión de las perforaciones, se fabricaron muestras con otros materiales: PEEK y resina cerámica. Las muestras de PEEK mostraron problemas similares a ULTEM™, pero las de resina cerámica, producidas con otro método de impresión, lograron perforaciones más precisas, aunque ligeramente ovaladas. Esto mejoró el rendimiento de absorción acústica en comparación con los otros dos materiales, aunque con desviaciones respecto a las curvas teóricas. A pesar de los desafíos, los tres materiales mostraron buena capacidad de absorción con un pico amplio sin necesidad de perforaciones pequeñas. Sin embargo, la calidad de impresión sigue siendo un obstáculo para la fabricación de MPP mediante impresión 3D. Con mejores impresoras en el futuro, la tecnología FDM podría ser una opción viable, aunque actualmente la impresión en resina y el mecanizado CNC parecen más adecuados para producir MPP. Por otro lado, FDM podría ser una alternativa eficiente al uso de metales en dispositivos de reducción de vibraciones acústicas, como resonadores de Helmholtz, gracias a las propiedades mecánicas del ULTEM™ y su capacidad para geometrías complejas.

Table of Contents

Acknowledgement v
Abstract vi
Resumen vii
List of Figures x
List of Tables xiv
Abbreviations and acronyms xvii

1 Introduction **1**
1.1 Objectives 8

2 State of the art **11**
2.1 Sound Absorption techniques for vibroacoustic loads mitigation 11
2.1.1 Noise level reduction at the launchpad 11
2.1.2 Sound absorption materials and microperforated panels 13
2.1.3 Other structural vibration reduction techniques 16
Passive isolation systems 16
Active isolation systems 18
2.2 Additive Manufacturing: Basic Concepts 20
2.2.1 Fused Deposition Modeling 20
Materials 21
Hardware 23
Software 24
Future 26
2.2.2 High-performance polymers 27

3 Additive Manufactured Polymers: Structural Characterization **31**
3.1 Testing methods and procedure 32
3.1.1 Tensile Tests 33
3.1.2 Bending Tests 33
3.1.3 Compression Tests 34
3.1.4 Charpy Impact Tests 34
3.2 Testing instrumentation and specimens 36
3.3 Results and Analysis 38
3.3.1 Tensile test 38
ULTEM™ 9085 38

ULTEM™ 1010 . . . 41
3.3.2 Flexural test . . . 43
ULTEM™ 9085 . . . 43
ULTEM™ 1010 . . . 44
3.3.3 Compression test . . . 45
ULTEM™ 9085 . . . 45
ULTEM™ 1010 . . . 47
3.3.4 Charpy Impact Test . . . 48
ULTEM™ 9085 . . . 48
ULTEM™ 1010 . . . 50
3.3.5 Fractures in ULTEM™ 1010 . . . 51
3.3.6 Differences with the datasheet . . . 52

4 Analytical model for microperforated panels 53
4.1 The model of Maa . . . 53
4.1.1 End corrections to the Maa analytical model . . . 56
4.1.2 The microperforated panel absorber . . . 58
4.1.3 Overperforation effects: the equivalent fluid model . . . 61
4.1.4 The double layer MPP . . . 62
4.2 Analytical solutions of the Maa equation . . . 63
Comparison . . . 64
Finding optimized solutions . . . 68
4.2.1 Panel design parameter iterations . . . 70
4.3 Acoustic tests . . . 72
4.3.1 Methodology . . . 72
4.3.2 Results . . . 75

5 Discussion 85

6 Conclusions and future work 107

Referencias 111

List of Figures

1.1 Space launch vehicles. From left to right: Nuri (KSLV-II), Starship, Ariane-4 and Atlas-Centaur. . . . 2
1.2 Vibroacoustic metamaterial for launcher, from the Fraunhofer LBF [25]. . . . 4
1.3 Comparison of manufacturing cost as a function of the part complexity [50]. 7

2.1 Water Deluge test from NASA. . . . 12
2.2 Flame deflector from NASA . . . 12
2.3 Diagram of a Helmholtz resonator. . . . 13
2.4 Diagram of an MPP. . . . 14
2.5 Sketch of two examples of microslit MPPs. . . . 14
2.6 Sketch of a MPP with irregular holes. . . . 15
2.7 Design parameters of the MPP configuration: cavity diameter (d), panel thickness (t) and cavity distance (D). . . . 16
2.8 Example of a Stewart platform [118]. . . . 17
2.9 Proposed quasi-zero stiffness platform [121]. . . . 18
2.10 Example of a VCM actuator. . . . 19
2.11 Examples active isolators . . . 20
2.12 Components printed with ULTEM ™ 9085 and 1010, from STRATASYS. . . . 21
2.13 Components printed with PEEK, from Roboze. . . . 21
2.14 Components printed with carbon fiber reinforced filament. . . . 22
2.15 Example of a 3D printed PCB with conductive filament. . . . 22
2.16 Example of a 3D printed dual extrusion system. . . . 23
2.17 Quad extrusion system. . . . 24
2.18 Large format printers. . . . 24
2.19 Different types of extruders. In both figures (A) extruder (B) filament (C) hotend (D) nozzle . . . 25
2.20 Illustration of the monitoring and self-correction system designed by Goh [167] 26
2.21 Classification of thermoplastics . . . 28

3.1 Componets made of ABS in the HERCCULES experiment . . . 32
3.2 Tensile test samples' dimensions (mm). . . . 33
3.3 Flexural samples' dimensions (mm). . . . 34
3.4 Flexural test sample positioning [211]. . . . 34
3.5 Compression samples' dimensions (mm). . . . 35
3.6 Charpy Impact test samples' dimensions (mm). . . . 35

3.7 Charpy impact test configuration [214]. 35
3.8 Sample layer orientation and direction. 36
3.9 Fortus 450mc (left) and 900mc (right) from Stratasys. 37
3.10 ULTEM™ 9085 average results and standard deviation for all 1A samples. . 39
3.11 ULTEM™ 9085 average results and standard deviation for all 1B samples. . 40
3.12 ULTEM™ 9085 average results and standard deviation for all 5A samples. . 40
3.13 On-edge 5A samples showing the deformation suffered during testing. 41
3.14 ULTEM™ 1010 average results and standard deviation for all 1A samples. . 43
3.15 ULTEM™ 1010 average results and standard deviation for all 1B samples. . 44
3.16 ULTEM™ 1010 average results and standard deviation for all 5A samples. . 45
3.17 ULTEM™ 9085 average results and standard deviation for all flexural samples. 46
3.18 On-edge flexural samples 47
3.19 ULTEM™ 1010 average results and standard deviation for all flexural samples. 48
3.20 Flex. sample On-edge 45°. 49
3.21 Compression test results, average, for ULTEM™ 9085. 49
3.22 ULTEM™ 9085 compression samples. Flat sample on left, upright sample on right. 49
3.23 Compression test results, average, for ULTEM™ 1010. 50
3.24 ULTEM™ 1010 compression samples. Upright samples on top, flat on bottom. 50
3.25 ULTEM™ 9085 Charpy Impact samples, notch sideways (left) and notch upright (right). 51
3.26 ULTEM™ 1010 Charpy Impact samples, notch sideways (top) and notch upright (bottom). 51
3.27 Broken ULTEM™ 1010 samples. 52

4.1 Double Panel equivalent circuit 62
4.2 Frequency ratio as a function of x and r from Maa's equations, missing an interval in the curve 64
4.3 Frequency ratio as a function of x and r after curve fitting. 64
4.4 Frequency ratio as a function of the perforation constant and r from Maa [26] 65
4.5 Frequency ratio as a function of the perforation constant and r from the code 65
4.6 Relationship between constants calculated by Maa. 66
4.7 Relationship between constants calculated in Matlab 67
4.8 Variation of α_{max} with r 67
4.9 Absorption coefficient variance depending on the incidence angle. 68
4.10 Comparison between the raw parameters obtained and the adapted values for manufacturing. 69
4.11 Absorption coefficient of the fixed parameters. 70
4.12 Absorption coefficient of different panels, varying the cavity depth ±0.15 mm. 71
4.13 Absorption coefficient of different panels, varying the thickness (t) ±0.5 mm. 71
4.14 Absorption efficiency of different panels, varying the perforation area (ϕ) ±3%. 71
4.15 Absorption coefficient of different panels, varying the cavity diameter ±0.2 mm and maintaining the perforation area constant 72
4.16 Absorption coefficient of different panels, varying the cavity diameter ±0.2 mm and maintaining the number of holes constant 72

4.17 Impedance Tube used for the tests. 74
4.18 Schematic of the Impedance Tube test configuration, taken from Tie et al. [239] 75
4.19 Placing of the sample in the tube, without the modeling clay. 76
4.20 Clay covering some of the perforations in one of the samples. 76
4.21 Comparison of the two case 4 panels tested. 77
4.22 Full range of results in the test. 77
4.23 Test results of case 2. 78
4.24 Test results of case 3. 78
4.25 Test results of case 4. 79
4.26 Test results of case 5. 79
4.27 Test results of case 6. 80
4.28 Test results of case 7. 80
4.29 Test results of case 8. 80
4.30 Test results of case 9. 81
4.31 Test results of case 10. 81
4.32 Test results of case 11. 81
4.33 Test results of case 12. 82
4.34 Test results for the two panel configuration. 82
4.35 Test results for the three panel configuration. 82
4.36 Comparison between cases 7 and 8, samples with the same design parameters except thickness. 83
4.37 Comparison between cases 9 and 10, samples with the same design parameters except thickness. 83
4.38 Comparison between cases 7 and 9, samples with the same design parameters except hole diameter. 83
4.39 Comparison between cases 8 and 10, samples with the same design parameters except hole diameter. 84

5.1 Irregular perforations in the panels for cases 2 and 3. 86
5.2 Material bumps and cracks on panels. 86
5.3 Hole diameter test plate. 87
5.4 Irregular perforations in the panels for cases 2 and 3. 88
5.5 Porosity in the tested samples 89
5.6 Readjusted analytical curve for case 4 for the diameter and percentage ratio. 90
5.7 Readjusted analytical curve for case 5 for the diameter and percentage ratio. 90
5.8 Readjusted analytical curve for case 6 for the diameter and percentage ratio. 91
5.9 Readjusted analytical curve for case 7 for the diameter and percentage ratio. 91
5.10 Readjusted analytical curve for case 8 for the diameter and percentage ratio. 91
5.11 Readjusted analytical curve for case 9 for the diameter and percentage ratio. 92
5.12 Readjusted analytical curve for case 10 for the diameter and percentage ratio. 92
5.13 Readjusted analytical curve for case 11 for the diameter and percentage ratio. 92
5.14 Readjusted analytical curve for case 12 for the diameter and percentage ratio. 93
5.15 Volume measurement test 94
5.16 Measuring the sample density 95
5.17 Density measurement samples. 95

5.18 Readjusted Case 4 panels with the porosity and correction parameters. . . . 97
5.19 Readjusted Case 5 panels with the porosity and correction parameters. . . . 97
5.20 Readjusted Case 6 panels with the porosity and correction parameters. . . . 98
5.21 Readjusted Case 7 panels with the porosity and correction parameters. . . . 98
5.22 Readjusted Case 8 panels with the porosity and correction parameters. . . . 98
5.23 Readjusted Case 9 panels with the porosity and correction parameters. . . . 99
5.24 Readjusted Case 10 panels with the porosity and correction parameters. . . . 99
5.25 Readjusted Case 11 panels with the porosity and correction parameters. . . . 99
5.26 Readjusted Case 12 panels with the porosity and correction parameters. . . . 100
5.27 Printed supports location for the ceramic resin panels. 101
5.28 Ceramic resin panels 102
5.29 Case 7 panel made of PEEK, with different perforation diameters. 102
5.30 Comparison in finish between the ULTEM™ (top) and PEEK (bottom) panels. 103
5.31 PEEK panels 103
5.32 Case 4 panels with three different AM materials. 104
5.33 Case 6 panels with three different AM materials. 104
5.34 Case 7 panels with three different AM materials. 104
5.35 Case 9 panels with three different AM materials. 105

List of Tables

3.1 Tensile test specifications. 33
3.2 Reference values [216, 217, 218, 219] of strength at break, yield strength and modulus of ULTEM™ 9085 and ULTEM™ 1010. 37
3.3 Tensile test results summary for ULTEM™ 9085 [208]. The Standard Deviation (SD) corresponding to each average value has been included in brackets next to it. 38
3.4 Tensile test results summary for ULTEM™ 9085 [208]. The Standard Deviation (SD) corresponding to each average value has been included in brackets next to it. 42
3.5 Flexural results summary for ULTEM™ 9085 [208]. The Standard Deviation (SD) corresponding to each average value has been included in brackets next to it. 44
3.6 Flexural results summary for ULTEM™ 1010 [208]. The Standard Deviation (SD) corresponding to each average value has been included in brackets next to it. 45
3.7 Compression Test results for ULTEM™ 9085 [208]. The Standard Deviation (SD) corresponding to each average value has been included in brackets next to it. 47
3.8 Compression test results for ULTEM™ 1010 [208]. The Standard Deviation (SD) corresponding to each average value has been included in brackets next to it. 47
3.9 Charpy Impact results summary for ULTEM™ 9085. 50
3.10 Charpy Impact results summary for ULTEM™ 1010. 51

4.1 Results comparison between Maa and the code. 66
4.2 Fixed parameters. 70
4.3 Nominal design parameters of the test cases. 73
4.4 Nominal design parameters of the two panel configuration 73
4.5 Nominal design parameters of the three panel configuration 73

5.1 Hole diameter test 87
5.2 Resulting thickness and estimated diameters in the tested panels 88
5.3 Change in the perforation ratio due to the estimated diameter 89
5.4 Results of the density samples 96
5.5 Density of the tested samples 96

5.6 Diameter of the perforations in the PEEK and Ceramic Resin panels. 102

Abbreviations and acronyms

AI	Artificial Intelligence
AM	Additive Manufacturing
ASTM	American Society for Testing and Materials
CAD	Computer-aided Design
CNC	Computer Numerical Control
CSIC	Consejo Superior de Investigaciones Científicas
DOF	Degrees-of-Freedom
ETSIAE	Escuela Técnica Superior de Ingeniería Aeronáutica y del Espacio
FEM	Finite Element Model
FDM	Fused Deposition Modeling
GMA	Giant Magnetostrictive Actuators
HPP	High-performance Polymer
ISO	International Organization for Standardization
MSLA	Masked Stereolithography
MEMS	Micro-Electric Mechanical System
MJF	Multi-Jet Fusion
MPP	Microperforated Panel
PEI	Polyetherimide
PVDF	Polyvinylidene fluoride
SMA	Shape Memory Alloy
SLA	Stereolithography
SLS	Selective Laser Sintering
TMD	Tuned Mass Dampers
TPU	Thermoplastic polyurethane

UPM Universidad Politécnica de Madrid

UV Ultraviolet

VCM Voice Coil Motor

Greek letters in equations

α Absorption coefficient

α_0 Maximum absorption coefficient

α_e Edge impedance

α_∞ Geometrical tortuosity

$\alpha_{\infty,mod}$ Modified tortuosity

$\mathbf{\Delta p}$ Pressure difference

η Dynamic viscosity of the air

θ Angle of oblique incidence

λ Wavelength

ρ Density

ρ_a Density of air under standard conditions

ρ_e Effective density

ρ_w Density of water under standard conditions

σ Perforation area percentage

σ_{mod} Modified flow resistivity

ϕ Porosity

ω Angular frequency

ω_0 Angular frequency at the resonance frequency

Roman letters in equations

$\mathbf{a}_\sigma$ Modifying parameter for the modified flow resistivity

$\mathbf{a}_{\sigma,\infty}$ Modifying parameter for the modified tortuosity

$\mathbf{b}$ Separation between holes

$\mathbf{c}$	Velocity of sound
$\mathbf{d}$	Hole diameter
$\mathbf{D}$	Cavity distance
$\mathbf{f}$	Frequency in Hz
$\mathbf{f}_0$	Resonance frequency
$\mathbf{g}$	Ratio of the mass and cavity reactances at low frequencies
$\mathbf{k}_m$	Mass reactance coefficient
$\mathbf{k}_r$	Resistance coefficient
$\mathbf{m}$	Relative acoustic mass
$\mathbf{r}$	Relative acoustic resistance
$\mathbf{r}_0$	Tube radius
$\mathbf{R}$	Reflection
$\mathbf{t}$	Panel thickness
$\mathbf{u}$	Axial particle velocity of the air
$\bar{u}$	Average velocity inside the tube
$\mathbf{W}_a$	Weight of the sample in air
$\mathbf{W}_f$	Weight of the sample submerged
$\mathbf{x}$	Perforation ratio
$\mathbf{x}_m$	Mass reactance
$\mathbf{y}$	Cavity depth ratio
$\mathbf{z}_D$	Relative acoustic impedance of the cavity
$\mathbf{Z}$	Acoustic impedance
$\mathbf{Z}_D$	Specific acoustic impedance of the cavity

Chapter 1

Introduction

In space missions, every kilogram counts, and reducing the mass of the payload while keeping it structurally safe is the primary objective of the design team. Reducing mass directly reduces launch costs and enhances fuel efficiency, facilitating more effective orbital insertion. This also applies to launch vehicles (see Figure 1.1), which have to sustain the brunt of the aerodynamic forces. In the 1960s, the Atlas-Centaur launch vehicle used a fiberglass fairing [1]. Then, to reduce weight, Ariane 4 used graphite epoxy face sheets with an aluminum honeycomb core in the fairing [2], which was also used by Soyuz, although with aluminum sheets [3]. More recently, in 2009, the Naro-1 (KSLV-I) and Nuri (KSLV-II) launchers used carbon fiber sandwich composites, trying to optimize acoustic insulation within strength limits [4]. SpaceX, on the other hand, chose stainless steel for the fairing of the Starship to be more cost-effective and increase the robustness during reentry [5]. This weight optimization introduces a trade-off: lighter structures generally exhibit lower stiffness, making them more susceptible to vibroacoustic excitation. As stiffness decreases, the natural frequencies of the components shift, often leading to higher vibrational amplitudes under acoustic loading. Adding mass is usually an effective method to reduce passive acoustic transmission [6], but it goes against the design philosophy.

One of the critical issues when designing space launchers is dealing with vibroacoustic coupling. The problem begins to occur during rocket launch, as the intense acoustic environment generated by the ignition, lift-off, and aerodynamic forces interacts with the structural components of the payload [7], the supersonic exhaust jet that is ejected one of the primary noise sources [8]. The generated loads typically cover a wide range of excitations, both in spatial properties and in the frequency range [9]. When these high-intensity acoustic waves couple with the structural elements of the payload, they amplify vibrational energy transfer, leading to significant mechanical stress and potential damage [10].

The acoustic environment during launch can impose severe stress on the payload, which can lead to different forms of structural damage, such as fatigue, fractures, and, in the worst case, catastrophic failures. More than half of satellite failures on the first day have excessive noise levels inside the housing as one of their causes [11]. The elements that are most at risk are those intentionally designed to be lightweight and structurally flexible, such as antennas, solar panels, and support structures, each of which is critical for spacecraft functionality.

Figure 1.1: Space launch vehicles. From left to right: Nuri (KSLV-II), Starship, Ariane-4 and Atlas-Centaur.

Damage to these elements can lead to mission failure by compromising communication, power generation, or structural stability.

Moreover, vibrations do not affect the payload uniformly. Resonance phenomena play a crucial role as different materials, shapes, and configurations respond variably to acoustic loads. Components with large surface areas and lower rigidity, such as deployable solar arrays and high-gain antennas, are particularly prone to excessive oscillations. These oscillations can induce misalignment, degrade performance, or, in extreme cases, cause mechanical detachment. Understanding and mitigating these interactions is essential for ensuring payload survivability and mission success.

An important challenge in mitigating this problem is the prediction of how the structural elements of the payload respond to the acoustic load. The interaction between acoustic waves and solid structures produces complex coupling effects that depend on the material, geometry, and structural interfaces. Recent advances in computational modeling and experimental testing have improved the understanding of vibroacoustic coupling, and numerical simulations, such as finite element analysis (FEA) and statistical energy analysis (SEA), are increasingly used to predict structural responses and optimize payload designs before launch.

Due to the importance of the components affected by the vibroacoustic coupling, mitigation strategies are required. There are usually two approaches to choose from to reduce the coupling. As the sound pressure inside the payload fairing cannot be reduced, as it requires reducing the thrust or modifying the aerodynamic design of the vehicle, the only remaining option is to reduce noise transmission, actively or passively [12, 13]. Active solutions, which are less common because of their complexity, involve real-time control systems that counteract resonant vibrations using actuators and sensors. Passive methods include the use of damping materials, vibration isolators, and advanced structural designs that distribute acoustic loads more effectively. The development of new materials and manufacturing techniques has also opened the door to hybrid methods, combining, for example, elastic elements and dampers

with an actuator [14].

A common method of passive mitigation is coating with absorbing materials. These materials can absorb sound and vibration into the interior of the fairing or to the payload. By converting acoustic energy into heat, these materials effectively reduce the transmission of energy, thereby minimizing the impact of high-intensity sound waves on sensitive payload components [15, 16, 17]. The selection of appropriate absorbent materials depends on factors such as frequency range, environmental conditions, and structural constraints.

Another type of passive mitigation technique is the use of cylindrical shells on the fairing of a spacecraft or launch vehicle. These shells serve multiple functions, including providing structural isolation due to their inherent damping properties, acting as an acoustic barrier to reduce noise transmission, and contributing to the overall stiffness and integrity of the fairing. Their effectiveness depends on the design, material and inclusion of additional damping or isolation techniques [18, 19].

Isolation mounts, such as rubbers, springs, and pneumatic mounts, are also common components in vibration mitigation. They function as mechanical isolators by absorbing and dissipating forces before they reach the payload. The choice of mounts depends on the desired operating frequency, the interface constraints of the spacecraft, and their load-bearing capacity.

Tuned Mass Dampers (TMD) are also passive mitigation techniques. These devices are among the oldest methods used for vibration control, dating back to 1909. TMDs are tuned to specific frequencies to counteract the loads at those frequencies, protecting critical components, and are used more commonly in tall buildings in Japan as a precaution against earthquakes. They have proven to be very effective in reducing vibration amplitudes at high frequencies in launch environments [20].

Active mitigation techniques use sensors, actuators, and control systems to counteract noise or vibrations in real time. Using the principle known as active noise control (ANC), these systems continuously monitor vibrational disturbances and generate opposing forces to cancel them out. They can achieve better dynamic environments in comparison with passive methods, but that solution comes with increased complexity and cost, besides other drawbacks. These active control methods can also be combined with passive techniques, such as cylindrical shells [21] or fluid-loaded plates [22, 23]. By strategically combining these techniques, engineers can effectively minimize the impact of harsh acoustic environments on sensitive payloads, ensuring their structural integrity and operational reliability during launch and ascent.

Choosing between mitigation techniques is complicated and often requires a trade-off analysis. Absorbing materials and mounts may increase the mass and volume of the spacecraft. The material selection is crucial, as they should be selected mainly on the basis of their ability to absorb a wide range of frequencies without increasing weight. However, advanced materials such as viscoelastic polymers can be expensive and challenging to integrate. The customization of each isolation system is also an issue, as each payload is different, which increases the complexity and cost of the design process. As the main objective of reducing the coupling is to ensure the mission's success, the integration of these mitigation methods has to be carefully balanced with the overall mission requirements.

As the space industry evolves towards lighter and more efficient solutions, new methods for vibroacoustic mitigation are appearing. One of the emerging technologies is the use of metamaterials [24] (shown in Figure 1.2). Researchers working on the "Silent Running" project (German Aerospace Center INNOspace Masters Challenge) at Fraunhofer LBF have investigated the use of metamaterials to reduce the acoustic pressure induce vibrations on launchers. Materials are structures consisting of periodic mechanical resonators applied to a specific component, enabling efficient reduction of vibrations in the stopband, with promising results [25].

Figure 1.2: Vibroacoustic metamaterial for launcher, from the Fraunhofer LBF [25].

Optimized structural designs, which integrate these advanced materials and control systems, are also crucial to addressing the vibroacoustic challenge. By using innovative modeling techniques and simulation tools, engineers can design launch vehicles that minimize resonant frequencies, distribute stress more evenly, and reduce vibration-induced damage. These designs also enable the use of flexible materials that can better absorb and dissipate vibrational energy.

By focusing on the optimization of these factors, advanced materials, active control systems, and refined structural designs, engineers will be better equipped to protect sensitive payload components, ensuring the integrity and reliability of missions. This, in turn, will allow space exploration to advance to new frontiers, with more frequent and cost-effective launches, greater payload capacity, and the potential for further innovations in space technology.

In recent years, microperforated panels (MPPs) and subwavelength devices have been proposed, which improve the absorption and insulation of the coping and reduce the coupling. However, the production techniques for such devices are costly and require complex and dedicated equipment, as well as long fabrication times [26, 27, 28]. Although there is some recent research on the manufacturing of this type of material using 3D printing techniques, such as that performed by Yang [29], the state of the art is not mature enough.

Microperforated panels (MPPs) are specialized acoustic panels designed to absorb sound through a mechanism known as "microperforation". These panels are typically made from materials such as metal, plastic, or wood and are characterized by a pattern of very small

holes, usually with diameters ranging from 0.1 to 1 millimeter.

The small perforations allow for sound waves to enter and interact with the air in the holes. This interaction causes frictional losses, dissipating the energy of sound as heat, resulting in sound absorption. MPPs act similarly to a Helmholtz resonator, absorbing specific frequencies and improving the acoustic performance. The perforations also help tomatch the acoustic impedance of the panel to that of the air, allowing for an efficient absorption of sound waves in a range of frequencies.

The main challenge of MPPs is that their performance depends on the precision of the perforations, requiring advanced equipment for their manufacturing. This increases the cost, as the materials and manufacturing processes can be quite expensive. This thesis aims to apply the 3D fabrication techniques investigated in the first part to the fabrication of this type of device, looking for characteristics such as fast manufacturing process, precision, and low cost for different topologies of the resulting structure.

The growth experienced in the field of additive manufacturing (AM) ever since its inception is nothing short of extraordinary. The first time a component was manufactured layer-by-layer using a computer-aided design (CAD) was in the 1980s [30], when Charles Hull invented the first form of 3D printing called stereolithography (SLA) [31]. SLA is a manufacturing process that uses ultraviolet (UV) light focused on a tank of liquid UV-curable photopolymer resin to harden it and a UV laser to build the layers. Before him, in 1981, Hideo Kodima created a device that used UV light to harden polymers, very similar to SLA, and almost at the same time as Hull, a team led by Alain Le Mehaute applied for the first patents using the SLA method, but it was abandoned by General Electric [32]. Since then, it has been referred to with different names, such as Rapid Prototyping, 3D printing, layered manufacturing, or solid free-form fabrication. Charles Hull founded his company, 3D Systems, in 1986, the first to develop 3D printers. This led others to try to develop new types of machine for additive manufacturing that used different materials or methods.

Very shortly after the foundation of 3D Systems, two different patents of additive manufacturing methods were filed, which nowadays represent the two most popular methods in 3D printing. In 1987, Carl Deckard filed a patent for Selective Laser Sintering (SLS) [33]. This method requires the powder to be deposited in thin layers, after which the layer is scanned with a high-power laser to harden it. This process is repeated after each layer. In 1989, Scott Crump, along with his wife, created (and patented in 1992) the Fused Deposition Modeling (FDM) method [34]. In FDM, a thermoplastic is fed through a hot nozzle that extrudes the material to create the layers of the component that is being made. He then went on to found Stratasys Inc., one of the leading manufacturers in 3D printing nowadays, both in printers and materials. By the 2000s, with the decrease in costs of 3D printers, many companies decided to invest in the capabilities of additive manufacturing.

As of today, the 3D printers are cheaper and better. People are now able to create their own components and their own designs, with a certain degree of complexity, in printers in a price range of 100-200 €. One of the various reasons for the growth among the common population is news outlets and social media [35]. These low-cost printers use mostly PLA, a thermoplastic monomer made from corn starch or sugar cane, making it also incredibly cheap

because they also present some of the lowest mechanical properties among polymers. The capabilities of 3D printing spread rapidly among employees at all levels and made them aware of its potential.

Although additive manufacturing is relatively new, it has seen incredible growth in some of the largest industries. Some of the fields that have adopted this manufacturing method are: medical, automotive, and aerospace industries. In the medical industry, additive manufacturing has been used for drug and pharmaceutical research [36], as well as for printing cartilages [37] and replacement tissues [38]. It can also help neurosurgeons by printing 3D models to practice surgical techniques [35]. For both automotive and aerospace, 3D printing has changed the way these industries design, develop, and manufacture new components. In particular, in the aerospace industry, there is a high fly-to-buy ratio, which is typically around 12: 1 or 25: 1 [39]. This implies that for each aerospace component produced, 12 to 25 units of costly material, such as titanium, are wasted. The weight is also a crucial factor in the aerospace industry, with the cost of sending a kilogram of payload to the Low Earth orbit ranging from $1,500 to$ 73,100, depending on the launch vehicle [40].

As space travel increases, reducing costs has become a priority for aerospace manufacturers. One way to achieve this is by reducing the weight of components through changes in design, materials, or manufacturing methods. Additive manufacturing (AM) is particularly effective in reducing weight and cost, as it allows simplification of complex components into single parts and provides greater freedom of geometric design [41, 42]. An example is GE Aviation's collaboration with Morris Technologies, which reduced the parts in a jet engine fuel nozzle from twenty to one, achieving a 25 percent weight reduction and shortened assembly times [43]. This has brought the buy-to-fly ratio almost to 1:1 [44].

Consequently, the aerospace industry has led the incorporation of 3D printing technologies and is considered a major promoter of additive manufacturing, along with the defense industry [45], since its inception in the 1980s [46]. 3D printing offers numerous opportunities for aerospace, transforming design, testing and validation, preproduction, and production processes [47].

Despite these advancements, the adoption rate of additive manufacturing (AM) in mainstream processes remains surprisingly low, as noted by Joshi and Sheikh [48]. The primary reason is the stringent certification requirements in the aerospace industry, which ensure the safety and reliability of components under extreme conditions. The absence of specific testing and safety standards for AM technologies complicates the certification of AM-produced parts, limiting their usage. Another factor highlighted by Joshi and Sheikh is the high energy demand of AM processes, which, despite their advantages such as complex geometries and reduced material waste, are energy-intensive.

Initially focused on rapid prototyping, AM now offers critical features for the aerospace industry such as the manufacture of complex, topologically optimized shapes with high strength-to-weight ratios, blind holes, and high surface area-to-volume ratio designs. It reduces the number of parts and junctions compared to traditional manufacturing, simplifying assembly and integration. AM can significantly cut down on the time-consuming assembly and integration processes by consolidating multiple parts into a single printed component.

Production speed is another major advantage of 3D printing. Traditional manufacturing

processes often require time-consuming tooling and molding changes, whereas 3D printing eliminates the need for molds or tools, enabling rapid design iterations and faster production times. The ability to quickly make design changes in a computer-aided environment significantly accelerates manufacturing. A survey by Jabil [49] found that 3D printing has sped up production times by allowing quick design changes without the need for mold or tool modifications. This is particularly beneficial for aerospace components that require intricate interior design and internal cooling, which traditionally require lengthy manufacturing processes. AM simplifies and shortens these processes, resulting in lighter components and less material waste.

Studies [50, 51] comparing the unit manufacturing cost of components using traditional processes versus AM show that as the complexity of the components increases, the costs of traditional processes increase, while the costs of AM remain relatively constant, as shown in Figure 1.3. This demonstrates the potential cost savings that AM can offer the aerospace industry.

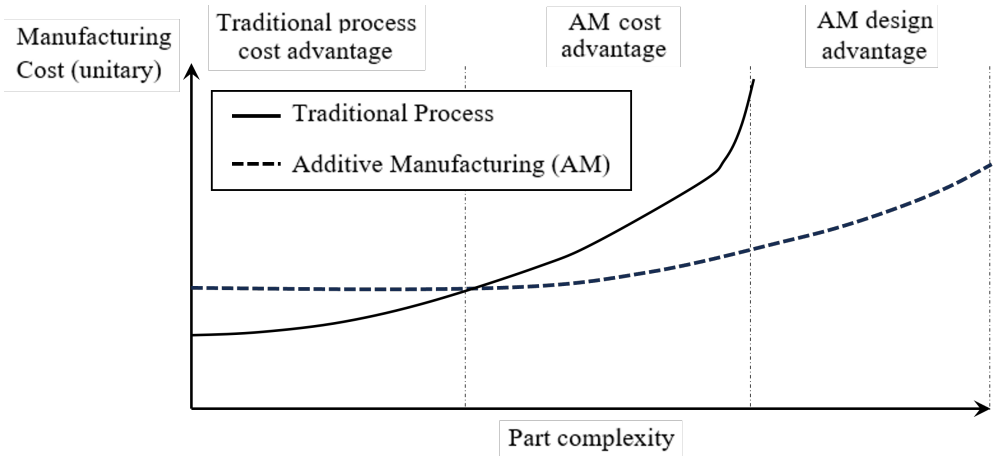

Figure 1.3: Comparison of manufacturing cost as a function of the part complexity [50].

In the past decade, extensive research has been conducted on materials suitable for aerospace applications [52]. Depending on the physical state of the material and the additive manufacturing (AM) technique used, ceramic materials, composites, metallic materials (aluminum alloys, steel, and titanium) and polymers can be printed. For polymers, high-strength materials have recently emerged. ULTEM™ is a high-performance polymer widely utilized in aerospace due to its exceptional strength, durability, and heat resistance. Invented by Joseph G. Wirth in the 1980s and initially marketed by the General Electric Plastics division (acquired by SABIC in 2007), ULTEM™ was originally used in the medical and chemical industries but has since become prevalent in aerospace applications due to its unique properties.

Two ULTEM™ materials particularly suitable for aerospace and also certified for that application [53, 54], are ULTEM™ 9085 and ULTEM™ 1010. ULTEM™ 1010, known for having the highest tensile strength among FDM filaments, results in robust and durable components and is commonly used in semi-structural and out-of-cabin parts, such as twinjets. In contrast, ULTEM™ 9085 is used in components where weight reduction is crucial without compromising strength, often found in inside-of-cabin parts.

Both ULTEMTM 9085 and ULTEMTM 1010 offer numerous benefits for aerospace applications, including dimensional stability, long-term heat resistance, high strength and stiffness, broad chemical resistance, low smoke generation, excellent fatigue and stress crack resistance, and hydrolysis resistance. These properties make them ideal for use in demanding aerospace environments where performance and reliability are essential, particularly in complex geometries, since the ultimate goal should be to approach the properties of parts manufactured by traditional methods.

The use of these two space-certified materials in additive manufacturing for microperforated panels on launch vehicle fairings or payloads could effectively mitigate acoustic coupling while maintaining a lightweight structure with excellent mechanical properties.

1.1 Objectives

In space structures, vibroacoustic coupling presents a significant challenge, often leading to structural damage to critical components such as antennas, solar panels, and support plates. As aforementioned, the extreme acoustic loads generated during launch can induce vibrations that compromise structural integrity, affecting both performance and longevity. To mitigate these effects, various solutions have been explored, including micro-perforated panels (MPPs) and subwavelength devices. However, while effective, these approaches often involve high production costs and lengthy manufacturing processes, limiting their feasibility for rapid developments and prototyping, and iterative design improvements.

Additive manufacturing (AM) has emerged as a transformative technology capable of addressing these challenges by enabling the fabrication of highly complex components using metallic, ceramic, and polymeric materials. One of the primary hurdles in AM lies in optimizing the mechanical properties of printed parts to ensure that they meet or exceed the performance of traditionally manufactured counterparts. Despite this challenge, AM offers unparalleled advantages, particularly in its ability to produce intricate geometries that would not be feasible using conventional manufacturing techniques. This capability is especially valuable for the development of novel acoustic damping structures tailored to the unique demands of space applications.

Recent advances in high-performance thermoplastic polymers, such as polyetherimide (PEI) and polyetheretherketone (PEEK), have further expanded the potential of AM in aerospace engineering. These materials exhibit an exceptional balance of strength, lightweight characteristics, and thermal stability, making them highly suitable for space-based applications where material performance is critical. The integration of such advanced polymers with AM techniques opens new possibilities for designing and manufacturing vibroacoustic mitigation solutions that are both technically efficient and cost-effective.

The primary objectives of this thesis are twofold. First, it aims to investigate current methodologies and technologies for developing new topological definitions of absorption and acoustic insulation elements, thus refining the underlying theoretical and mathematical frameworks. Second, it seeks to identify and evaluate suitable materials for these devices, focusing specifically on their application during the launch phase.

The main research areas include:

- The application of topological optimization techniques to enhance the mechanical properties of printed specimens, establishing design and technological parameters that improve structural resilience.
- An in-depth review of the state-of-the-art in acoustic devices manufacturing techniques with an emphasis on reducing fluid-structure coupling through innovative design methodologies.
- The development and validation of MPPs, using additive processes, with systematic testing to assess their acoustic performance, including frequency response, absorption bandwidth, and overall absorption coefficients.
- A comprehensive analysis of different additive manufacturing technologies to determine the most suitable processes based on material type, dimensional stability, and environmental constraints.

The dissertation is structured as follows:

- **Chapter 1: Introduction.** The introduction sets up the dissertation presenting the problem that spacecrafts face during launch, which is vibroacoustic coupling, and explains the usual methods used to mitigate it. It introduces the use of microperforated panels, used in other fields but not proven in spacecrafts, and proposes the use of additive manufacturing to make them, taking into account the weight issues in the space industry.
- **Chapter 2: State of the Art.** This chapter offers knowledge about basic concepts that are of importance for this work, such as additive manufacturing, high-performance polymers, and other methods used for vibration reduction in spacecrafts. It also includes an overview on sound absorption in spacecrafts and research on microperforated panels.
- **Chapter 3: Material Characterization.** The methodology followed for the mechanical test is described, including the quantity of samples, the type, and their orientation. The results are presented in this chapter and briefly discussed.
- **Chapter 4: Microperforated Panels.** This chapter starts with a review of the theoretical formulation of microperforated panels, followed by an explanation of how analytical solutions are found and an analysis of how the design parameters of the panel affect its absorption coefficient. It then explains the methodology followed for the acoustic tests and presents the results obtained,
- **Chapter 5: Discussion.** In this chapter, the results obtained in the mechanical tests (Chapter 3) and acoustic tests (Chapter 4) are analyzed and discussed in depth. New tests are performed and presented, and correction models are applied as a result, with the objective of finding the best procedure for the manufacture of MPPs with 3D printing.
- **Chapter 6: Conclusions.** The final instance of this dissertation explains the conclusions drawn from the results of the tests and their analysis, and the viability of additive

manufacturing microperforated panels for spacecrafts structures.

Chapter 2

State of the art

This chapter presents first some of the basic concepts of the topics discussed in this dissertation: the use of sound absorption mechanics in spacecrafts and the research done so far on microperforated panels. This is followed by a review of additive manufacturing, high-performance polymers, and vibration isolation methods typically used in space applications.

2.1 Sound Absorption techniques for vibroacoustic loads mitigation

Nowadays, two techniques are often used to reduce vibroacustic loads that could potentially damage the payload inside the launcher fairing: to mitigate noise levels at the source which implies to actuate into de launchpad; and/or to reduce sound pressure levels reaching out the payload inside the fairing, which usually requires acoustic absorbers.

2.1.1 Noise level reduction at the launchpad

Most strategies used include reducing the noise emitted by rockets, increasing sound absorption, or avoiding direct reflections toward the launch vehicle[6]. The most widely used solution is the injection of water (see Figure 2.1) around the launch pad, as it mitigates supersonic jet noise [55]. It affects the velocity and temperature of the exhaust jet, reducing noise levels, and decreases velocity fluctuations and turbulent shear stresses [56].

The impact of water ejection has been tested in numerous scale models of launch vehicles. The tests on the scale model of ARES 1 demonstrated a 3.4 dB using an above-deck water suppression [57]. On the scale model of the ARIANE 6 rocket, using water injection at the trench and water deluge directed towards and away from the support platform, indicated that the mitigation could be of 6 dB at lower altitudes, while at higher altitudes, the above-deck water injection provided a reduction between 1 dB and 3 dB [58]. The efficiency of this method means that many launch platforms around the world use it, including the Kennedy Space Center, the European Spaceport in French Guiana, and the Tanegashima Space Center. Despite the success in mitigating the noise, water injection can also have its drawbacks, as it

Figure 2.1: Water Deluge test from NASA.

may damage materials and structures [59], and affect the performance of deflectors [60].

Another method that reduces the generation of acoustic waves at the jet is plume/flame deflectors, shown in Figure 2.2. A flame deflector prevents the exhaust plumes of the launch vehicle from damaging the vehicle and platform. They are designed to restrain the discharge gas inside the deflector and reflect the impact to the surrounding environment [61]. In a NASA technical report from 1971, the acoustic efficiency of undeflected jets was stated to be 0.22%, a cone-shaped deflector had an efficiency of 0.05%, and a 45 inclined plate has one of 0.10%. The Space Shuttle launch pad utilized a V-shaped deflector, while the Vega launch pad uses a wedge deflector, which is more frequently used in rocket launch systems [59].

(a) (b)

Figure 2.2: Flame deflector from NASA

The deflector can be open or closed, in regard to the exhaust ducts. Closed deflectors are key in weakening the ignition overpressure [62], but are more vulnerable to thermal loads [61]. Open deflectors are more practical, but the closed deflectors have better noise mitigation. Studies [59, 63] have shown that extending the flame duct reduces the noise during launch, between 4 dB (10 m) and 8 dB (30 m), although there seems to be a point of diminishing returns [64]. Increasing the number of ducts can disperse acoustic waves over a wider area, although it depends on the launch vehicle [6]. In the VEGA tests, the difference in mitigation was very little between one or two ducts [63], but analysis has shown that, for a vehicle with five boosters, there could be a mitigation difference of 6.4-8.9 dB [65].

2.1.2 Sound absorption materials and microperforated panels

Sandwich composites provide poor acoustic performance, due to their high stiffness and lightweight, at low frequencies [66], so engineers use materials with high sound absorption or dampeners to protect the fairing of the launch vehicle. In his book, Ingard states that these materials dissipate sound energy into heat, through viscous and thermal effects [67]. There are three main types of sound-absorbing materials: porous, resonator, and hybrid. Porous materials are divided into cellular (foam), fibrous (mineral woods) and granular (bead packings), and use the difference in particle velocity and thermal gradients between the solid and the medium to absorb the noise [68]. The acoustic performance of porous materials depends on airflow resistivity, porosity, and tortuosity.

Acoustic blankets have been studied and used extensively. Depending on their thickness, their absorption curve moves to higher or lower frequencies [69]. They are, nevertheless, limited in their attenuation capacities to below 100 Hz due to the long wavelength at low frequencies. Porous and fibrous materials can potentially release particles that can become problematic in environments that require special cleaning, or where high-velocity gases circulate [70].

Resonant absorbers are very simple mechanisms composed of a mass and stiffness, designed to absorb noise at a specific frequency. The most common resonance absorbers are membrane absorbers, Helmholtz resonators, perforated plates, and slot resonators. Helmholtz resonators have been studied in rocket engines since the '60s. In 1969, five resonators of distinct cavity depths and known cavity gas properties were tested with a hydrogen-oxygen rocket engine [71]. They consist of a large volume with a small neck, as shown in Figure 2.3, in which the absorption is produced by viscous-thermal effects. The air is forced in and out of the cavity, causing the air inside the resonator to vibrate at a specific frequency. They can provide wide-band absorption, unlike the peak provided by porous materials.

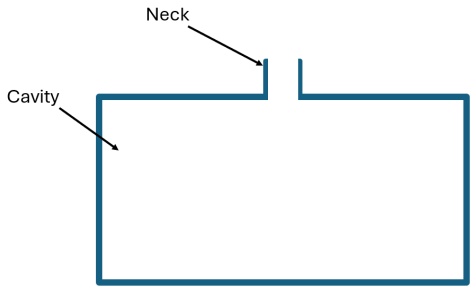

Figure 2.3: Diagram of a Helmholtz resonator.

Microperforated panels, diagram shown in Figure 2.4, were first proposed by Maa [26, 72] in 1975 as an alternative to these materials, establishing an approximate theory and a general theory on how to predict the acoustic properties of the panels. The studies conducted by Maa have led to multiple investigations on the theory of microperforated panels, so there are quite a few articles on the subject. The most prominent models to calculate the acoustic impedance of an MPP are the one from Maa [26, 72] and the equivalent fluid model [73, 74, 75]. Maa includes in his model the formulas used by Zwikker and Kosten [76] for perforated panels and porous materials, and the edge impedance, first proposed by Crandall [77], suggested by

Ingard [78], as well as the results obtained by Lord Rayleigh [79] for sound waves in small cylindrical tubes.

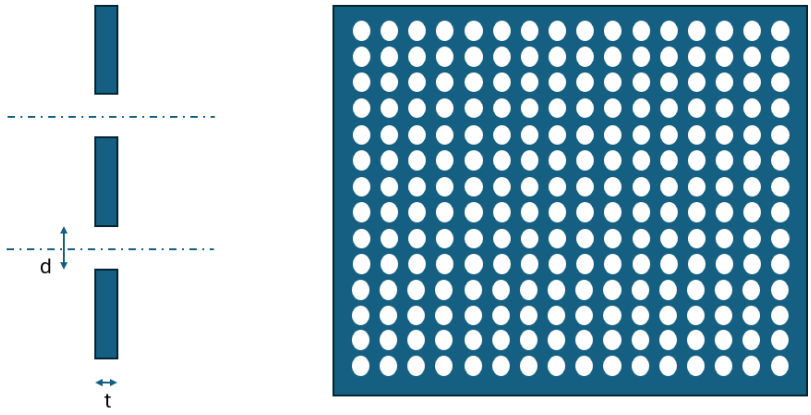

Figure 2.4: Diagram of an MPP.

To reduce manufacturing costs, different types of perforation have been studied both by Maa, who developed a theory of narrow slit perforations [27], and by other researchers [80, 81, 82] (Figure 2.5). Randerberg [28] also investigated this same type of perforation, but adjustable. Pfretzschner et al. [83] proposed something called a microperforated insertion unit (MIU), that would combine the millimeter perforations of a carrying plate with the micro perforations of a woven mesh. It would provide a similar performance to that of an MPP. Ruiz et al. [84] showed that this method would be significantly cheaper, as the carrying plate could be machined through a conventional method and commercial meshes could be used.

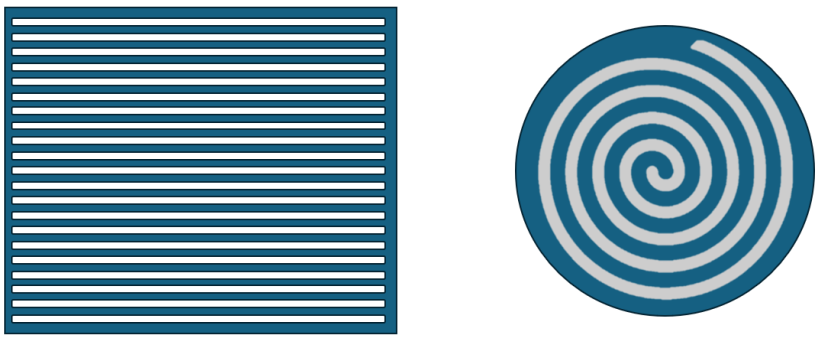

Figure 2.5: Sketch of two examples of microslit MPPs.

Huang [85] investigated the use of incompletely divided cavities, in which he introduced spacers of shorter length than the cavity and which could improve the absorbance at low frequencies. Mosa [86] studied the use of inhomogeneous boreholes, varying borehole diameter,

cavity depth, and borehole frequency, similar to Figure 2.6. This approach demonstrated the potential for improving sound absorption over a broader frequency range.

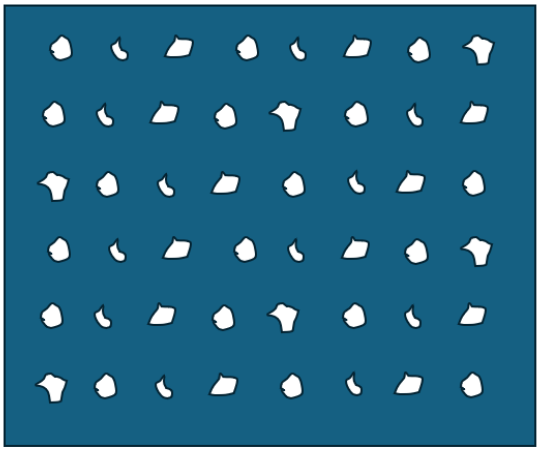

Figure 2.6: Sketch of a MPP with irregular holes.

To increase the absorption bandwidth, several researchers have proposed the use of multi-layer MPPS (ML-MPP). Maa [87] and Lee and Swenson [88] used the equivalent circuit technique to calculate the absorption coefficient, while Lee and Kwon [89] used the impedance transfer method. The two methods provided different results, as proven by Cobo et al. [90]. Cobo used the impedance transfer method to analyze both double [90] and triple layer [91] MPPs. Figure 2.7 shows three of the main design parameters (cavity diameter, panel thickness, and cavity distance) in the triple MPP configuration. The missing design parameter, the perforation area percentage, determines, along with the cavity diameter, the number of perforations in the panel.

Other proposals include:

- combining MPPs with Helmholtz resonators [92],
- membrane cells [93],
- perforation of Polyvinylidene fluoride (PVDF) films [94],
- partitioning the air cavity with different depths [95], similar to Huang [85],
- growing carbon nanotubes at one side of MPP [96],
- adding mechanical impedance plates which resonate at proper frequencies [97, 98],
- helical structures of rolling thin paper that would make the high sound absorption be provided by viscous-thermal loses in the thin slits, resulting in winding [99, 100].

Alternative manufacturing methods have been proposed by Quian et al. [101] and Cobo and Montero de Espinosa [102]. The first used Micro-Electric Mechanical System (MEMS) technology to machine MPPs with ultraperforations, with holes smaller than 100 μm, which allowed for a bandwidth larger than that of a conventionally manufactured MPP. The latter

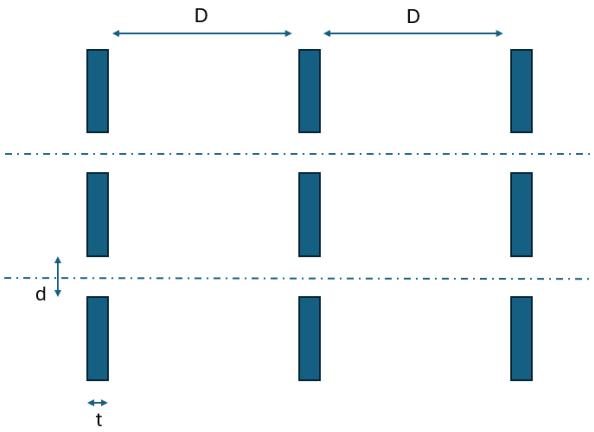

Figure 2.7: Design parameters of the MPP configuration: cavity diameter (d), panel thickness (t) and cavity distance (D).

used an infiltration technique, mixing polymeric material with salt grains. Once mixed and cured, it was introduced in a water bath to remove the salt grains, which would leave irregular holes of sub-millimetric size.

More recently, both Liu [103] and Jiang [104] investigated the acoustic properties of microperforated panels fabricated by 3D printing on porous materials inspired by Maa's publications, both with good results. On the other hand, Akiwate [105] performed an acoustic characterization study on printed panels with a honeycomb-type structure backing and with circular and non-circular perforations. At the same time, Yang investigated the 3D printing of micro-perforated panels for an adjustable absorption band.

Despite these advancements, it is important to note that none of the aforementioned studies utilized the high-performance aerospace materials proposed in this thesis. They have been discussed as a possible solution, but with no experimental testing as of now. The integration of such materials in additive manufacturing processes for MPPs could further expand their application potential, particularly in environments where both acoustic performance and material durability are critical. This area remains largely unexplored, presenting a significant opportunity for future research and innovation.

2.1.3 Other structural vibration reduction techniques

Protection systems in spacecraft are critical to the success of the mission, ensuring the safety of the crew and the integrity of the spacecraft. Various systems have been developed and research about that have aimed to reduce or isolate the effects of vibrations caused by external forces and noise.

Passive isolation systems

Passive isolation methods are extremely common in aerospace as they can be integrated without need to control them. Depending on how the energy is dissipated, passive techniques

for spacecraft can be divided into four groups: spring dampers, negative or quasi-zero stiffness mechanisms, smart materials, and mechanical metamaterials and structures [106].

Spring dampers reduce the transmission of energy between the source and receiver through the use of a connection made of elastic elements, which gain their resilience from their shape or materials [107]. They are generally springs, pneumatic structures, or elastomeric designs. Viscoelastic materials were one of the first isolators across multiple fields and are usually referred to as elastomeric mounts [108]. They have been profoundly studied, especially their effect on reducing vibrations in satellites [109, 110, 111]. In their research, Kawak, Cabon and Aglietti showed a strategy in which their performance in the early stages of design [112] could be predicted. They characterized the mechanical and thermal properties and established a correlation between the properties and the transmissibility curves. Shi et al. [113] designed a passive viscoelastic isolator for the attenuation of a single gimbal control moment gyro, while Xu et al. [114] designed one to be used in reaction wheels. Although viscoelastic materials have been used across a variety of platforms because of their lightweight, simplicity, reliability, and cost, they have a strong dependence on temperature, a limited loss factor, and poor performance at low frequencies.

Mechanical springs are the most common dampeners, as they can be custom made for many different stiffness properties. In the KEPLER spacecraft, the reaction wheel used a combination of metal springs and other passive components to stabilize the telescope to maintain its precision [115]. Huang [116] designed a launch environment damper in China for the SDLT-1 satellite using the Stewart platform. It was designed to ensure the platform's structural integrity, and the imager was isolated with three springs placed between the basement and the satellite's roof boards, and was tested with success. Wang et al. [117] introduced an X-shaped structure to suppress post-capture vibration induced by collusion, connected to other elements in a Stewart platform. It showed better vibration suppression compared to the spring-mass damper of the Stewart platform, but its bearing capacity and vibration isolation were more limited.

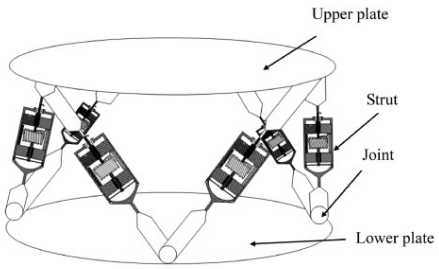

Figure 2.8: Example of a Stewart platform [118].

Quasi-zero stiffness is a property of certain mechanical systems where it behaves as if it has a very low or almost no resistance to deformation over a range of operating conditions. This is due to the non-linear characteristic of stiffness in high static and low dynamic elastic elements [119], and is achieved by introducing a negative stiffness with a parallel positive stiffness. Tang et al.[119] proposed an isolator in a 6 DOF Stewart platform, which theoretically is supposed to be incredibly stable in a space environment. Li et al. [120] introduced the idea

of a quasi-zero stiffness double pendulum system device, which had a variable stroke and an adaptive adjustment. This system was tested successfully in the Milli-Arc-Seconds Space Pointing Measuring Instrument (MAS-SPMI) micro-vibration test. However, there are still doubts about the efficiency of these high-frequency systems, so their viability in satellites is unprovable at the moment as they cannot withstand the launch environment.

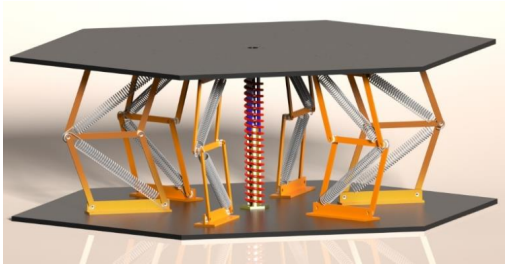

Figure 2.9: Proposed quasi-zero stiffness platform [121].

Shape memory alloys (SMA) are extremely common due to their extreme elasticity and the shape memory effect [122, 123]. A deformed SMA can recover its original shape upon unloading or heat application, due to the stress-induced phase transformation from austenite to martensite. To ensure structural integrity in the launch environment, Kwon et al.[124, 125] researched the use of SMA in the form of a washer. When tested without an isolator, it demonstrated a notable impact in reducing disturbances. Passive vibration isolators made of SMA have not yet been tested in space.

Metamaterials are artificially engineered materials that have properties not commonly found in nature. Their characteristics derive from their structure and not from their chemical composition [126]. These properties are such as negative stiffness, zero or negative Poisson ratio, and negative effective mass density [127]. Xu et al. [128] introduced an approach that used mass blocks to isolate microvibrations in linear and L-shaped joint sandwich structures in satellites, while Lu et al. [129] proposed a multifunctional metamaterial featuring a low-frequency bandgap, achieved by embedding nonlinear spherical pendulum resonators in a magnetic cavity. This design created a bandgap that suppressed low-frequency vibrations and enabled energy harvesting. Metamaterials, according to the recent literature, have shown promise in the attenuation of mechanical waves and in the isolation of low-frequency vibrations. The main disadvantage is high power consumption, which is becoming a growing concern, particularly with the miniaturization of small satellite platforms that have limited power generation and storage capacities [106].

Active isolation systems

The most common active isolation systems are actuators and sensors that are used to control force and feedback signals. They are good in the low-frequency regions in various active control schemes, according to Liu et al.[130]. The most frequently used actuators identified in the literature are: Voice coil motors (VCM), piezoelectric actuators, giant magnetostrictive actuators (GMA), and magnetic levitation (maglev).

The voice coil motors (Figure 2.10) operate according to the principle of electromagnetic

induction. They generate a constant upward force on a working range and do not consume energy to support the payload [131]. VCMs are used in systems that require precise linear motion and are favored for their ability to provide smooth, fast, and highly controllable movement. They also have the advantage of a compact structure, a wide control frequency band, and a large actuating displacement [132]. In 2014, Chi, Cao and Huang [133] designed a WSVI platform based on a circular payload adapter, which used a VCM to isolate vibration in the range of 5-100 Hz. In another study from 2014, Weipeng et al. [134] examined a soft active isolator (SAI) with a stationary permanent magnet to assess its effectiveness in isolating microvibrations for sensitive satellite payloads, achieving an attenuation of -20dB in the 5-100 Hz range. More recently, Yalcin and Erkan [135] optimized the use of an electromagnet-based hybrid zero power microvibration isolator, including coils and permanent magnets. Electromagnetic actuators based on Voice Coil Motors (VCM) have been researched and applied across various platforms, such as the Active Rack Isolation System (ARIS) and the European Space Agency's Micro Vibration Isolation System [136].

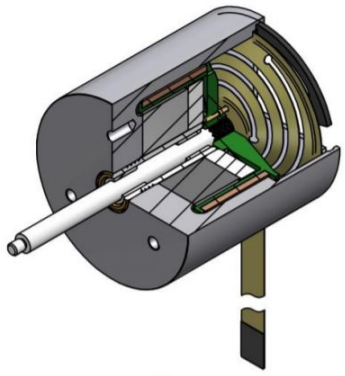

Figure 2.10: Example of a VCM actuator.

Actuators convert electrical energy into mechanical energy, and piezoelectric actuators rely on the materials of the same name, which are considered smart materials. The properties of piezoelectric materials can change when an electrical field is applied [137]. In this case, piezoelectric actuators produce small movement when a high voltage is applied, and they are used for ultraprecise positioning or when handling high forces in static or dynamic situations [138]. They have been applied in the Payload adapter for Ariane-5 [139] and the Satellite Ultra-quiet Isolation Technology Experiment SUITE [136, 140]. They offer low electromagnetic interference, fast response, reduced system complexity, and large output force, although their properties vary with environment.

Magnetostrictive actuators (Figure 2.11a) are devices that use the magnetostrictive effect, which is the change in the shape or dimensions of a material when exposed to a magnetic field. They can deliver high-output forces and can be driven at high frequencies, which makes them suitable for vibration control applications [141]. Although the literature is numerous, magnetostrictive actuators have not yet been applied in any spacecraft systems because there are still issues related to their heat generation, complexity, and high price.

Maglev actuators (Figure 2.11b) address the issues of piezoelectric and magnetostrictive

actuators with respect to mechanical contact [106], as they can generate motion [142] without direct physical contact [143] and offer effective isolation over a wide range of frequencies [144]. Their excellent precision and dynamic performance make them a good option for vibration isolation in spacecraft, and thus have been applied in the Microgravity Active Vibration Isolation System MAIS [145] and CHASE [146]. The main drawbacks of maglev actuators are their large power consumption, cost, and complexity.

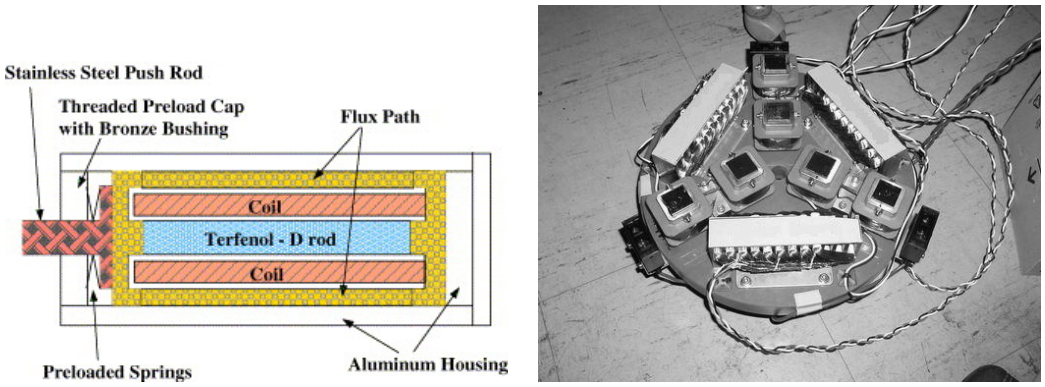

(a) Design of a magnetostrictive actuator, from Tan and Baras [147].

(b) Maglev actuator, from reference [148].

Figure 2.11: Examples active isolators

2.2 Additive Manufacturing: Basic Concepts

This section presents the different methods of additive manufacturing, their nature, the vibrations caused by sound waves, and the possible methods to mitigate them.

2.2.1 Fused Deposition Modeling

There are several different methods of additive manufacturing, but not all can be applied to the same materials. Some methods are exclusive to a material type, such as metals, polymers, or ceramics. For polymers, each of the methods available has its advantages, depending on the type of polymer used, the complexity of the design, the desired properties, or the intended use of the component.

The methods normally used for thermoplastics are Selective Laser Sintering (SLS), Multijet Fusion (MJF), and Fused Deposition Modeling (FDM). The first two involve powdered material. While SLS fuses the powder particles together, building the object layer by layer, MJF utilizes a fusing agent deposited where the powder should be solidified, followed by detailing the edges to refine the edges. Infrared light is used to fuse the powder, and the process starts again. Some common thermoplastics used in these two processes are nylon and thermoplastic polyurethane (TPU). FDM is the most common method for AM with thermoplastics. As mentioned in the Introduction, it involves extruding a filament through a heated nozzle, which melts it and deposits it. Afterward, the material cools and solidifies, bonding the layers.

FDM, widely recognized for its accessibility, versatility, and cost-effectiveness, has seen substantial evolution since its inception. Continuous advancements in materials, hardware, and software, as well as the emergence of more demanding applications, have driven FDM to deliver better precision, improved print quality, and enhanced mechanical properties. These developments have significantly broadened the capabilities of the technology, making it suitable for more complex and performance-critical applications in various industries.

Materials

One of the significant advances in FDM is the introduction of high-performance polymers such as PEI (Figure 2.12) and PEEK (Figure 2.13), which has opened the doors to industries such as aerospace, automotive and healthcare. These polymers provide exceptional mechanical strength, chemical resistance, and thermal stability, allowing FDM-printed parts to withstand harsh environments and demanding conditions that were once considered out of reach for thermoplastics.

(a) Component printed with ULTEM ™ 1010

(b) Component printed with ULTEM™ 9085

Figure 2.12: Components printed with ULTEM ™ 9085 and 1010, from STRATASYS.

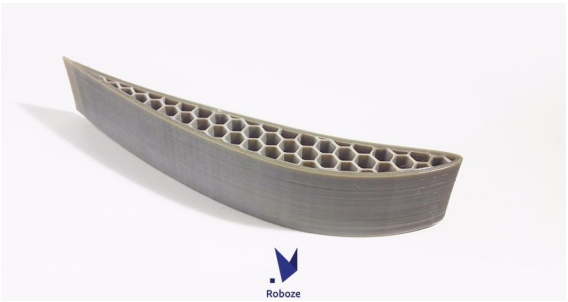

(a)

(b)

Figure 2.13: Components printed with PEEK, from Roboze.

The rise in popularity of composite filaments, such as carbon fiber reinforced polymers (Figure 2.14), has also expanded the capabilities of FDM. These materials combine the

lightweight and high strength of carbon fiber with the versatility of thermoplastics, resulting in stronger components with a better strength-to-weight ratio, ideal for critical applications. In addition, the emergence of metal-filled filaments has brought metal-like properties to FDM, enabling the manufacturing of components with improved durability, wear resistance, and a more metallic finish. Although not the same as a metallic component, these filaments are a cost-effective alternative to parts that require the versatility of FDM and some characteristics of metals.

Figure 2.14: Components printed with carbon fiber reinforced filament.

Another key advancement is the development of conductive filaments, which enable the manufacture of functional electronic components in FDM printers. This means that some components can be manufactured with embedded circuitry (Figure 2.15), opening up opportunities in industries such as electronics, robotics, and wearable technology. With conductive materials, complex assembly processes can be eliminated, as 3D printers can directly produce integrated and smart components.

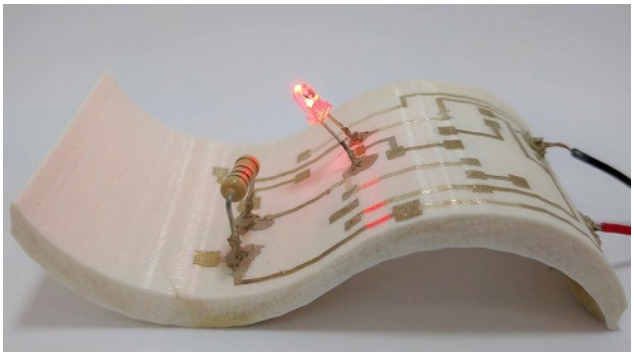

Figure 2.15: Example of a 3D printed PCB with conductive filament.

Sustainability has become a focal point in many industries, with many advances directed towards the reduction of waste [149]. In FDM, biopolymers, such as PLA, derived from renewable resources, are very popular, especially among personal printers. Some studies explored a method for reducing plastic waste by modifying the behavior of the material or optimizing the support structure [150, 151]. In addition to these types of materials, there is an interest in recycling waste material [152], which has a low rate due to the diverse amount of plastics, additives, and composites used [153]. Another option could be to create closed-loop

systems in which discarded prints and support materials are reprocessed to produce new filament [154].

Hardware

Hardware has also been through several innovations in recent years. The newest FDM printers can have dual (Figure 2.16), triple and quad (Figure 2.17) extrusion systems, allowing for the combination of different materials in a single print. The combination of materials enables the creation of components with varying mechanical properties or integrated functions. For example, a single component could have both a rigid structure and flexible joints, which is very useful in applications that require multifunctionality, such as robotics and medical devices.

The use of multiple extrusion systems also enables the combination of filament types, such as rigid thermoplastics, with elastomers or support materials. This allows for an increase in design complexity that can be printed while also reducing the need for manual assembly as the support materials available can be either dissolved or easily removed. The versatility of FDM printers has made them very attractive for prototyping and end-of-use parts, especially in high-performance sectors [155].

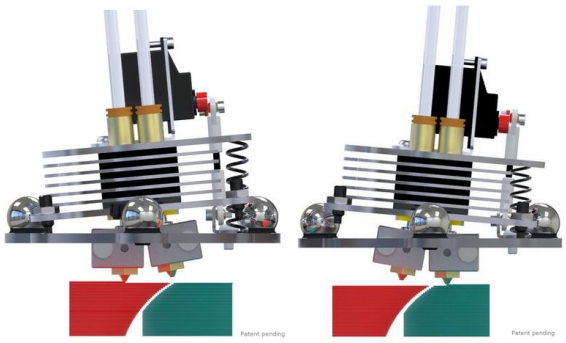

Figure 2.16: Example of a 3D printed dual extrusion system.

Some industries, such as aerospace and automotive, have also developed large-format printers (Figure 2.19). These FDM printers can manufacture sizable components in a single print, reducing the need for assembling smaller parts and offering structural advantages. These parts can maintain high strength and integrity without relying on fasteners or joints. Printers also increase manufacturing efficiency, cutting down the lead time for large parts that would require several steps to complete through traditional means.

In addition to extrusion systems and build volumes, improvements and advances in extruder designs have also improved the overall performance of the FDM printer. Direct drive extruders (Figure 2.19a), compared to Bowden extruders (Figure 2.19b), offer more precise control over filament feeding, resulting in smoother extrusion and better print quality [156]. It also has better retraction, requires a less powerful motor, and is more compatible with a wider range of filaments. All-metal hot-ends can reach higher temperatures, allowing the use of high-performance materials.

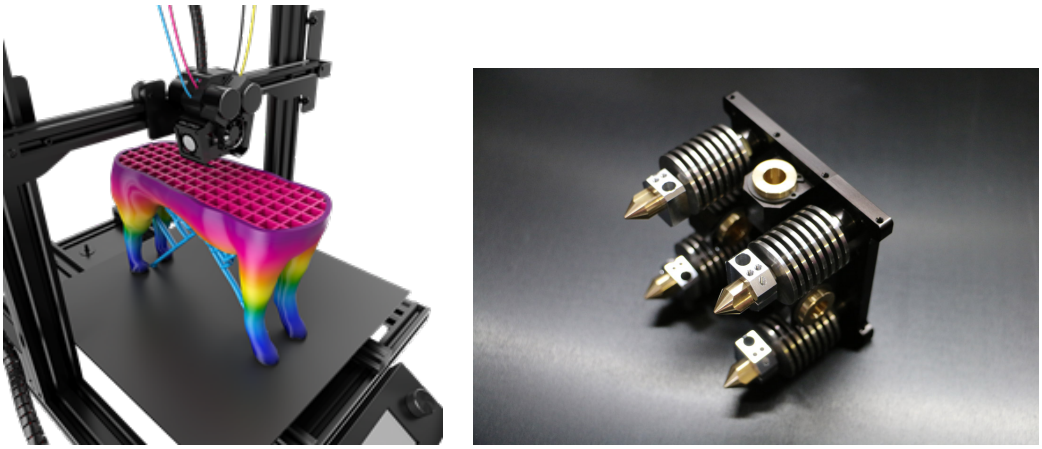

(a) (b)

Figure 2.17: Quad extrusion system.

(a) Example of a large format printer made by BigRep

(b) DIY large format printer made by PhD student Daniel del Rio Velilla, from ETSIAE, for his Master's thesis

Figure 2.18: Large format printers.

Nozzle technology has also improved with the development of hardened nozzles for abrasive materials like carbon fiber reinforced composites and metal-filled filaments. They provide greater durability and wear resistance, and they manage more challenging materials while maintaining high precision and quality of the parts. The advances in motion control systems have contributed to an increase in reliability and precision of modern printers. The improved stepper motors, linear guides, and belt tensioning systems provide a more accurate movement, reducing problems such as vibration, warping, and layer shifting.

Software

The software available today for FDM has seen significant advancements, incorporating new technologies such as advanced slicing algorithms, machine learning, and topology optimization. These improvements can optimize print efficiency, material use, and overall quality.

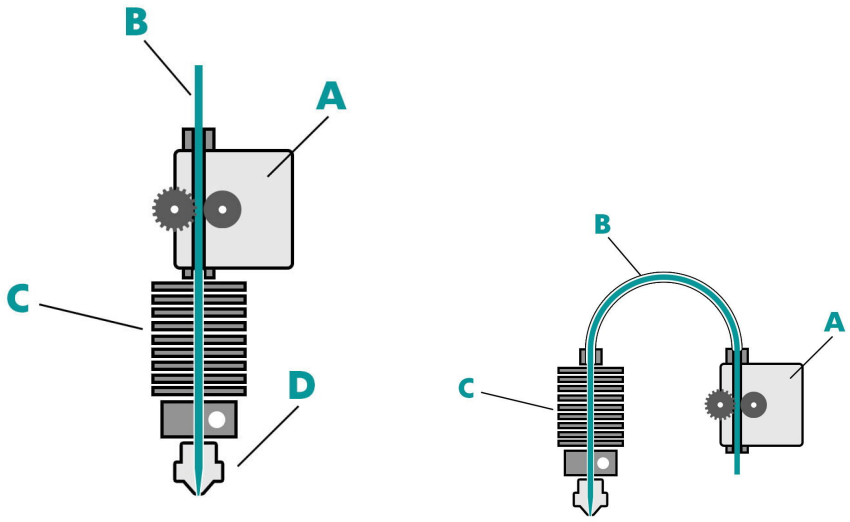

(a) Direct-drive extruder (b) Bowden extruder

Figure 2.19: Different types of extruders. In both figures (A) extruder (B) filament (C) hotend (D) nozzle

Optimizing or eliminating the support structure is a key factor in the advancement of FDM, to help reduce the material usage, simplify removal, or reduce the postprocessing time. Slicing algorithms can be divided into two groups: planar and nonplanar. Planar algorithms generate flat layers, while nonplanar algorithms can provide curved and out-of-plane layers, increasing build speed, reducing or eliminating support structures, and enhancing mechanical properties [157], making it possible to print overhangs without the need of support materials [158]. While incredibly promising, there is a lack of a suitable approach to nonplanar slicing that considers layer thickness and tool orientation [159].

Modern software can include dynamic layer height adjustments and adaptive infill patterns, optimizing the print path for speed, strength, and material efficiency. By adapting the height of the layer [160] and the infill [161] depending on the zone of the component, the user can ensure fine detail and better mechanical properties in critical areas while reducing material waste and speeding up the process in less demanding zones, but maintaining the mechanical integrity of the component.

Machine learning and Artificial Intelligence (AI) have demonstrated remarkable success in fields such as aerospace [162], manufacturing [163], and bio-3D printing [164], and their integration into FDM printers is now enhancing process control [165], also helping to optimize the parameter or the printing path. Using real-time sensor data, machine learning algorithms can predict and prevent possible print failures, such as overhang instability, material inconsistencies, or warping [166]. These algorithms would provide the ability to adjust parameters such as extrusion speed or nozzle temperature during the print to ensure the print quality without the need of outside input. This would not only reduce errors but also minimize downtime and waste, making the entire process more reliable and efficient.

In a study by Goh [167], a real-time monitoring system was developed using a camera and

laptop to employ computer vision and machine learning models to identify printer anomalies and make real-time corrections during the printing process (Figure 2.20). The system classified image data into categories such as under-extrusion and over-extrusion, with a correction algorithm executing appropriate adjustments based on the identified issues. This approach significantly improves print consistency and reduces the likelihood of print failures.

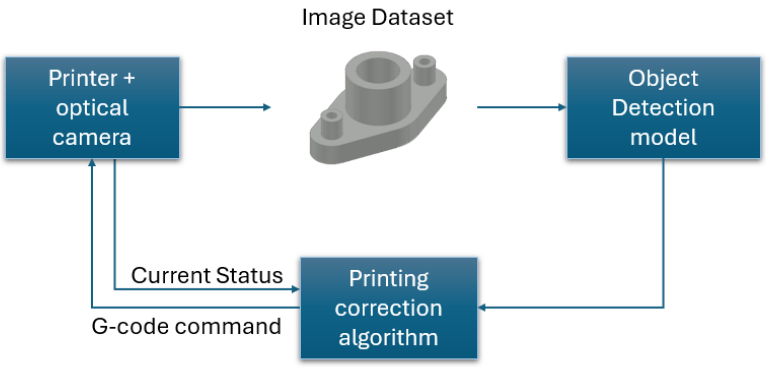

Figure 2.20: Illustration of the monitoring and self-correction system designed by Goh [167]

Some of the CAD software available nowadays can incorporate topology optimization and generative design tools [168, 169], which allow engineers to create complex geometries optimized for their function, resulting in light and structurally strong parts that would be difficult or extremely expensive to perform by traditional means. The characteristics of FDM, creating the part layer by layer, allow for this possibility and fully realize the potential of these tools, allowing for innovations in industries where performance and material efficiency are important.

Future

There are still areas where FDM can improve that are being looked into, such as improving surface finish and precision and integration with other manufacturing technologies. The inherent layer-by-layer construction of 3D printed components results in visible layer lines and less refined surface textures. Researchers and manufacturers are actively exploring new techniques to address this issue, including advanced post-processing methods such as sanding [170, 171, 172], chemical smoothing [173, 174], and vapor polishing [175, 176]. These techniques continue to make significant strides in improving print quality, delivering smoother surfaces and a more polished appearance.

Another area of improvement is hybrid manufacturing, which combines traditional manufacturing methods, such as computer numerical control (CNC) or injection molding, with FDM. This integration allows manufacturers to leverage the design flexibility of FDM for complex geometries while profiting from CNC finishing precision [177] or the mass production of injection molding. Hybrid manufacturing combines the strength of each method [178], enabling the production of parts that would otherwise be difficult.

These advancements and integrations are pushing the boundaries of FDM, expanding its capabilities beyond rapid prototyping to become a more competitive option for end-use

production and functional parts. As technology continues to evolve, further improvements can be expected in print quality, precision, and production efficiency, making FDM a more powerful and versatile tool in the manufacturing ecosystem.

2.2.2 High-performance polymers

Polymers can be categorized on the basis of their chemical structure, properties, or applications. The most common classification groups them into thermoplastics, thermosets, and elastomers. Thermoplastics soften when heated and return to their original state upon cooling. This behavior occurs because their polymeric structures are held together by weak intermolecular forces that can easily be disrupted by heat [179]. Thermosets, on the contrary, have three-dimensional cross-linked network structures that do not soften when heated. This is because covalent bonds are formed by a cross-linker connecting their polymer backbones, making them resistant to reshaping through heating. Finally, elastomers are flexible polymers that can stretch and return to their original shape once the applied stress is released [180, 181].

High-performance polymers (HPPs) are a type of polymer that exhibits superior mechanical, thermal, chemical, and electrical properties in comparison with standard polymers. These polymers are engineered to withstand extreme conditions (corrosive environments, high temperatures, pressure conditions, etc.), making them perfect for demanding applications in various industries and, in some cases, good substitutes for more traditionally used materials, like aluminum.

There are several criteria for a polymer to be considered as high-performance, the polymer having to satisfy one or more, some of them being [182]:

- The polymer must have a durability of at least 10,000 hours at 177 °C, maintaining its properties under short- and long-term exposure to mechanical stress, harsh chemicals, and electrical shock at this temperature. It should also remain stable when subjected to various types of radiation and corrosive environments at 177 °C.
- The thermal decomposition temperature should not be lower than 450 °C, with a desirable 5% weight loss determined by dynamic thermogravimetric analysis at a heating rate of 2.5 ° C per minute.
- Weight loss rates should be minimal at elevated temperatures.
- The temperature at which 10% deflection occurs under a 1.52 MPa load should be at least 177 °C.

Figure 2.21 shows the common classification of polymers. Cost and performance increase with each level, as well as with the maximum operational temperature. High-performance polymers are sometimes divided into high-performance and ultra-performance or imidized materials. These materials are at the top of the pyramid, with the best physical properties at over 200º C. Two examples of imidized materials are DuPont™ Vespel® Polymide (PI) and Torlon® Polyamide-imide (PAI), both also used in aerospace components. Polyamide components can be manufactured through Direct Forming or isostatic molding, while PAI is processed by compression molding, injection molding and extrusion.

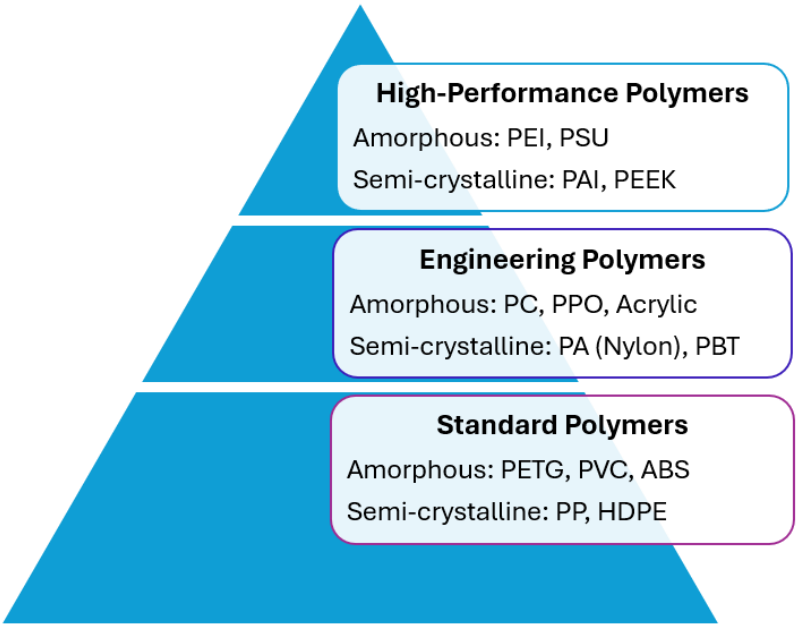

Figure 2.21: Classification of thermoplastics

HPPs can be classified into three main categories: amorphous, semicrystalline, and liquid crystalline polymers, the latter of which is not shown in the figure. Each of these types has distinct structural characteristics that influence their properties and applications.

- **Amorphous**: These polymers lack a well-defined crystalline structure, which gives them unique characteristics such as high transparency, bondability, and thermoformability. Amorphous polymers such as polysulfone (PSU) and polyetherimide (PEI) exhibit excellent dimensional stability and good impact resistance and are often used in applications where precision and clarity are important. Their lack of crystallinity allows them to be easily processed and molded into complex shapes, making them ideal for structural components, medical devices, and electrical insulation [183, 184].
- **Semi-Crystalline**: Semicrystalline polymers have regions of ordered crystalline structures within an amorphous matrix, giving them a combination of toughness, rigidity, and resistance to deformation. Examples include polyphenylene sulfide (PPS) and polyetheretherketone (PEEK). These polymers are widely used in bearing and wear applications because of their superior resistance to wear, chemicals, and high temperatures. Their crystalline regions contribute to their strength and chemical inertness, making them suitable for harsh environments, such as those found in the aerospace, automotive, and oil and gas industries. Furthermore, the crystalline nature of these polymers often results in lower moisture absorption and better dimensional stability under load [185, 186].
- **Liquid Crystalline Polymers**: a unique class of polymers that exhibit a highly ordered structure even in the molten state. This ordering results in exceptional mechanical properties, including high strength and stiffness, along with excellent resistance to chemicals

and heat [187]. LCPs are often used in electronics, particularly in applications requiring precision, such as connectors, flexible circuits, and other components where dimensional stability at high temperatures is crucial [188]. Their inherent flame retardancy and low coefficient of thermal expansion further enhance their suitability for high-performance electronic and industrial applications [189].

Each category of high-performance polymers offers distinct advantages that make them suitable for specific applications. Amorphous polymers are preferred for their processability and clarity, making them ideal for structural and optical components. Semi-crystalline polymers, with their superior wear resistance and thermal stability, are favored in applications involving high mechanical stress and exposure to harsh chemicals. Liquid crystalline polymers, known for their extraordinary strength and thermal properties, are essential in advanced electronic and industrial applications where precision and durability are paramount.

Polyetherimides, which are known under the branded name ULTEM™ are a class of high-performance polymers that combine the beneficial properties of polyimide and polyether units within their backbone structure. This unique combination was developed to address the demand for a material that not only offers the thermal and chemical stability typically associated with aromatic ethers and imides but also remains melt-processable, allowing for greater versatility in manufacturing processes.

PEI is widely recognized for its outstanding resistance to high temperatures, with continuous use possible at temperatures up to 180 °C without a significant loss of its mechanical properties [190]. This high-temperature performance is complemented by the material's impressive strength and stiffness, which contribute to its ability to replace metals and other traditional materials in demanding structural applications. In addition to its mechanical robustness, PEI exhibits excellent dimensional stability, ensuring that components retain their shape and performance even under varying thermal and mechanical loads. The polymer also has high creep resistance, further improving its suitability for long-term applications where dimensional precision is critical [191].

Another key feature of PEI is its inherent flame-retardant properties. Not only does it resist ignition but also emits very low levels of smoke when exposed to fire, making it a safer choice for applications where fire safety is a concern. The strong chemical resistance of PEI is another significant advantage, particularly against hydrocarbons, alcohols, and halogenated solvents, which allows it to perform well in harsh chemical environments. This chemical resistance, combined with its hydrolytic stability, makes PEI a reliable material for use in environments where exposure to moisture and chemicals is common [191].

PEI is used in a wide range of industries because of its properties. In the medical and healthcare sector, it is used in devices and components that require sterilization and long-term reliability. Its biocompatibility and resistance to repeated autoclaving make it an ideal material for surgical instruments, medical devices, and dental tools [192].

In the electrical and electronics industry, PEI is valued for its excellent dielectric properties and dimensional stability. It is commonly used in connectors, circuit boards, and other components where electrical insulation and precision are essential. The resistance of the polymer to high temperatures and chemical exposure further enhances its suitability for these

applications [193].

The automotive and aerospace industries benefit from PEI's high strength-to-weight ratio, flame retardancy, and resistance to high temperatures. It is used in under-the-hood components, aircraft interiors, and other structural parts where durability and safety are paramount [194, 195]. The ability of PEI to replace metals in these applications not only reduces weight but also contributes to improved fuel efficiency and overall performance [196].

Despite its good qualities, PEI also has some limitations. Its primary disadvantage is its notch sensitivity, which can create stress concentrations that may lead to mechanical failure under certain conditions. This notch sensitivity requires careful design considerations to avoid sharp corners or other features that could compromise the integrity of the material [197, 198].

Another significant limitation is the high processing temperatures required for PEI, which can complicate manufacturing processes and increase production costs. These high temperatures require special equipment and processing techniques, which can be cost prohibitive for some applications. Furthermore, the overall cost of PEI is relatively high compared to other polymers, which can limit its use in cost-sensitive industries [199].

Although it presents its challenges, PEI is a versatile polymer with excellent mechanical properties and thermal stability. Its benefits make it an invaluable material across several industries in modern manufacturing. The continued development and optimization of its processing techniques will likely expand its use even further, especially in applications where performance, reliability, and weight are critical.

Chapter 3

Additive Manufactured Polymers: Structural Characterization

As mentioned earlier, polymers, particularly high-performance polymers, are increasingly being used in structural components as a result of their exceptional strength-to-weight ratio, corrosion resistance, and versatility in design. Their ability to be molded into complex shapes and inherent durability allow for innovative engineering solutions that were previously unattainable with traditional materials such as metals.

Although not a high-performance polymer, and only for a short stratospheric flight aboard a balloon, the HERCCULES experiment [200, 201] used ABS for structural components, with satisfying results. The polymer was used for the PCB module, made entirely of ABS frames (for the PCB) and a connector panel, and only using steel spacers (Figure 3.1a), and for the custom-made union between the experiment panels and the structural frames (Figure 3.1b). It was also used for the support structures for the cables and thermistors placed in different parts of the experiment. The short duration of the flight meant that there would not be any risk of outgassing, and the highest load that the experiment would experience would be at landing, with a peak acceleration of 35g under the worst-case scenarios. The structure did not suffer internal damage, and the use of ABS helped reduce the weight of an experiment that was already beyond the limit. If a material such as ABS can withstand these loads, the possibilities of materials such as ULTEM™ are much greater, which is why it is necessary to fully understand their capabilities through mechanical tests.

Research has shown that the mechanical properties of specimens made from the same material can vary depending on the direction of the layer and the printer used [202, 203]. This is also true for high-performance polymers, where factors such as layer orientation can influence tensile strength, fracture toughness, and fatigue resistance. Thus, these characteristics must be considered when selecting materials for specific applications.

The anisotropy, or directional dependence of mechanical properties, significantly contributes to variations in properties based on printing orientation. This anisotropy is inherent in materials used in 3D printing and directly affects the performance of printed parts.

The research by Goh [204] highlights the notable difference in tensile strength based on the

(a) Electronic box with the ABS structure.

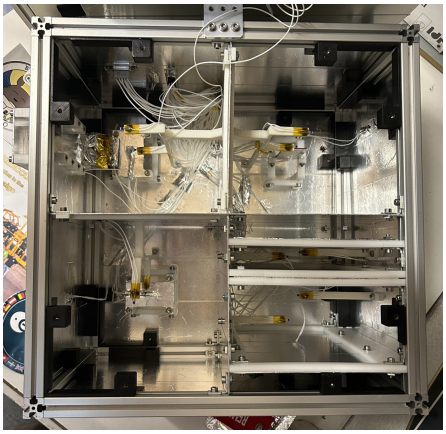

(b) Main experiment box with the custom-made unions and support components.

Figure 3.1: Componets made of ABS in the HERCCULES experiment

orientation of the printing. Samples printed vertically exhibit only 40-50% of the tensile strength of those printed flat or on edge, a substantial reduction that can impact the suitability of printed parts for certain applications.

Furthermore, the mechanical properties of a sample are significantly influenced by its shape, a crucial aspect discussed in detail by Laureto and Pierce [205]. They compared Type I and Type IV samples as defined by the ASTM D638 standard [206], which measures the tensile properties of plastics. Type I samples are larger, while Type IV samples are smaller. They found that Type IV samples tended to overestimate ultimate strength compared to Type I samples, leading to potentially inaccurate predictions of material performance in actual applications. Their findings emphasize the importance of considering the shape of the sample when evaluating mechanical properties and the need for standard testing procedures to account for these shape-dependent variations [207].

By considering these factors, designers and engineers can ensure that they select the best material for their application, achieving optimal performance. The results shown in this chapter have already been published in references [208, 209].

3.1 Testing methods and procedure

This section describes the set of tests performed to determine the mechanical properties of ULTEM™ 9085 and ULTEM™ 1010 to understand the implications of the printing direction and orientation. Four types of tests are performed to determine tensile properties (DIN EN ISO 527 [210]), flexural properties (DIN EN ISO 178 [211]), compressive properties (DIN EN ISO 604 [212], ASTM D695 [213]) and resistance to breakage by flexural shock (Charpy impact test, ASTM D6110 [214]).

3.1.1 Tensile Tests

The ISO standard 527 [210] describes up to four types of samples that can be tested, of different sizes and geometries, with different test speeds depending on the reference length of the samples. The ISO standard defines sample 1A as the standard sample for testing, but also allows for samples 1B. In cases where neither type 1 sample is possible to be used, it also allows samples 5A and 5B. For this research, samples 1A, 1B and 5A were used as samples 5B proved to be too difficult to print correctly due to their small size (35 mm long and1 mm thick). The reason for choosing to test three types of samples was to see how the geometry of the sample affects its mechanical properties. The dimensions are shown in Figure 3.2

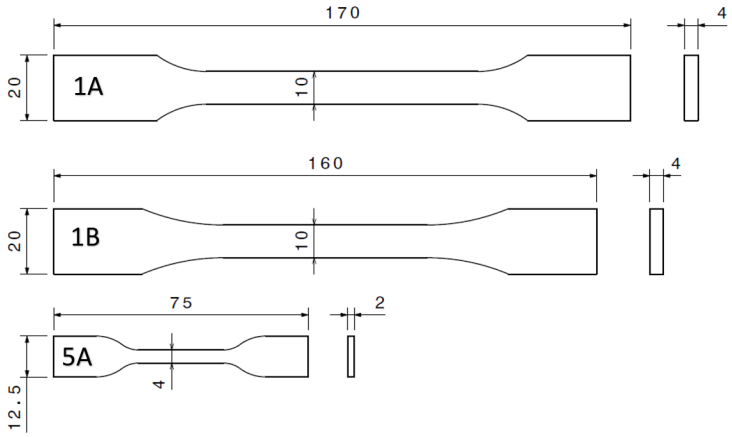

Figure 3.2: Tensile test samples' dimensions (mm).

As mentioned above, the test speed to calculate both the modulus and the rest of the curve depends on the reference length of each type of sample, according to the ISO standard [210] (as close as possible to 1%/min of the reference length). The reference length for the samples and the corresponding test speed are defined in Table 3.1.

Table 3.1: Tensile test specifications.

Sample	Reference length	Testing speed for Modulus	Testing speed after Modulus
1A	75 mm	1.00 mm/min	50 mm/min
1B	50 mm	0.50 mm/min	50 mm/min
5A	20 mm	0.25 mm/min	5 mm/ min

3.1.2 Bending Tests

For the flexural tests, the ISO standard 178 [211] only specifies one type of sample, as shown in Figure 3.3.

The standard defines the test as the three-point flexural test, as shown in Figure 3.4. The ISO standard [211] requires the reference length (L) to be 64 mm, as well as for the radius in the three points (R1 and R2) to be 5 mm.

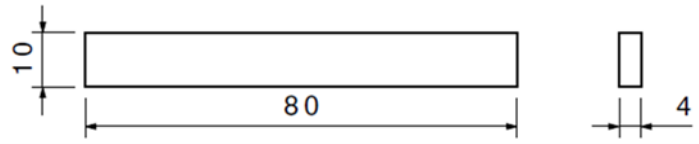

Figure 3.3: Flexural samples' dimensions (mm).

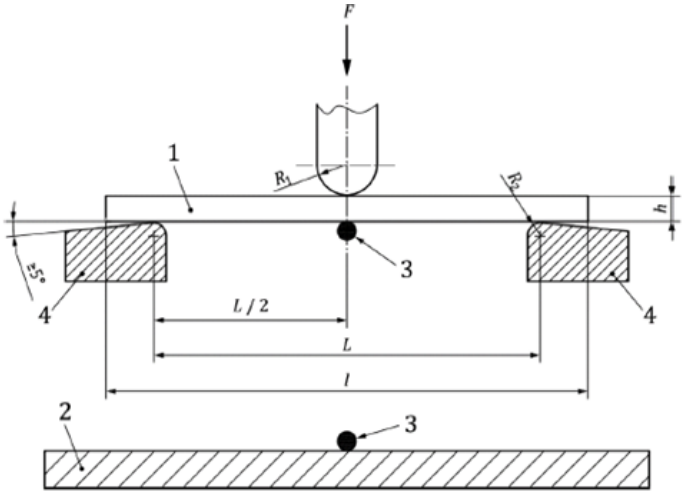

Figure 3.4: Flexural test sample positioning [211].

For the testing procedure, the standard defines two possible methods to follow. Method A establishes a constant test speed of 2 mm / min until it breaks or reaches a maximum strain of 5%. Method B establishes a test speed of 2 mm/min for the determination of the flexural modulus and 10 mm/min or 100 mm/min for the rest of the curve. For this research, method B was chosen, using a testing speed of 2 mm/min until it reaches the end of the modulus determination range ($0.05\% < \epsilon < 0.25\%$), unloads the sample and starts again at a speed of 10 mm / min.

3.1.3 Compression Tests

For compression tests, the standard followed was ASTM D695 [213], which is equivalent to ISO standard 604 [212]. The dimensions of the samples are shown in Figure 3.5. The standard states that the sample must be in the form of a right cylinder or prism whose length is twice its width/diameter. The standard specifies that the testing speed is 1.3 mm / min for the entire duration of the test.

3.1.4 Charpy Impact Tests

Regarding the Charpy impact tests, ASTM D6110 [214] and ISO 179 [215] are not equivalent, as is the case for the compression tests. This research uses the sample geometry of ASTM D6110 [214], as shown in Figure 3.6.

The Charpy Impact test is performed using a pendulum impact machine. The sample is placed

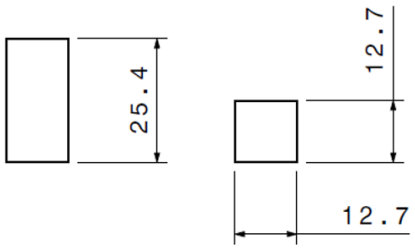

Figure 3.5: Compression samples' dimensions (mm).

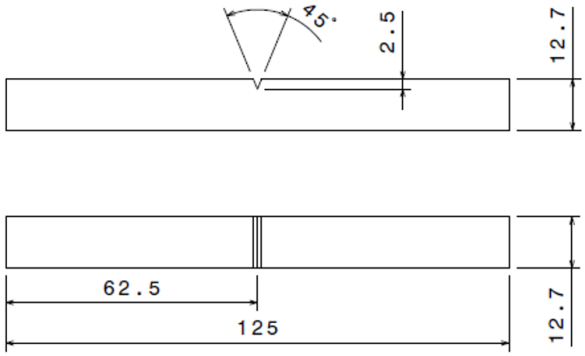

Figure 3.6: Charpy Impact test samples' dimensions (mm).

at the base with the notch looking inward after the pendulum is raised to the required height and secured, as shown Figure 3.7. After resetting the indicating mechanism, the pendulum is released, striking the center of the sample. The indicating mechanism would then show the breaking energy of that test.

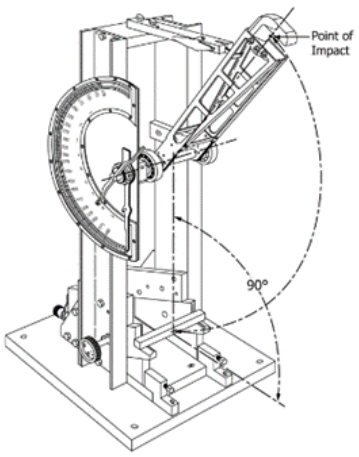

Figure 3.7: Charpy impact test configuration [214].

The impact resistance of the material (in kJ/m^2) is calculated by subtracting the friction loss energy from the indicating breaking energy and dividing it by the width of the sample.

3.2 Testing instrumentation and specimens

Tensile and flexural tests were conducted using an Instron universal testing machine equipped with extensometers and a 3000 kg load cell, in the facilities of E.T.S. de Ingeniería Aeronáutica y del Espacio (ETSIAE), affiliated to the *Universidad Politécnica de Madrid* (UPM). The compression tests were performed using a MicroTest Electromechanical Universal Testing System (EM2 series), also in the ETSIAE facilities, equipped with extensometers and 156 mm compression plates. For the impact tests, a 30 kgm Mouton pendulum from Amsler was used, in the facilities of E.T.S. de Ingeniería de Caminos, Canales y Puertos (also affiliated with UPM).

Each tensile and bending specimen was made with three different layer orientations: flat at a 45° angle, upright at a 0° angle and on-edge at a 0° angle. Furthermore, the flexural sample and specimen 1A were also printed on-edge at a 45°-layer orientation for comparison purposes. For type 1 samples, four samples were printed in each orientation, while six of each for flexural samples and tensile samples 5A were printed. In the case of compression and Charpy impact tests, three samples were printed in two different orientations for both tests. Compression samples were printed horizontally and vertically at a 45° angle, while Charpy impact samples were printed with the notch positioned sideways (H) and upright (V) at a 45° angle. The printing direction and the layer orientations are shown in Figure 3.8a and Figure 3.8b.

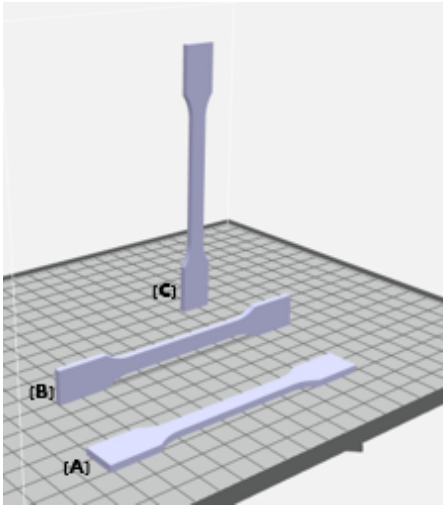

(a) Different layer direction printed: (A) flat, (B) on edge, and (C) upright

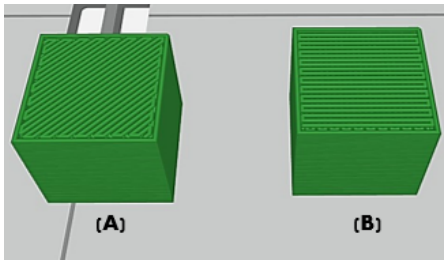

(b) Layer orientation printed: (A) +/- 45°, and (B) 0°/90°

Figure 3.8: Sample layer orientation and direction.

Datasheets obtained from material manufacturers [216, 217, 218, 219] will serve as a reference point for comparison. It is important to note that these datasheets may present variations in testing conditions, such as different standards used in America and Europe, variations in specimen dimensions/geometry, and variations in printers. It should be noted that the ULTEM™ specimens used in our study were printed using the FORTUS 450mc printer by Stratasys (see Figure 3.9), using the ULTEM™ 9085 Resin (Natural) and ULTEM™ 1010 Resin (general-purpose) from Stratasys. The provided material datasheets [216, 217]

specifically pertain to the FORTUS 900mc. Furthermore, the manufacturer's datasheet only provides information on Izod impact testing for these materials, while our study employed Charpy testing, rendering direct comparisons inappropriate.

Figure 3.9: Fortus 450mc (left) and 900mc (right) from Stratasys.

Table 3.2: Reference values [216, 217, 218, 219] of strength at break, yield strength and modulus of ULTEM™ 9085 and ULTEM™ 1010.

Material	TEST	Strength at break (MPa)	Yield Strength (MPa) (H/V)	Modulus (GPa)
ULTEM™ 9085	Tensile Flexural Compression	68.1 104 -	69.2 - 139/342	2.52 2.4 2.22/2.28
ULTEM™ 1010	Tensile Flexural Compression	80 no break -	- - 245/440	3 2.91 2.9/3.2

For ULTEM ™ 1010, the reference datasheet is obtained from CAMPUS [218], and for ULTEM™ 9085, the datasheet is obtained from MCPP [219]. The reference values for the tests can be found in Table 3.2.

The reference samples for the tensile, flexural and compression tests underwent a conditioning period of at least 40 hours at a temperature of 23 ± 2 °C (73 F ± 3.6 F) and a relative humidity of 50 ± 10% before testing, according to the Stratasys material testing procedure[220]. The information about each test is the following:

- Tensile tests followed the ASTM D638 Type I standard [221], employing a crosshead speed of 5.08 mm/min (0.2 in./min).
- For flexural mechanical tests, ASTM D790 samples [222] measuring 12.7 mm × 3.175 mm × 76.2 mm were used. Procedure A was used, with a span length of approximately 50 mm (∼ 2 in.) and a strain rate of 0.254 mm/mm/min (0.01 in./in./min).

- Compression strength tests were performed on ASTM D695 [213] rectangular prism samples measuring 12.7 mm × 12.7 mm × 25.4 mm, utilizing a crosshead speed of 1.27 mm/min (0.05 in./min). The failure was determined by the appearance of the initial tear in the sample.
- No information regarding the specific procedures for Charpy impact testing is provided.

The printer required different tips for the materials, using the T14 for the ULTEM™ 1010 and the T16 for ULTEM™ 9085. Both provide a sample of a 0.254 mm layer height. All samples were printed with a theoretical 100% infill, a single edge contour (0.508 mm thick) and a perpendicular raster pattern between layers. The printer is made for commercial purposes, so some printing parameters, such as printing speed, are fixed and impossible to change.

3.3 Results and Analysis

3.3.1 Tensile test

ULTEM™ 9085

The results of the tensile test for ULTEM™, 9085, as shown in Table 3.3, indicate that upright samples (printed at a 90° angle) exhibited a lower elastic modulus and ultimate strength compared to other samples. The best overall performance was observed in the 1A on-edge 45° samples, as illustrated in Figure 3.10.

Table 3.3: Tensile test results summary for ULTEM™ 9085 [208]. The Standard Deviation (SD) corresponding to each average value has been included in brackets next to it.

Specimen	Printing Orientation (nº of Samples)	Elastic Modulus (SD) (MPa)	Yield Strength (SD) (MPa)	Ultimate Tensile Strength (SD) (MPa)
1A	FLAT (4)	1583.25 (23.71)	33.58 (0.7)	72.72 (1.69)
	ON-EDGE 45° (4)	1488.64 (37.38)	54.41 (5.56)	81.71 (2.05)
	ON-EDGE 90° (4)	1588.14 (93.96)	36.25 (2.16)	77.03 (1.55)
	UPRIGHT (4)	1189.11 (138.64)	41.48 (4.71)	45.69 (5.30)
1B	FLAT (4)	1061.50 (2.12)	24.81 (0.35)	71.76 (0.58)
	ON-EDGE (4)	1070.35 (11.75)	21.97 (2.31)	78.23 (0.48)
	UPRIGHT (4)	992.22 (37.36)	22.43 (2.92)	46.68 (1.82)
5A	FLAT (6)	1219.83 (68.43)	22.97 (6.7)	82.99 (1.62)
	ON-EDGE (6)	1265.67 (85.65)	21.10 (12.18)	90.92 (3.00)
	UPRIGHT (6)	1185.87 (55.10)	31.07 (1.69)	43.87 (6.24)

The elastic modulus of the 1A flat and on-edge samples was higher compared to the 1B and 5A samples. However, the upright sample showed the same modulus as the 5A sample, despite having higher yield and ultimate stress but smaller deformation at break. While the yield stress was greater in the 1A samples, the highest ultimate strength at break was observed in the 5A samples. Overall, better tensile mechanical properties were achieved when the samples were printed on-edge.

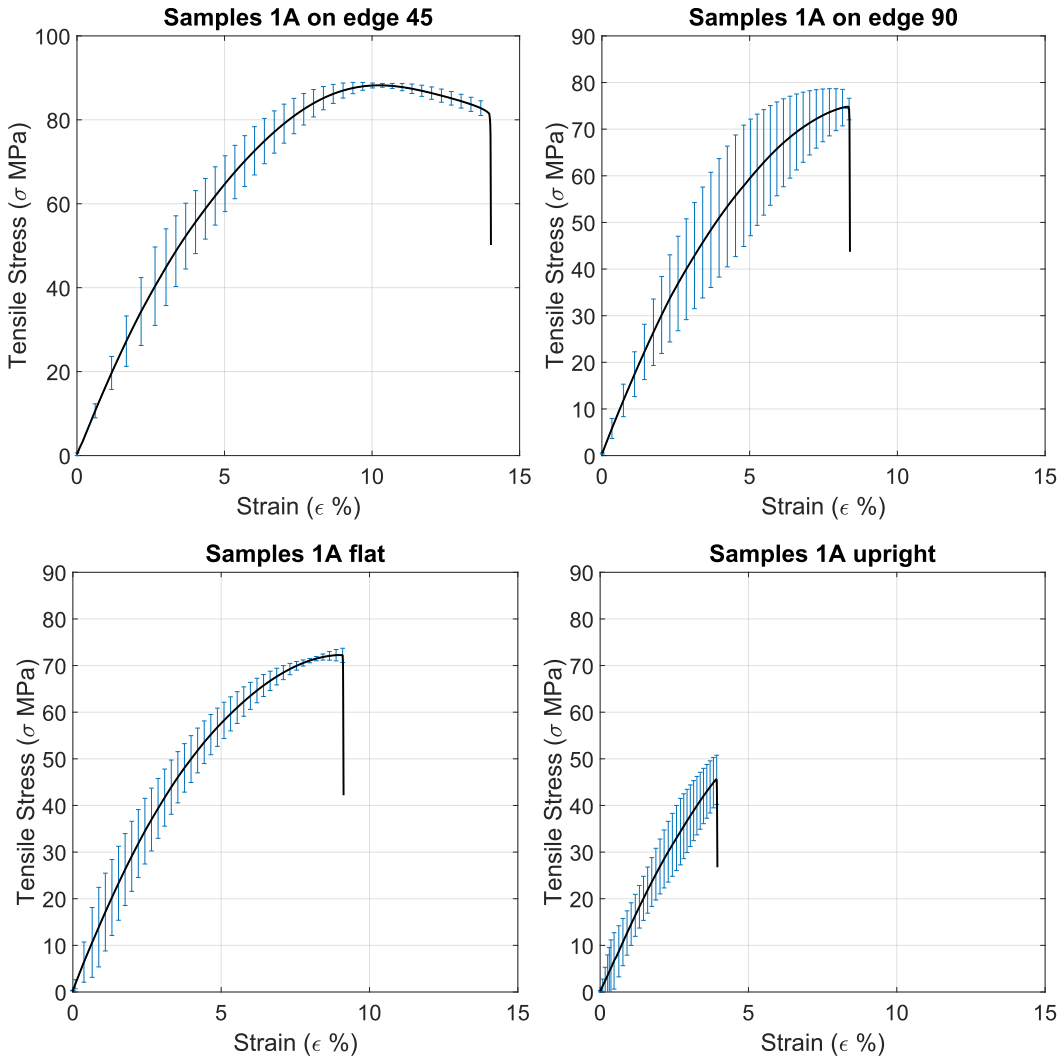

Figure 3.10: ULTEM™ 9085 average results and standard deviation for all 1A samples.

Among the various orientations tested for the 1A samples, the on-edge 90° configuration yielded the highest elastic modulus, while the on-edge 45° showed superior ultimate strength and yield strength. For the 1B samples, the on-edge orientation resulted in the highest elastic modulus and ultimate strength, whereas the flat orientation exhibited the highest yield strength. In the 5A samples, the on-edge specimens achieved the best elastic modulus and ultimate tensile strength, with the upright orientation displaying the highest yield strength. Overall, the on-edge samples consistently demonstrated superior performance across these tests.

According to the datasheet provided by STRATASYS [216], the ultimate tensile strength of the on-edge 45° samples was higher than the reference values, while the yield strength and modulus were lower. Comparing with other authors, Padovano et al. [223] reported a nearly identical yield strength for the on-edge 45° specimens (100% infill), although their ultimate strength is slightly lower and their Young's modulus is 0.9 GPa higher. Both Kaplun [224]

and Zaldivar [225] investigated the properties of ULTEM™, 9085 in flat (0°), on-edge (45°), and upright (90°) specimens (using ASTM type 1 samples). Their tensile strength results are lower than those presented here, while their Young's modulus values are higher, approaching the datasheet value. Zaldivar reports a low Young's modulus of 1770 MPa for the on-edge 45° samples, which is closer to the 1488 MPa obtained here than to the datasheet value of 2520 MPa. Their ultimate tensile strength values for the flat and on-edge samples are considerably lower (46.83 MPa and 47.52 MPa, respectively).

Figure 3.10 to Figure 3.12 show the average curves for each orientation of the three types of samples. The curves for samples 1B and 5A exhibit a more similar trend to each other (with different failure points) compared to the curves for the 1A samples.

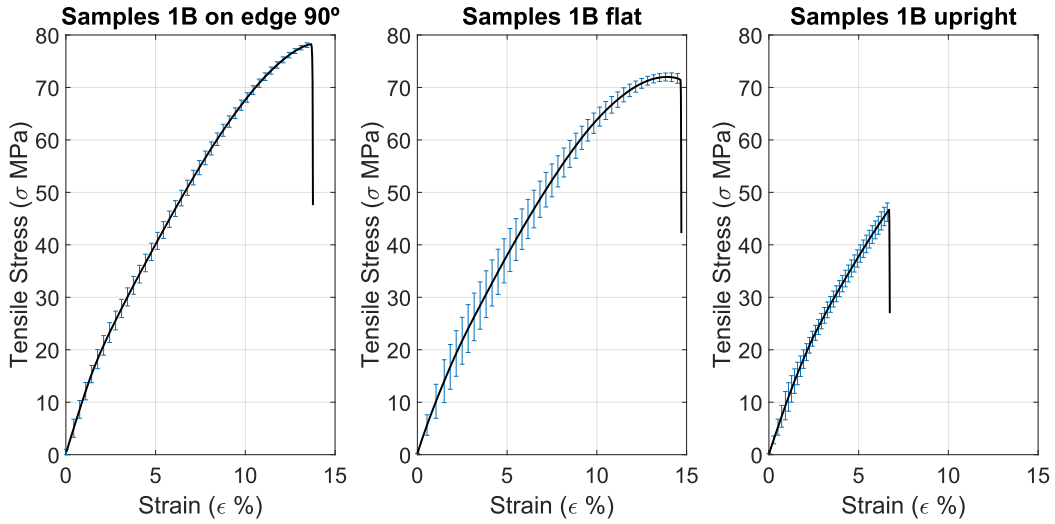

Figure 3.11: ULTEM™ 9085 average results and standard deviation for all 1B samples.

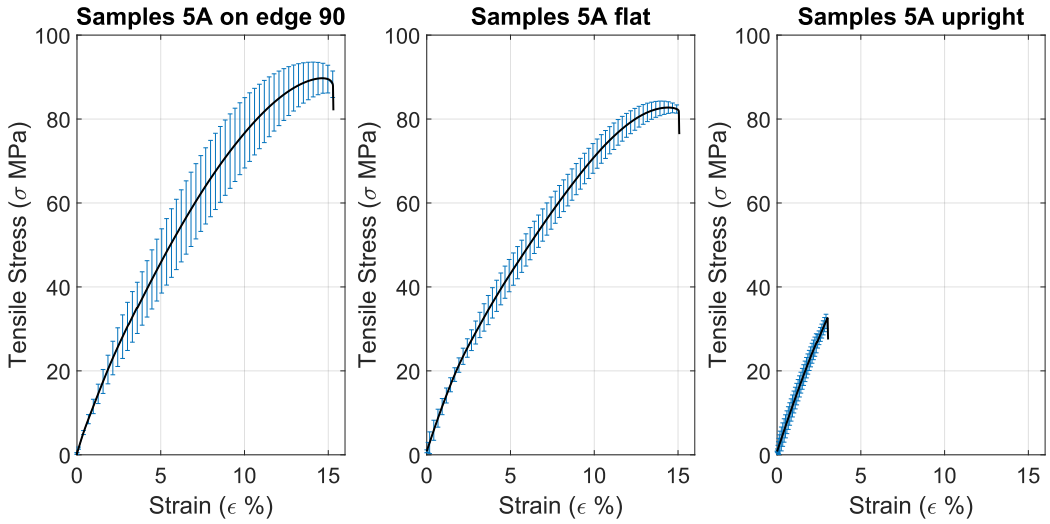

Figure 3.12: ULTEM™ 9085 average results and standard deviation for all 5A samples.

During tensile testing of the 5A on-edge samples for ULTEM™, 9085, some issues arose where the layers of the specimen began to separate rather than breaking. This led to a different appearance in the test results compared to other samples. The test was not stopped when the layers began to separate to determine if the sample would eventually break, so the exact strain at break is only an estimate.

Figure 3.13: On-edge 5A samples showing the deformation suffered during testing.

A picture of the 5A samples is shown in Figure 3.13. The wall layer separated, not the filling, and the sample fractured perpendicular to the layer deposition after being stretched excessively. In some instances, the total length of the sample extended from 75 mm to nearly 90 mm.

ULTEM™ 1010

The tensile test results for ULTEM™, 1010, as shown in Table 5, indicate that the elastic modulus was similar for the 1A and 5A samples but lower for the 1B samples. The yield strength was comparable between the 1A and 1B samples but higher for the 5A samples. The ultimate strength was also similar for the 1A and 1B samples. Overall, the modulus results were fairly consistent among the same type of specimen.

Examining each type of sample (see Figure 3.14 to Figure 3.16), it is evident that the 1B and 5A samples exhibit similar curves across the three orientations, with the exception of the upright 5A sample. In the 5A samples, only the flat and on-edge curves are nearly identical, though the on-edge sample fails earlier than the flat sample. For the 1B samples, the curves are also similar but with varying failure points, with the upright samples failing much earlier. Across all three sample types, the flat samples demonstrate the latest fracture points, which coincide with the ultimate tensile strength.

The difference in elastic modulus between the ULTEM™, 1010 sample types in both materials is notable. While the elastic modulus is an intrinsic material property and should not be directly influenced by shape, the anisotropic nature of these materials—with properties that vary depending on direction—means that shape can influence the orientation of stress relative to the material's natural stiffness directions. This can result in variations in the elastic modulus based on the loading direction relative to the material's geometry. Specimens 1A and 5A exhibit a shorter (and more similar) curved region compared to specimen 1B, which may influence the perceived stiffness of the samples. Since the curved regions are not identical

Table 3.4: Tensile test results summary for ULTEM™ 9085 [208]. The Standard Deviation (SD) corresponding to each average value has been included in brackets next to it.

Specimen	**Printing Orientation (nº of Samples)**	**Elastic Modulus (SD) (MPa)**	**Yield Strength (SD) (MPa)**	**Ultimate Tensile Strength (SD) (MPa)**
1A	FLAT (4)	1435.96 (75.75)	15.57 (3.19)	71.85 (0.84)
	ON-EDGE 45°(4)	1540.30 (33.65)	15.69 (4.15)	76.26 (2.13)
	ON-EDGE 90° (4)	1553.01 (29.69)	19.47 (2.22)	64.51 (8.73)
	UPRIGHT (4)	1447.77 (79.96)	12.23 (2.52)	35.00 (14.12)
1B	FLAT (4)	1005.33 (18.07)	15.04 (1.76)	73.58 (0.83)
	ON-EDGE (4)	1020.07 (20.03)	16.81 (1.79)	59.25 (2.59)
	UPRIGHT (4)	1077.44 (15.15)	14.21 (0.81)	41.11 (12.27)
5A	FLAT (6)	1459.88 (41.44)	28.14 (2.95)	103.37 (1.72)
	ON-EDGE (6)	1452.81 (24.21)	29.78 (7.59)	93.37 (5.81)
	UPRIGHT (6)	1254.25 (33.73)	27.13 (3.99)	47.99 (1.67)

between the sample types, this may explain the difference observed between 1A and 5A in the ULTEM™, 9085 results.

Among the various orientations tested for the 1A samples, the on-edge 90° configuration exhibited the best elastic modulus and yield strength, while the on-edge 45° (as shown in Figure 3.16) demonstrated superior ultimate strength. The flat sample, on the other hand, showed higher deformation at break. Overall, the results for this sample type were consistent, with low standard deviation and uniform behavior.

In the 1B samples, the upright orientation resulted in the highest elastic modulus, the on-edge orientation had the highest yield strength, and the flat orientation achieved the highest ultimate strength. For the 5A samples, the flat specimens performed best in terms of elastic modulus and ultimate tensile strength, while the on-edge specimens showed the highest yield strength. There was little correlation between the results and behavior of the different sample types, except for the yield strength, which was consistently higher in the on-edge 90° samples. This may be attributed to the anisotropic properties of the material.

As with ULTEM™, 9085, the comparison to the datasheet is based on the on-edge 45° orientation. In tensile tests for ULTEM™, 1010, the tested samples performed worse elastically compared to the datasheet, with the average elastic modulus being only half of what was reported. However, the ultimate strength was similar to the datasheet values, while the deformation at break was higher in our tests. The sample is also not expected to yield. Pandelidi [226], in their research, examined the tensile strength and modulus of ULTEM™, 1010 specimens in both flat and on-edge configurations. Their results for modulus were approximately 0.5 GPa lower than the values presented here, while the tensile strength ranged between 4 and 14 MPa lower.

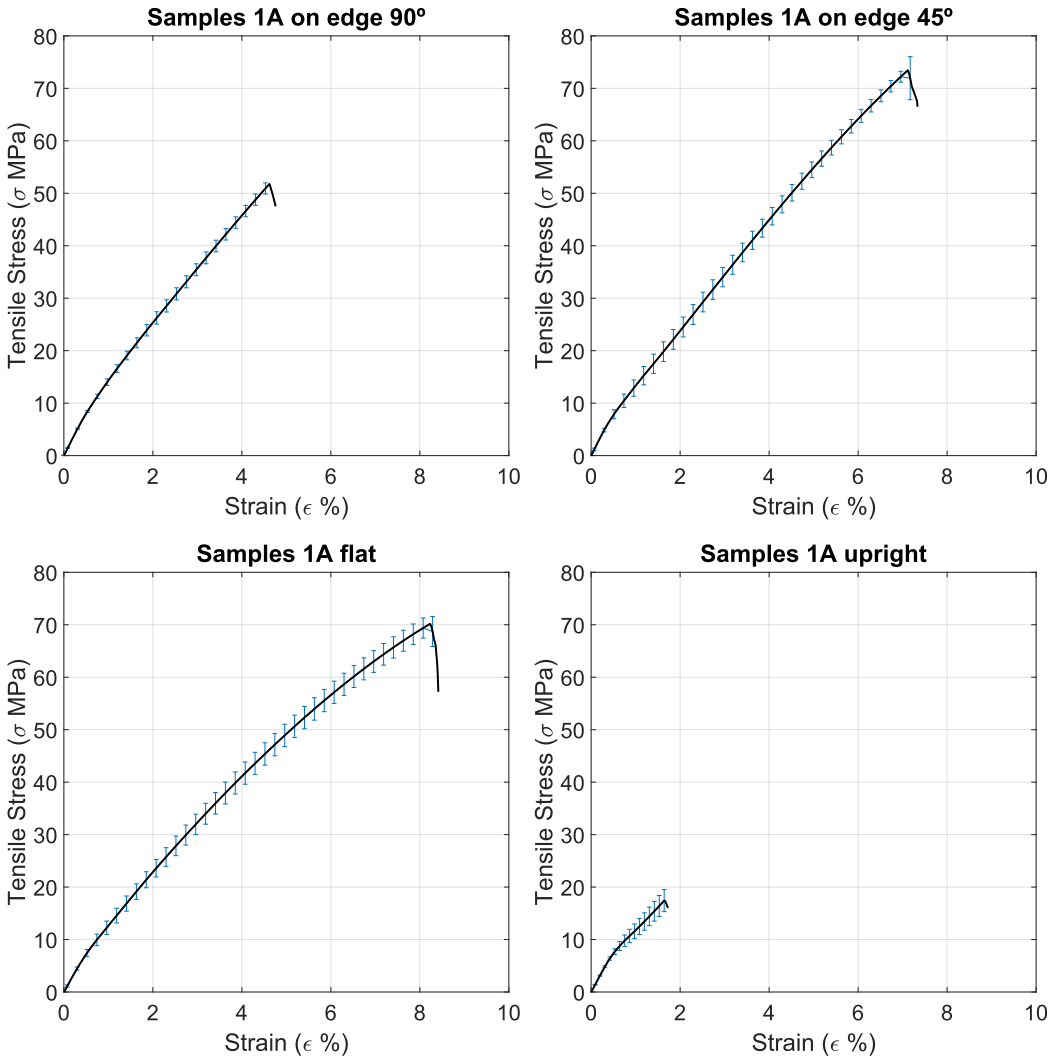

Figure 3.14: ULTEM™ 1010 average results and standard deviation for all 1A samples.

3.3.2 Flexural test

ULTEM™ 9085

The flexural tests (Table 3.5 and Figure 3.17) yield results consistent with those of the tensile tests. The upright specimens performed worst overall, while the on-edge specimens, particularly those oriented at 45°, showed the best performance. The on-edge 45° sample was the only one that did not break, although one sample in this batch did crack. The on-edge 90° samples also did not break apart.

Compared to the datasheet, the flexural modulus obtained from the on-edge 45° samples was higher than the reference value, as was the flexural strength. In both the tests and the datasheet, the samples did not break, as shown in Figure 3.18a. In Figure 3.18b, the on-edge 90° samples exhibit cracking, but without complete fracture. In the study conducted by Byberg [227], the flexural strength values were lower than those obtained here. The closest

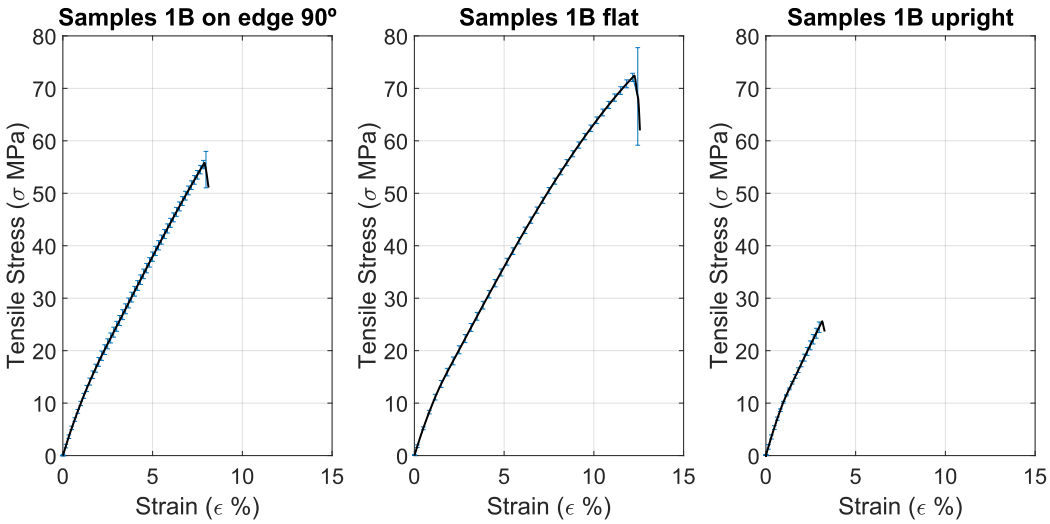

Figure 3.15: ULTEM™ 1010 average results and standard deviation for all 1B samples.

Table 3.5: Flexural results summary for ULTEM™ 9085 [208]. The Standard Deviation (SD) corresponding to each average value has been included in brackets next to it.

Printing Orientation (nº of Samples)	**Elastic Modulus (SD) (MPa)**	**Flexural Strength (SD) (MPa)**
FLAT (6)	2692.94 (95.60)	137.88 (4.63)
ON-EDGE 45º (6)	3260.20 (77.17)	155.04 (3.05)
ON-EDGE 90º (6)	2974.15 (51.25)	133.46 (0.98)
UPRIGHT (6)	2111.47 (92.70)	78.38 (13.38)

match was found in the on-edge 90° samples, with a variation of 7.5%, while the largest discrepancy occurred in the on-edge 45° samples, with a 25.5% variation.

ULTEM™ 1010

Regarding the flexural tests of ULTEM™, 1010 (see Table 3.6), the on-edge 90° samples exhibit the highest elastic modulus, in contrast to ULTEM™, 9085, where the on-edge 45° samples had the highest elastic modulus. However, the on-edge 45° samples for ULTEM™, 1010 do show the highest flexural strength.

In Figure 3.19 it is evident that the upright and flat samples exhibit a similar trend, which is also reflected in their comparable elastic modulus. However, the upright samples fail earlier, indicating lower flexural strength. The on-edge 45° samples demonstrate consistent results with minimal variation.

Compared to the datasheet, the on-edge 45° sample shows a lower value. Similar to the tensile tests, the primary difference is in how the on-edge 45° samples fail (as shown in Figure Figure 3.20), whereas the samples from Stratasys did not break. For the upright sample, which does break according to the datasheet, the flexural strength is comparable to our results. For samples that do not break, the datasheet provides the strength at 5% strain (130 MPa),

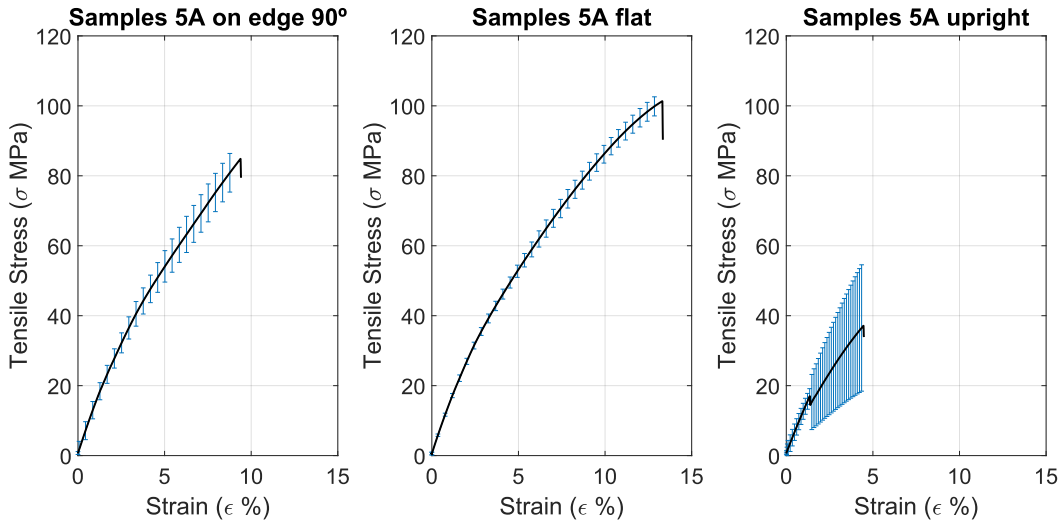

Figure 3.16: ULTEM™ 1010 average results and standard deviation for all 5A samples.

Table 3.6: Flexural results summary for ULTEM™ 1010 [208]. The Standard Deviation (SD) corresponding to each average value has been included in brackets next to it.

Printing Orientation (nº of Samples)	**Elastic Modulus (SD) (MPa)**	**Flexural Strength (SD) (MPa)**
FLAT (6)	2508.92 (134.43)	136.85 (6.83)
ON-EDGE 45° (6)	2667.02 (210.12)	181.35 (4.30)
ON-EDGE 90° (6)	3400.33 (78.63)	148.91 (7.39)
UPRIGHT (6)	2512.05 (598.55)	89.07 (10.82)

which we can use for comparison with our results. The on-edge 45° samples exhibit higher strength at this point than the datasheet value.

Both Taylor [228] and Pandelidi [226] investigated the flexural properties of ULTEM™, 1010. Their research yields similar modulus values to those presented here, with the exception of the on-edge 90° samples. They report moduli of 2.4 GPa and 2.5 GPa, compared to the 3.4 GPa presented in this study. Taylor's yield strength values closely match our findings, while Pandelidi's flexural strength values are lower, notably showing about 60% of the value reported for the on-edge 90° samples.

3.3.3 Compression test

ULTEM™ 9085

The compression tests for ULTEM™, 9085 reveal that the flat samples reach maximum stress at yield, exhibiting typical behavior of tough and durable plastics. In contrast, the upright samples remain in the plastic region for a longer period and achieve better results, likely due to the direction of the force and the interlayer bonding of the specimens. The upright

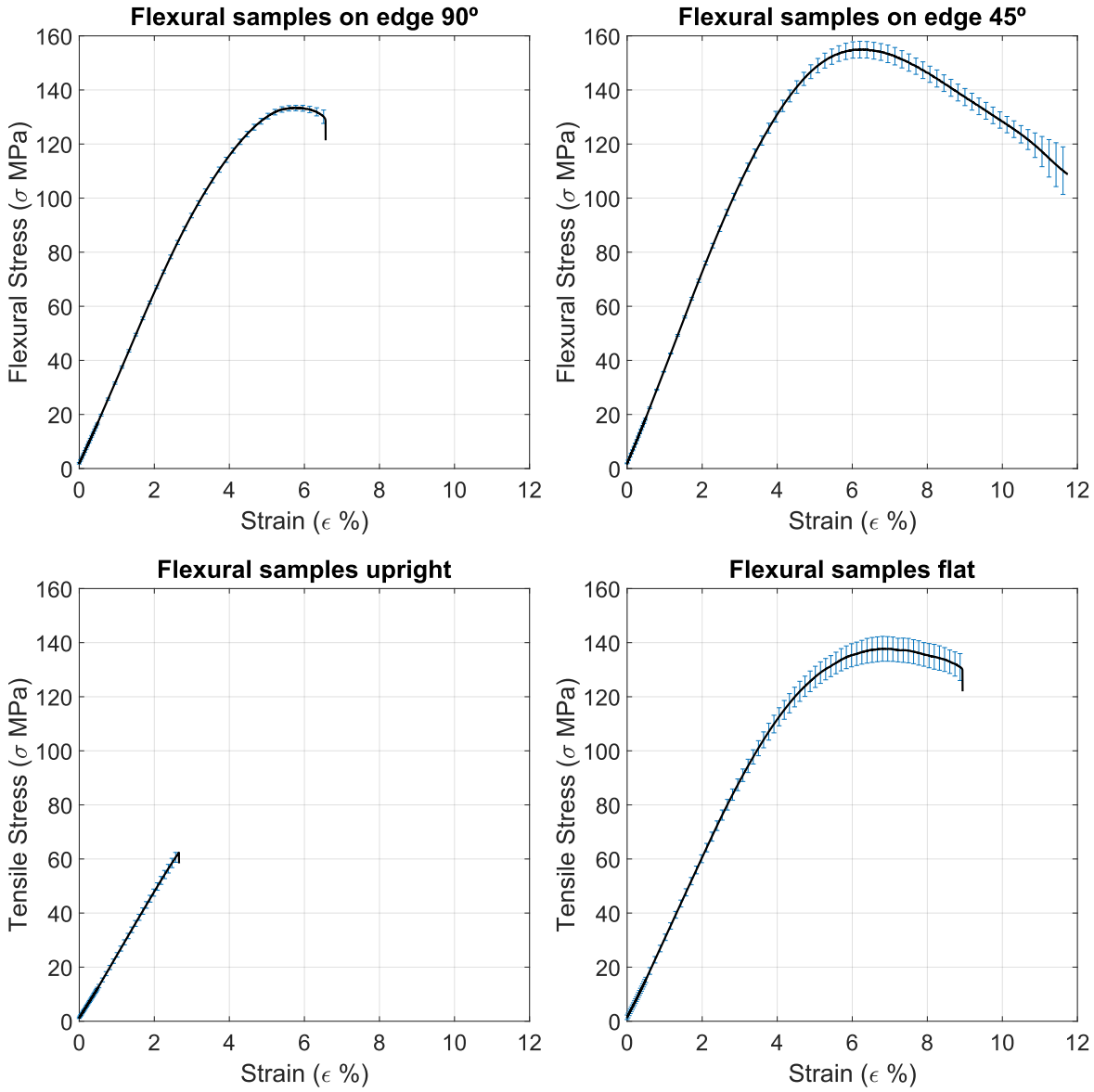

Figure 3.17: ULTEM™ 9085 average results and standard deviation for all flexural samples.

samples show slight strain hardening as stress increases beyond the yield point. Two of the samples break upon reaching ultimate strength without a decrease in stress, while the third sample continues to deform. The average results for the tests can be seen in Table 3.7 and Figure 3.21. Figure 3.22 shows the samples after testing.

Byberg [227] also investigated the compressive strength of ULTEM™, 9085 samples, although they used 10 × 10 × 4 mm specimens. Their research found compressive strength values that were nearly double those obtained in this study for the horizontal samples, while the increase for the upright samples was 30%.

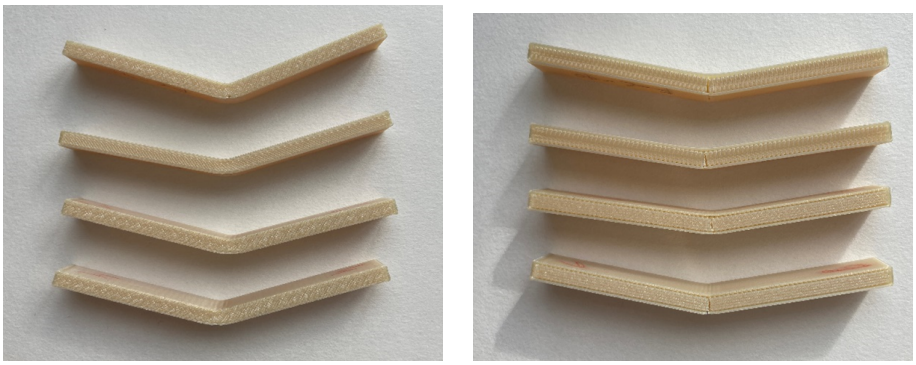

(a) Flex. sample On-edge 45° (b) Flex. sample On-edge 90°

Figure 3.18: On-edge flexural samples

Table 3.7: Compression Test results for ULTEM™ 9085 [208]. The Standard Deviation (SD) corresponding to each average value has been included in brackets next to it.

Printing Orientation (nº of Samples)	**Elastic Modulus (SD) (MPa)**	**Yield Strength (SD) (MPa)**
FLAT (3)	906.67 (0.21)	46.10 (4.87)
UPRIGHT (3)	1089.63 (0.46)	63.73 (6.47)

ULTEM™ 1010

The compression tests for ULTEM™, 1010 show similar results to those for ULTEM™, 9085, with the upright samples performing better, as seen in Table 3.8. This improved performance is likely due to the same reasons as for ULTEM™, 9085. The flat samples also maintained a constant compressive strength until failure, whereas the upright samples began to break internally, causing the machine to miss the failure (see Figure 3.23). Figure 3.24 displays the samples after testing, showing how two of the flat samples broke apart.

Table 3.8: Compression test results for ULTEM™ 1010 [208]. The Standard Deviation (SD) corresponding to each average value has been included in brackets next to it.

Printing Orientation (nº of Samples)	**Elastic Modulus (SD) (MPa)**	**Yield Strength (SD) (MPa)**
FLAT (3)	1854.17 (60.75)	99.16 (2.46)
UPRIGHT (3)	2024.73 (86.27)	123.30 (3.77)

In both materials, shear bands are observed, which are precursors to failure due to their tendency to concentrate stress and propagate, potentially leading to fractures or other forms of mechanical degradation. Shear bands are commonly seen in polymers subjected to compressive forces, forming when the material undergoes shear strain beyond its yield point. In these

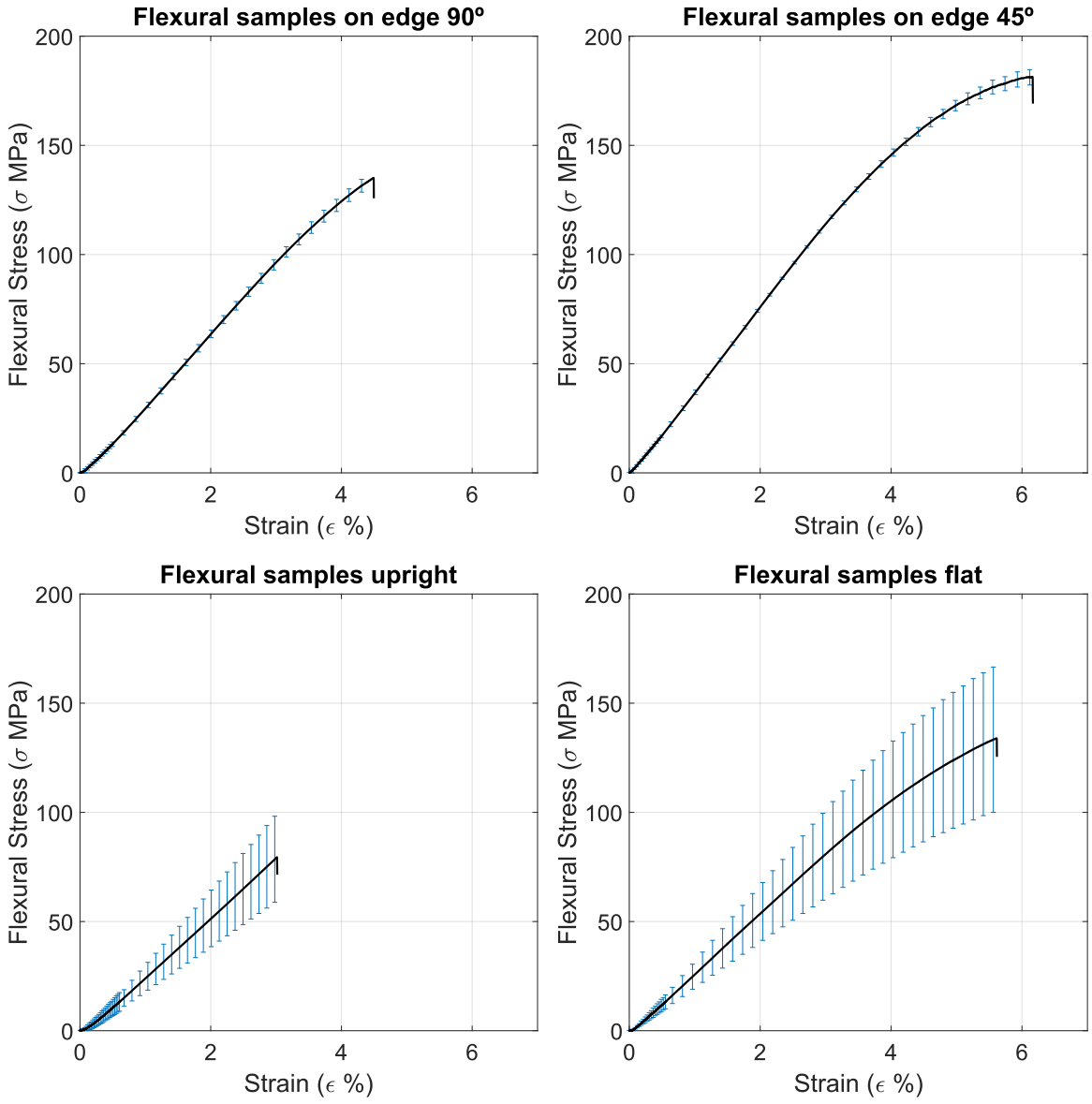

Figure 3.19: ULTEM™ 1010 average results and standard deviation for all flexural samples.

tests, small stress-relieving cracks nucleate within the polymer parallel to the direction of maximum shear stress, typically at an angle of 45°.

3.3.4 Charpy Impact Test

ULTEM™ 9085

Regarding the Charpy impact test, since the Stratasys datasheet [216] does not provide relevant information, the MCPP datasheet [219] was used for comparison. This datasheet lists a constant value of 11 kJ/m^2, which is consistent with other datasheets. The tests performed, as shown in Table 3.9, resulted in lower values, approximately 6 kJ/m^2, with the upright

Figure 3.20: Flex. sample On-edge 45°.

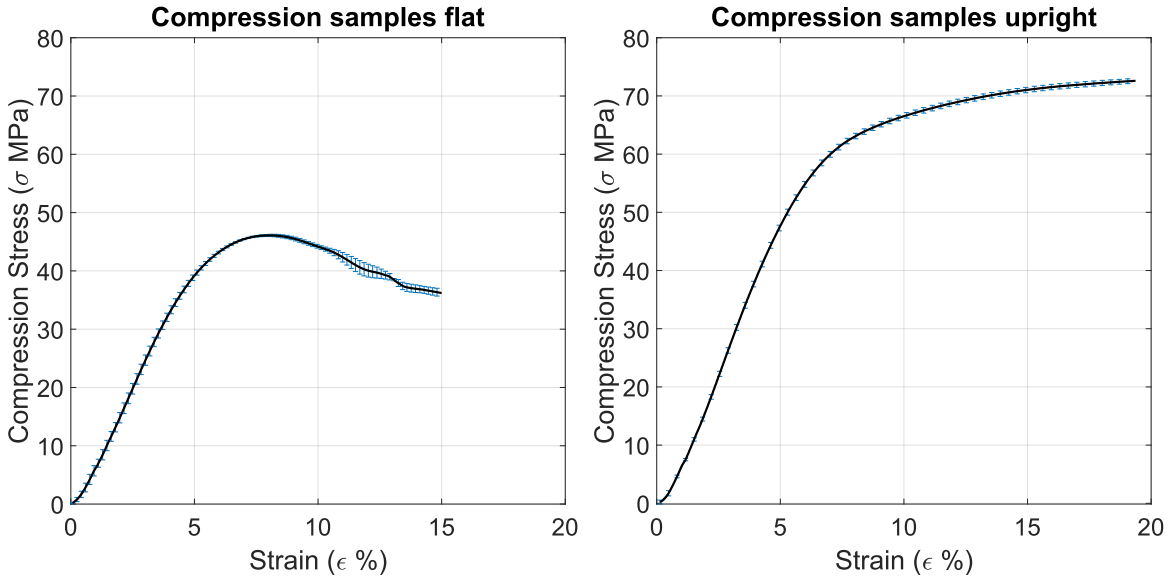

Figure 3.21: Compression test results, average, for ULTEM™ 9085.

Figure 3.22: ULTEM™ 9085 compression samples. Flat sample on left, upright sample on right.

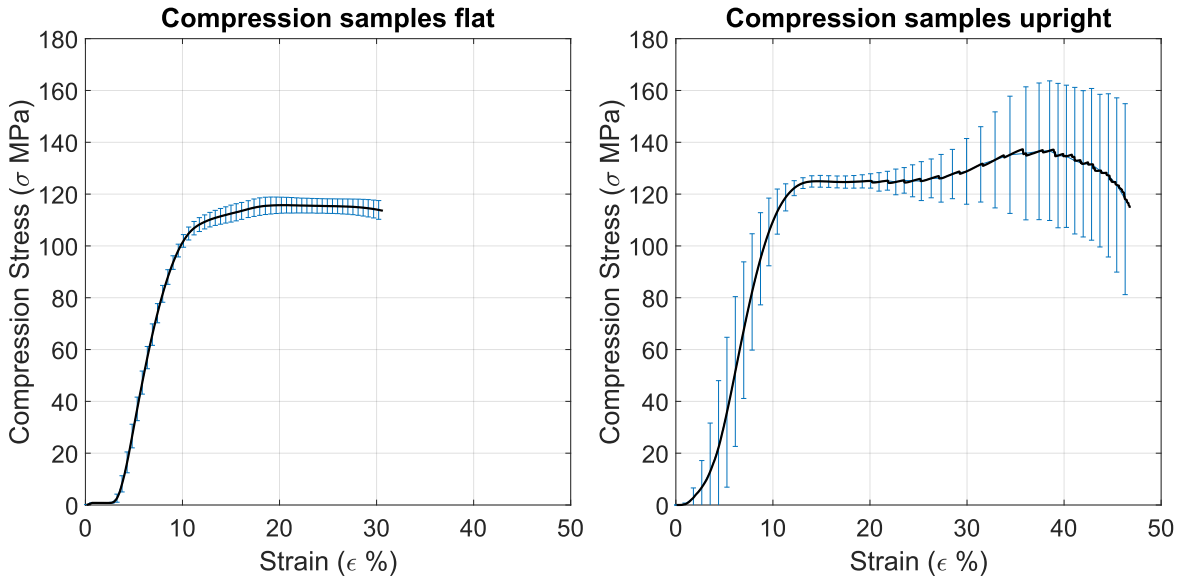

Figure 3.23: Compression test results, average, for ULTEM™ 1010.

Figure 3.24: ULTEM™ 1010 compression samples. Upright samples on top, flat on bottom.

samples exhibiting higher energy absorption. Figure 3.25 displays a sample of each type after testing.

Table 3.9: Charpy Impact results summary for ULTEM™ 9085.

Printing Orientation (nº of Samples)	**J/m**	**kJ/m²**	**Standard Dev. (kJ/m²)**
NOTCH SIDEWAYS (H)	72.20	5.59	0.694
NOTCH UPRIGHT (V)	78.72	6.19	1.259

ULTEM™ 1010

For the Charpy impact test, a similar approach was taken as with ULTEM™, 9085, using the CAMPUS datasheet for reference. The datasheet lists an impact test value of 4 kJ/m^2, which is consistent with our test results. As shown in Table 3.10, the results are similar for

Figure 3.25: ULTEM™ 9085 Charpy Impact samples, notch sideways (left) and notch upright (right).

both orientations, but in this case the sideways samples achieve a higher result. Figure 3.26 displays the specimen after testing.

Table 3.10: Charpy Impact results summary for ULTEM™ 1010.

Printing Orientation (nº of Samples)	**J/m**	**kJ/m²**	**Standard Dev. (kJ/m²)**
NOTCH SIDEWAYS (H)	51.72	4.11	1.782
NOTCH UPRIGHT (V)	51.37	4.08	1.746

Figure 3.26: ULTEM™ 1010 Charpy Impact samples, notch sideways (top) and notch upright (bottom).

3.3.5 Fractures in ULTEM™ 1010

During the tensile and flexural tests of ULTEM™, 1010 samples, an interesting observation emerged: rather than breaking into two distinct pieces, some samples fractured into 3, 4, or 5 parts, as shown in Figure 3.27. Typically, these additional fragments were small pieces surrounding the primary breaking point. This phenomenon is likely due to the release of energy upon fracture, given that the mechanical properties of these samples are quite similar. In contrast, such fragmentation was not observed with ULTEM™, 9085.

The occurrence of multiple fragments does not appear to be strongly influenced by the orientation of the sample. It was observed in specific instances of the flat and on-edge 90° samples of types 1A and 1B during tensile tests, as well as in flat, on-edge 90°, and on-edge 45° samples during flexural tests. In particular, upright samples and Type 5A samples did not fracture into multiple pieces. This is surprising, as theoretically upright samples and Type 5A samples should be more susceptible to fracture due to layer deposition (for upright samples) and reduced thickness (for Type 5A samples).

These findings suggest that the fracture behavior of ULTEM™, 1010 samples can exhibit complex patterns, with some samples showing multiple fragments upon failure. Further investigation is needed to fully understand the underlying mechanisms contributing to this phenomenon and its implications for practical applications.

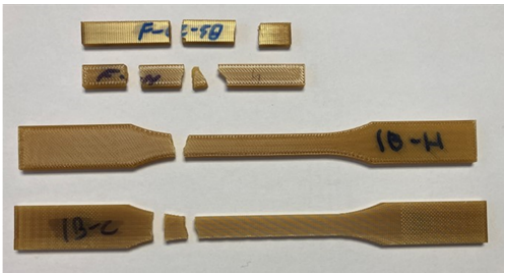

Figure 3.27: Broken ULTEM™ 1010 samples.

3.3.6 Differences with the datasheet

The samples used in the materials testing procedure conducted by STRATASYS differed from those in this study, except for the compression tests, which followed the same specifications. Differences in sample types, testing procedures, printing parameters, and methods (such as printing all samples at once versus individually) could contribute to variations in the observed mechanical properties. Printing multiple samples in a single batch may increase the printing time and potentially lead to thermal degradation. Additionally, higher testing speeds can result in higher measured strength values as a result of the strain-hardening effect, while factors such as aging and environmental conditions can influence Young's modulus.

Another critical factor is the influence of porosity on the mechanical properties of 3D-printed samples [229]. The research by Wang et al. [230] showed that samples with lower porosity tend to exhibit better mechanical properties. The location of the pores was found to be more critical than their quantity [231]. Since the porosity of the samples was not measured and the datasheet provides limited information on sample porosity, this could be another factor that contributes to deviations from the reference values. Future work should include porosity measurements to better understand its impact.

It is also important to note that polymers have unique properties that can affect mechanical testing. Reproducibility between different batches or laboratories can be challenging, making detailed reporting of test conditions essential. Polymers are temperature-sensitive, and their mechanical properties can change with temperature. Conducting tests at various temperatures and using controlled environments before and during testing, while also managing humidity (which can degrade properties over time), could help reduce variability. Aging and fatigue tests are also recommended under various loading conditions to better understand the long-term performance of the material and establish S-N curves.

Chapter 4

Analytical model for microperforated panels

This chapter outlines the mathematical process used to derive the theoretical acoustic absorption and explores how various design parameters of microperforated panels influence the acoustic absorption curve. Then it presents the methodology used for the acoustic testing, detailing the panels tested, and showcasing the results obtained.

4.1 The model of Maa

As has been described in section (State of the Art), sometimes the noise can be controlled at the source. However, in cases such as closed spaces (inside a rocket fairing, for example), it could be needed to reduce the reverberation time to appropriately mitigate the noise. Modifying the reverberation time involves controlling the sound that arrives by propagation through air at the surface or point of measurement. One of those noise control techniques is absorption, which is generally the case to use some types of acoustic materials specifically designed to absorb sound. Microperforated panels are passive absorbers that can dissipate sound energy as heat, usually effective for reducing medium- and high-frequency noise.

The absorption mechanism of a porous material is very simple. If the porous material is placed in the path of an acoustic wave, part of the energy is dissipated into heat when the acoustic waves impinge through the holes, whereas the rest of the energy is transmitted or reflected. The percentage of energy absorbed is called absorption coefficient, , and it is a function of the frequency.

In a perforated panel, the energy dissipation of the sound waves is produced by viscous thermal losses inside the perforations, this effect being enhanced by reducing the diameter of the perforations. Microperforated panels (MPPs) have arisen for this reason [26]

If an MPP is located in front of a rigid wall, it acts as a resonator. It could be compared to Helmholtz resonator, but they can be tuned to provide the maximum of absorption in a determined resonance frequency, covering a wide frequency range. The MPP can be considered

as a lattice made up of short and narrow tubes whose diameters are very small compared with their separation distances, but the latter is yet smaller than the wavelength of impinging sound waves. If the distance between the perforations is large compared to the diameter of the perforation, then the acoustic impedance of the panel can be approximated by the impedance of the individual hole divided by the number of holes in the MPP. If these conditions are fulfilled, the expression of a sound wave in a tube proposed by Rayleigh [79] and simplified by Crandall [77] for short tubes can be used. Therefore, the equation representing the aerial motion of a short tube compared to the wavelength is

$$\rho\dot{u} - \frac{\eta}{r_1} - \frac{\partial}{\partial r_1}(r_1\frac{\partial u}{\partial r_1}) = \frac{\Delta p}{t}, \tag{4.1}$$

where ρ is the density of the air, η is the dynamic viscosity of the air, t is the thickness of the panel (tube length), and u is the axial particle velocity of the air in the tube.

As we assume that the pressure difference between the two ends is Δp, that the panel is a circuit and the wave is sinusoidal, which means that we may take the time derivative as $j\omega$, which leaves:

$$(\frac{\partial^2}{\partial r_1^2} + r_1\frac{\partial u}{\partial r_1} + k^2)u = \frac{\Delta p}{\eta t}, \tag{4.2}$$

where

$$k^2 = -\frac{j\omega\rho}{\eta}. \tag{4.3}$$

Equation 2 can be identified as the Bessel differential equation, which has the following solution:

$$y = AJ_0(x),$$

where J_0 is the Bessel function of the first kind and of the zeroth order. As the velocity on the tube wall ($r_1 = r_0$) must be zero, the solution for the velocity of the particles is the following:

$$u(r_1) = -\frac{\Delta p}{\eta k^2 t}\left(1 - \frac{J_0(kr_1)}{J_0(kr_0)}\right). \tag{4.4}$$

The average velocity inside the tube will then be

$$\bar{u} = \frac{2}{r_0^2}\int_0^{r_0} r_1 u(r_1) dr_1 = \frac{2}{r_0^2}\frac{\Delta p}{\eta k^2 t}\int_0^{r_0} r_1\left[1 - \frac{J_0(kr_1)}{J_0(kr_0)}\right] dr_1. \tag{4.5}$$

Knowing that:

$$\int xJ_0(x)dx = xJ_1(x),$$

we find that the equation for the average velocity will be:

$$\bar{u} = \frac{-\Delta p}{\eta k^2 t}\left[1 - \frac{2}{kr_0}\frac{J_1(kr_0)}{J_0(kr_0)}\right]. \tag{4.6}$$

The ratio of pressure change (Δp) to average velocity gives the specific acoustic impedance of the MPP:

$$Z_1 = \frac{\Delta p}{\bar{u}} = j\omega\rho t\left[1 - \frac{2}{kr_0}\frac{J_1(kr_0)}{J_0(kr_0)}\right]^{-1}. \tag{4.7}$$

If we take:

$$kr_0 = x\sqrt{-j},$$

where x is the perforation constant

$$x = r_0\sqrt{\frac{\rho\omega}{\eta}} = d\sqrt{\frac{\rho\omega}{4\eta}} \tag{4.8}$$

then

$$Z_1 = j\omega\rho t\left[1 - \frac{2}{x\sqrt{-j}}\frac{J_1(x\sqrt{-j})}{J_0(x\sqrt{-j})}\right]^{-1}. \tag{4.9}$$

The values of Z_1 when x is small (x<1) and large (x>10) were approximated by Crandall [77]. In the first case, we can use the series expansion for J_0 and J_1 (only the first three terms). Using Equation (4.7) and taking $a = kr_0$ we have that:

$$J_0(a) = 1 - \frac{a^2}{4} + \frac{a^4}{64} + \mathcal{O}, \tag{4.10}$$

$$J_1(a) = \frac{a}{2}\left(1 - \frac{a^2}{8} + \frac{a^4}{192} + \mathcal{O}\right), \tag{4.11}$$

then

$$Z_1 = j\rho\omega t\left[1 - \frac{2}{a}\frac{\frac{a}{2}\left(1 - \frac{a^2}{8} + \frac{a^4}{192}\right)}{1 - \frac{a^2}{4} + \frac{a^4}{64}}\right]^{-1} = j\rho\omega t\left[\frac{\left(1 - \frac{a^2}{4} + \frac{a^4}{64}\right) - \left(1 - \frac{a^2}{8} + \frac{a^4}{192}\right)}{1 - \frac{a^2}{4} + \frac{a^4}{64}}\right]^{-1}. \tag{4.12}$$

The term $\frac{a^4}{64}$ in the denominator barely has any effect on the final results, and it can be neglected. This leaves:

$$Z_1 = j\rho\omega t\left[\frac{a^2}{8}\cdot\frac{\frac{a^2}{12} + 1}{1 - \frac{a^2}{4}}\right]^{-1} = j\rho\omega t\left[\frac{\frac{a^2}{8}}{(1 - \frac{a^2}{6})}\right]^{-1}. \tag{4.13}$$

Substituting kr_0 and using Equation (4.3), we find that the approximate equation of the specific acoustic impedance for small values of x is:

$$Z_1 = \frac{4}{3} j\rho\omega t - \frac{8\rho\omega j t}{k^2 r_0^2} = \frac{4}{3} j\rho\omega t + \frac{32\eta t}{d^2} \quad \text{for} \quad \text{x} < 1. \tag{4.14}$$

For large values of x, we take Equation (4.9), as according to Jahke and Emde [232], it is very nearly true that:

$$\frac{J_1(x\sqrt{-j})}{J_0(x\sqrt{-j})} \simeq -j, \tag{4.15}$$

so

$$Z_1 = j\omega\rho t \left[1 + \frac{2j}{kr_0}\right]^{-1} \tag{4.16}$$

Expanding on the term inside the brackets, we have:

$$\left[1 + \frac{2j}{kr_0}\right]^{-1} = \frac{kr_0}{kr_0 + 2j} \cdot \frac{kr_0 - 2j}{kr_0 - 2j} = \frac{(kr_0)^2 - 2jkr_0}{(kr_0)^2 + 4} = \frac{(kr_0)^2}{(kr_0)^2 + 4} - \frac{2jkr_0}{(kr_0)^2 + 4} = \frac{1}{1 + \frac{4}{(kr_0)^2}} - \frac{2jkr_0}{(kr_0)(1 + \frac{4}{(kr_0)^2})} = \frac{1}{1 + \frac{4}{(kr_0)^2}} \cdot \left[1 - \frac{2j}{kr_0}\right]$$

If k>>1, then the term $\frac{1}{1+\frac{4}{(kr_0)^2}}$ tends to 1, so the acoustic impedance is expressed as Equation 4.17:

$$Z_1 = j\omega\rho t \left[1 - \frac{2j}{kr_0}\right] = j\omega\rho t \left[1 - \frac{4j}{d\sqrt{-\rho\omega j/\eta}}\right] \tag{4.17}$$

$$Z_1 = j\omega\rho t + 4\eta t \sqrt{\frac{\rho\omega}{2\eta}}(1 + j) \quad \text{for} \quad \text{x} > 10. \tag{4.18}$$

These formulas are used by Zwikker and Kosten [76] when discussing perforated panels and porous materials. Maa combines equations (4.14) and (4.18) to account for the values of k between 1 and 10, which is the usual design range for MPPs:

$$Z_1 = \frac{32\eta t}{d^2}(1 + \frac{x^2}{32})^{0.5} + j\rho\omega t \left[1 + (9 + \frac{x^2}{2})^{-0.5}\right] \tag{4.19}$$

4.1.1 End corrections to the Maa analytical model

According to Maa, if Equation 4.19 is compared with the exact solution of Equation 4.9, a maximum error around 6% is found, so that both the exact and approximate equations can be used for perforations in a panel if the interspace between centers is greater than the diameter of the perforation. However, the equations of Maa can be strictly applied to MPPs with circular perforations and low perforation rates, so that the perforations are separated from each other and the borders do not interact. In addition, two other factors must be considered, related to the mass reactance and the resistance of the short tube. First, the radiation of a cylindrical mass of air through the perforation produces an apparent increase in the panel

thickness. This induces an increase in the length of the tube that should be accounted for in the imaginary part of the impedance (reactance). This correction was derived by Ingard [78], resulting in a corrector factor of 0.85 jd.

In addition, the vibration of the air molecules at the surface of the panel (the thermal boundary layers) produces frictions losses when the air flow enters the perforation, producing an additional viscosity effect. The correction factor to the real part of the impedance (acoustic resistance) was derived by Ingard [173] and Maa [72] as $0.5(2_0)$.

Therefore, the approximate formula proposed by Maa including the aforementioned corrections is written as:

$$Z_1 = \frac{32\eta t}{d^2}(1+\frac{x^2}{32})^{0.5} + j\rho\omega t\left[1+(3+\frac{x^2}{2})^{-0.5}\right] + \frac{\sqrt{2}x\eta}{d} + 0.85jd\rho\omega. \tag{4.20}$$

The relative acoustic impedance of the MPP is then

$$z_{MPP} = \frac{Z_1}{\sigma\rho_0 c} = r + j\omega m \tag{4.21}$$

where σ is the perforation percentage (total area of the perforation on a unit area of the panel, interference between the pores is neglected), c is the velocity of sound, r is the relative acoustic resistance and m is the relative acoustic mass. The expressions for r and m can be derived as:

$$r = \tfrac{32\eta t}{\sigma\rho_0 c d^2}k_r, \tag{4.22}$$

$$m = \tfrac{t}{\sigma c}k_m \tag{4.23}$$

where k_r is

$$k_r = \sqrt{1+\frac{x^2}{32}} + \frac{\sqrt{2}xd}{32t}, \tag{4.24}$$

and k_m is

$$k_m = 1 + (9+\frac{x^2}{2})^{-0.5} + 0.85\frac{d}{t}.. \tag{4.25}$$

From Equation (4.8) Maa obtains a very useful design formula:

$$x = d\sqrt{\frac{f}{10}}, \tag{4.26}$$

where d is the hole diameter in mm and f is the frequency in Hz. The ratio d/t is usually close to 1 and is taken as such. The perforation ratio can be found from Equation (4.22):

$$\frac{\sigma}{t} = \frac{32\eta k_r}{\rho c d^2 r}. \tag{4.27}$$

If the holes in the Mpp are distributed in square lattices, the exact value of σ is:

$$\sigma = (\frac{\pi}{4})(\frac{d}{b})^2, \tag{4.28}$$

where d is the hole diameter and b is the separation of the holes.

Substituting the perforation ratio into Equation (4.23) yields the mass reactance formula:

$$x_m = (\frac{k_m}{8k_r})rx^2. \tag{4.29}$$

In the range of x from 0.5 to 2 (the most important in MPP design), the value of the ratio k_m/k_r is approximately 2, so in this region, Equation (4.29) can be taken as:

$$x_m = 0.25rx^2. \tag{4.30}$$

4.1.2 The microperforated panel absorber

The MPP absorber is conformed by an MPP fixed before a solid surface with a cavity of thickness D. The specific and relative acoustic impedance of the cavity are:

$$Z_D = -j\rho c \cdot \cot(\frac{\omega D}{c}),\ z_D = -j\cot(\frac{\omega D}{c}) \tag{4.31}$$

which is added to the acoustic impedance of the MPP

$$z_1 = z_{MPP} + z_D = r + j\omega m - j\cot(\frac{\omega D}{c}). \tag{4.32}$$

The formula for the absorption coefficient is:

$$\alpha = 1 + |R|^2, \tag{4.33}$$

where

$$R = \frac{Z_1 - Z_0}{Z_1 + Z_0} = \frac{z_1 - 1}{z_1 + 1}, \quad \text{where } \ Z_0 = \rho c. \tag{4.34}$$

Then for normal incidence, the absorption coefficient will be:

$$\alpha = 1 - \left|\frac{z_1 - 1}{z_1 + 1}\right|^2 = 1 - \frac{[Re(z_1 - 1)]^2 + [Im(z)]^2}{[Re(z_1 + 1)]^2 + [Im(z)]^2}$$

$$\alpha = \frac{(r+1)^2 - (r-1)^2}{(r+1)^2 + (\omega m - \cot(\frac{\omega D}{c}))^2} = \frac{4r}{(r+1)^2 + (\omega m - \cot(\frac{\omega D}{c}))^2}. \tag{4.35}$$

In case of oblique incidence θ, the acoustic impedance of the MPP does not change because it is local, but the cavity behind the panel will change, as the wave paths will have a difference of $2D\cos\theta$. The relative acoustic impedance and absorption coefficient for oblique incidence will then be:

$$z_1 = (r + j\omega m)\cos\theta - j\cot(\frac{\omega D\cos\theta}{c}), \tag{4.36}$$

$$\alpha = \frac{4r\cos\theta}{(1 + r\cos\theta)^2 + (\omega m\cos\theta - \cot(\frac{\omega D}{c})\cos\theta)^2}. \tag{4.37}$$

Absorption bandwith

The maximum value of the absorption coefficient with normal incidence will be when

$$\alpha_0 = \frac{4r}{(1+r)^2}, \tag{4.38}$$

which occurs at the resonance frequency (f_0, ω_0) when

$$\omega_0 m = \cot(\frac{\omega_0 D}{c}) \rightarrow \operatorname{acot}(\omega_0 m) = \frac{2\pi D}{\lambda_0}. \tag{4.39}$$

This gives the cavity depth ratio

$$y = \frac{D}{\lambda} = \frac{1}{2\pi}\operatorname{acot}(\omega_0 m), \tag{4.40}$$

where λ is the wavelength of the resonance frequency. With these equations, given the values of k,r and f_0, the structure of the MPP absorber is determined. An important design quantity is the ratio of ωm to $\omega_0 D/c$, which is the ratio of the mass and cavity reactances at low frequency:

$$g = \frac{mc}{D} = \frac{\omega_0 m}{\operatorname{acot}(\omega_0 m)}, \tag{4.41}$$

this parameter is a constant of the MPP, not dependent of the frequency.

The absorption coefficient is one half of the maximum value at the frequencies given by:

$$\alpha = \frac{4r}{2(1+r)^2} \rightarrow \omega m - \cot(\frac{\omega D}{c}) = \pm(1+r), \tag{4.42}$$

which can also be rewritten as

$$2\pi g y_1 - \cot(2\pi y_1) = +(1+r), \tag{4.43}$$
$$2\pi g y_2 - \cot(2\pi y_2) = -(1+r), \tag{4.44}$$

where y_1 and y_2 depend on f_1 and f_2, which are the half absorption frequencies and conform the frequency band of absorption $(f_1 - f_2)$

$$y_1 = \tfrac{f_1 D}{c} = \tfrac{D}{\lambda_1}, \tag{4.45}$$
$$y_2 = \tfrac{f_2 D}{c} = \tfrac{D}{\lambda_2}. \tag{4.46}$$

These equations, along with Equation (4.39) rewritten with g and y as variables

$$2\pi g y_0 - \cot(2\pi y_0) = 0, \tag{4.47}$$

can be solved graphically, according to Maa. For large values of g (when $g \geq 2(1+r)/3$), the cotangents can be taken (approximately and without introducing errors) as:

$$\cot(2\pi y) = \frac{1}{2\pi y} - \frac{2\pi y}{3} \tag{4.48}$$

Substituting Equation (4.48) into Equations (4.43), (4.44) and (4.47), we get:

$$y_0 = \tfrac{1}{2\pi} \cdot \frac{1}{\sqrt{g+1/3}}, \tag{4.49}$$

$$y_1 = \tfrac{1}{2\pi} \cdot \sqrt{\left(\tfrac{1+r}{2g+\frac{2}{3}}\right)^2 - \frac{1}{g+\frac{1}{3}}} - \frac{1+r}{2g+\frac{2}{3}}, \tag{4.50}$$

$$y_2 = \tfrac{1}{2\pi} \cdot \sqrt{\left(\tfrac{1+r}{2g+\frac{2}{3}}\right)^2 + \frac{1}{g+\frac{1}{3}}} - \frac{1+r}{2g+\frac{2}{3}}. \tag{4.51}$$

From these we get the frequency ratio and resonance frequency for large values of g:

$$B = \frac{y_2}{y_1} = \frac{f_2}{f_1}. \tag{4.52}$$

$$f_0 = \sqrt{f_1 \cdot f_2} \tag{4.53}$$

Equation (4.42) can also be converted into:

$$\frac{\omega D}{c} = \operatorname{acot}\left[\pm(1+r) + g\frac{\omega D}{c}\right]. \tag{4.54}$$

An exact solution for this equation does not exist, but Maa arrives to an approximate solution (less than 1% error) using the derivative of the arc-cotangent for when the values of g are smaller than 1.

$$\tfrac{\omega_1 D}{c} = \operatorname{acot}(1+r) \cdot \left[1 + \tfrac{g}{1+(1+r)^2}\right]^{-1}, \tag{4.55}$$

$$\tfrac{\omega_2 D}{c} = (\pi - \operatorname{acot}(1+r)) \cdot \left[1 + \tfrac{g}{1+(1+r)^2}\right]^{-1}. \tag{4.56}$$

With Equations (4.55) and (4.56), we can calculate the frequency ratio:

$$B = \frac{\omega_1 D/c}{\omega_2 D/c} = \frac{f_2}{f_1} = \frac{\pi}{\operatorname{acot}(1+r)} - 1, \tag{4.57}$$

which shows that for small values of g, the frequency interval is constant and only depends on r.

As stated earlier, with the values of r, x and f_0 defined, we can determine the structure and frequency characteristics of MPP. The resonance frequency can be found from the ratio of the resonance frequency to the lower half-absorption frequency:

$$FR = \frac{f_0}{f_1} = \left(1 + r + \frac{g+1/3}{1+r}\right) \operatorname{acot}(\omega_0 m), \tag{4.58}$$

in which $\omega_0 m$ is given by Equation (4.29) if $g + 1/3$ is small compared to $(1+r)^2$, so it will also depend on r and x.

Equations (4.52) and (4.57) show the frequency interval as a function of the perforation constant x and the relative acoustic resistance r, but do not account for all values of the frequency interval, as the regions where g is smaller than 1 and where $g \geq 2(1+r)/3$ do not intersect, so the relationship between these parameters in that area will have to be found graphically. By plotting the relationship, we can obtain the values of r and x for the desired absorption band.

4.1.3 Overperforation effects: the equivalent fluid model

Years after Maa developed his model, the equivalent fluid model was adapted to MPPs using the Johnson-Allard approach with an equivalent tortuosity [74, 75]. The two models are similar, using the same parameters and yielding similar absorption curves.

Maa used an approximation for the impedance of an array of circular perforations in Equation 4.9. The edge impedance proposed by Ingard [78] assumes that perforations are far enough from each other so that there is no interaction between them. However, if the perforation ratio is high enough, that interaction has to be accounted for. This effect is introduced by Melling [233] by dividing the mass reactance by the Fok function [234]:

$$F(\epsilon) = \left(1 - 1.4092\epsilon + 0.33818\epsilon^3 + 0.06793\epsilon^5 - 0.02287\epsilon^6 + 0.03015\epsilon^7 - 0.01641\epsilon^8\right)^{-1}, \tag{4.59}$$

where

$$\epsilon = \sqrt{\phi}. \tag{4.60}$$

Combining this equation with the input impedance of a single MPP according to Maa is

$$Z_1 = \frac{4x\mu\sqrt{3}}{\phi \cdot d} + i\frac{\omega\rho_0}{\phi}\left(0.85\frac{d}{F(\epsilon)} + t\left[1 - \frac{2}{x\sqrt{-j}}\frac{J_1(x\sqrt{-j})}{J_0(x\sqrt{-j})}\right]^{-1}\right) - Z_0\cot(kD) \tag{4.61}$$

The acoustic impedance in the equivalent fluid model is

$$Z_{hole} = i\omega\rho_e\frac{t}{\phi} \tag{4.62}$$

where ρ_e is the effective density related to the air density and the dynamic tortuosity α ($\rho_e = \rho \cdot \alpha$)

$$\rho_e = \rho\left(1 + \frac{\sigma p G_j(\omega)}{i\omega\rho_0}\right) \tag{4.63}$$

$$G_j(\omega) = \left(1 + \frac{4\omega\rho_0\mu}{\sigma^2\phi^2 r^2}\right)^{1/2} \tag{4.64}$$

where the parameters σ , and r (radius) are dependent on the design parameters and unique to each panel:

$$\sigma = \frac{8\mu}{\phi r^2}, \tag{4.65}$$

Atalla and Sgard introduced the edge impedance through the geometrical tortuosity α_∞, which is defined as the high-frequency limit of the tortuosity $\alpha_e = \frac{\rho_e}{\rho_o}$. The geometrical tortuosity of the MPP also depends on the media in contact with the panel, so for a panel in contact with air on both sides:

$$\alpha_{\infty,} = 1 + \frac{0.85d}{tF\left(\epsilon\right)}. \tag{4.66}$$

Therefore, the impedance of a single MPP with the equivalent fluid model is:

$$Z_{MPP} = i\frac{\omega\rho_0\alpha_\infty t}{\phi}\left[1 + \frac{\sigma\phi}{i\rho_0\omega\alpha_\infty}\left(1 + i\frac{4\omega\rho_0\alpha_\infty^2\mu}{\sigma^2\phi^2 r^2}\right)^{1/2}\right] \tag{4.67}$$

4.1.4 The double layer MPP

It is not unusual to use multiple MPPs in the same system, which may be connected in series or in parallel. A parallel connection would widen the bandwidth but would decrease the maximum absorption, while a series connection would have a wider frequency band and higher absorption.

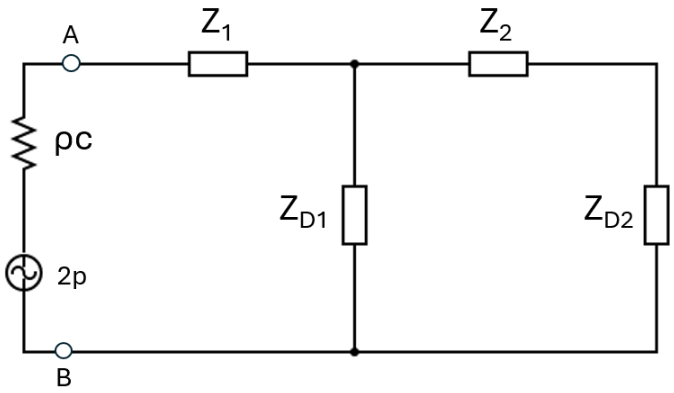

Figure 4.1: Double Panel equivalent circuit

Maa obtained the impedance of a double layer MPP using the equivalent circuit analogy, where the air cavities and the perforated panels are related to an electrical circuit (Figure 4.1) in series and parallel configurations. The impedance of the panel will always be in series while the impedance of the air cavity will be in parallel, as shows Figure 4.1). Then, we can obtain the impedance equation that takes into account both panels by using the Thevenin theorem, assuming an open circuit between points A and B, and taking the first MPP as the lad resistance.

The first air gap resistance Z_{D1} is in parallel with Z_2, which is:

$$Z_2 = Z_{MPP2} + Z_{D2} = r_2 + j\omega m_2 - j\cot\frac{\omega D_2}{c} \tag{4.68}$$

so

$$Z = Z_{MPP1} + \frac{Z_{D1} \cdot (Z_{MPP2} + Z_{D2})}{Z_{MPP2} + Z_{D2} + Z_{D1}} \tag{4.69}$$

As the Thevenin equivalent is not the best method to obtain the acoustic impedance in systems with multiple microperforated panels, and it could be more convenient to use the Transfer Impedance method. Following the method established by Pedro Cobo [90] in his research, we can establish that the impedances are:

$$Z_{C3} = -i \cdot Z_0 \cdot \cot(kD_3), \tag{4.70}$$

$$Z_3 = Z_{MPP3} + Z_{C3} \tag{4.71}$$

$$Z_{C2} = Z_0 \cdot \frac{Z3 \cdot \cos(kD_2) + i \cdot Z_0 \cdot \sin(kD_2)}{Z_0 \cdot \cos(kD_2) + i \cdot Z_3 \cdot \sin(kD_2}, \tag{4.72}$$

$$Z_2 = Z_{MPP2} + Z_{C2}, \tag{4.73}$$

$$Z_{C1} = Z_0 \cdot \frac{Z2 \cdot \cos(kD_1) + i \cdot Z_0 \cdot \sin(kD_1)}{Z0 \cdot \cos(kD_2) + i \cdot Z_2 \cdot \sin(kD_1}, \tag{4.74}$$

and

$$Z_1 = Z_{MPP1} + Z_{C1}. \tag{4.75}$$

Introducing this last equation into Equation 4.34 would provide the normal incidence reflection and absorption coefficients of the multiple layer MPP.

4.2 Analytical solutions of the Maa equation

With the equations Maa obtained, the perforation constant vs. the frequency interval graph appears as shown in Figure 4.2, where it can be seen that it is missing a section, as there is no mathematical solution for those values. Maa obtains the values for the frequency ratio in two different instances, depending on the value of g, making it a piecewise function. The best way to obtain this interval is through Curve Fitting. Matlab contains a curve fitting tool, which allows you to choose the equation used for the fitting (interpolant, polynomial, smoothing spline, exponential, etc.) and the parameters of said equation (terms, degree, method, etc.).

In this case, Smoothing Spline was chosen with a smoothing parameter of very nearly 1. The tool will then generate a function that can be added to the code. It was only necessary to generate the code for one r value, as it could be applied to all r values without an issue. The results of the curve fitting performed by Matlab are shown in Figure 4.3.

To obtain the closest values for the desired frequency ratio, we use the Matlab function *get* to take the all the values in the curve fitting graph and store it. It has to be done inside the loop to store the values for each curve.

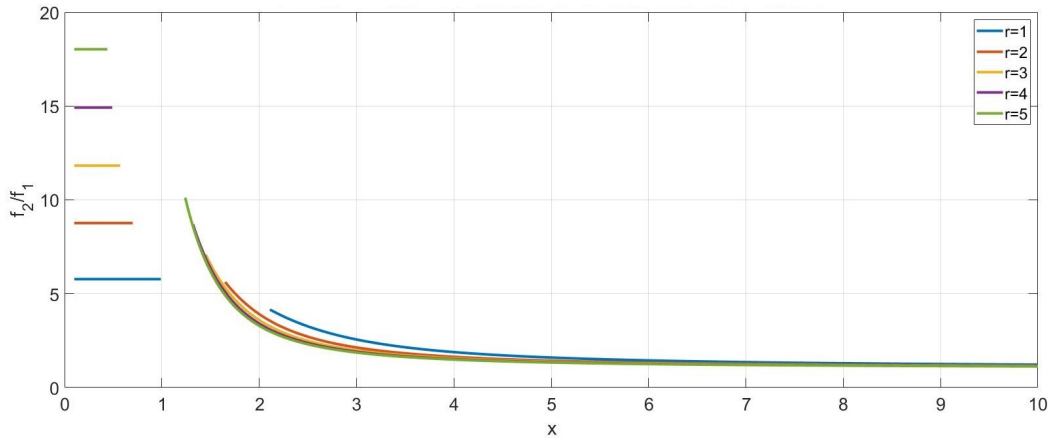

Figure 4.2: Frequency ratio as a function of x and r from Maa's equations, missing an interval in the curve

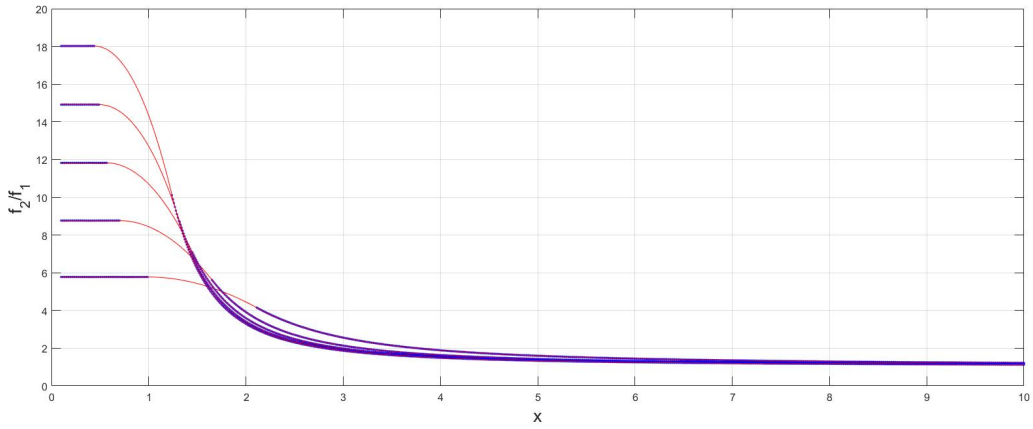

Figure 4.3: Frequency ratio as a function of x and r after curve fitting.

We then use the desired frequency ratio and obtain the row position in each of the columns of the *y1* matrix for which the difference is minimum. As the function gives back both the row position (I) and the difference (A), we use the row position to get the corresponding *x/k* and frequency interval values to create a matrix (*options*) that shows all the available combinations of r and *x/k*, with the corresponding frequency ratio value and error to the desired frequency ratio value. As some of the r curves won't always cross the desired frequency ratio, the difference value will be big, so a for loop is added to introduce a tolerance in the difference values, removing the rows that do not meet the tolerance values.

Comparison

To check if the code was correct, a test case was run with the same conditions as those in Maa's article [72]. In his example, the desired absorption band was 250-2000 HZ, which required a frequency interval of 8.

An important clarification: Maa first used x for the perforation constant, but then changed it

to k in another article to avoid confusion, and the graphs are taken from that article. As k was already being used for another parameter in this research, it was decided to use x.

Figures 4.4 and 4.5 show the perforation constant as it varies with the frequency interval. Figure 4.4 was taken from Maa's paper to compare to the graph obtained from the code developed. Given that Maa uses a specific scale, it is impossible to be 100% certain that the results obtained are the same, but they seem to be very similar.

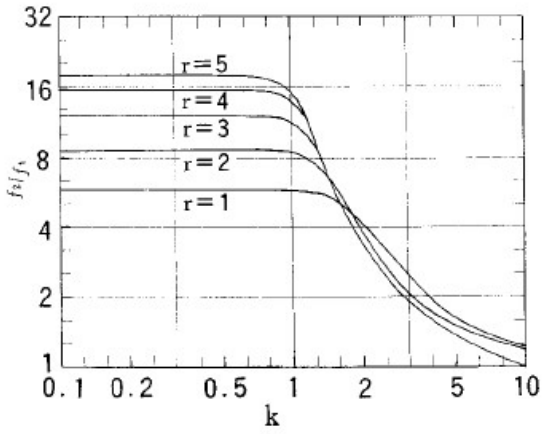

Figure 4.4: Frequency ratio as a function of the perforation constant and r from Maa [26]

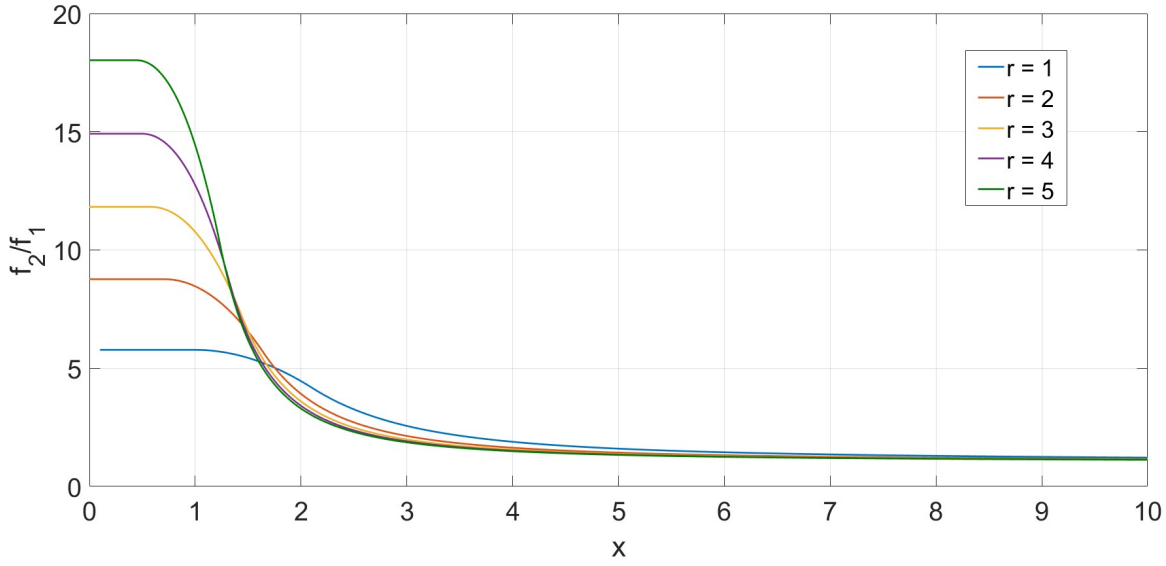

Figure 4.5: Frequency ratio as a function of the perforation constant and r from the code

Figures 4.6 and 4.7 are meant to be comparisons between the relationship of the constants obtained by Maa and through Matlab.

Figure 4.8 is interesting to plot to see how the maximum absorption coefficient varies with the acoustic resistance. As can be seen in the figure, the maximum absorption coefficient

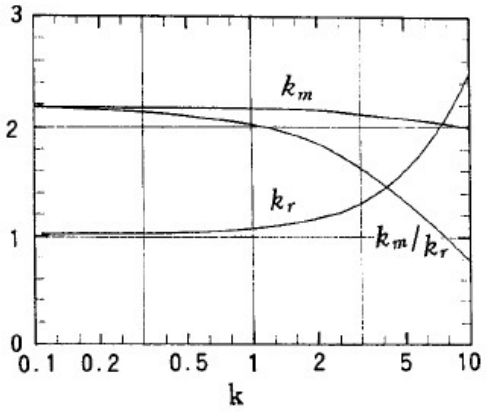

(a) Constants of the MPP as functions of the perforation constant from Maa [26].

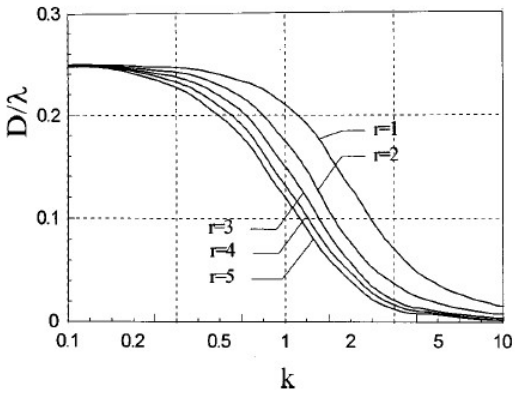

(b) Relative cavity depth as a function of the perforation constant and r from Maa [26].

Figure 4.6: Relationship between constants calculated by Maa.

value is obtained when r is 1, but it approximately stays over 0.9 in the range 0.5-2. A high absorption coefficient is always desirable, so it should be taken into account when choosing the r value.

Table 4.1 shows the results obtained by Maa and those obtained through Matlab. It is unknown which values for density, viscosity, and speed of sound were used for his calculations, so the conditions were estimated using his results. Air was taken to be at room temperature. Another detail to be taken into account is that Maa doesn't explicitly state which value of r was chosen, only mentioned that it was slightly over 2. Using Matlab, another frequency ratio graph (Figure 4.5) was plotted, but with more r values. With this graph, it was found that the curve for r=2.2 gave a frequency ratio of 8 at approximately x=1.25, which is the value that Maa used.

Table 4.1: Results comparison between Maa and the code.

	Maa	Matlab
f_2/f_1	8	8
r	2<	2.2
x	1.25	1.25
FR	3.05	3.106
α_{max}	0.88	0.8594
f_0	760 Hz	776.53 Hz
d = t	0.144 mm	0.1419 mm
σ	0.52%	0.4978%
b	1.77 mm	1.7818 mm
D	0.064 m	0.0606 m

The difference in results varies between 0.6% and 5.3%, which can be due to the uncertainty in what value of perforation constant Maa used and the assumption that $\omega_0 m$ is always given

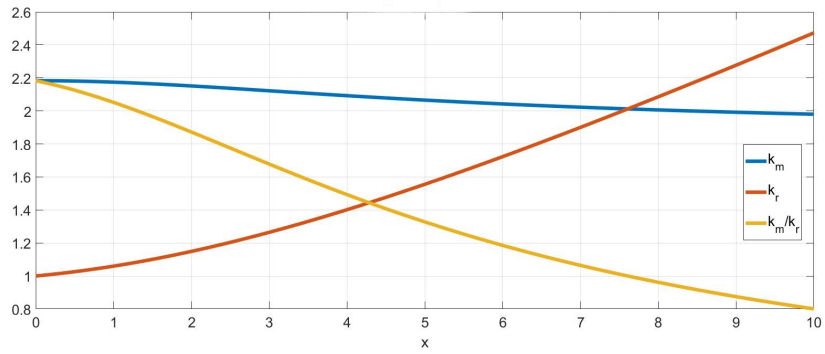

(a) Constants of the MPP as functions of the perforation constant

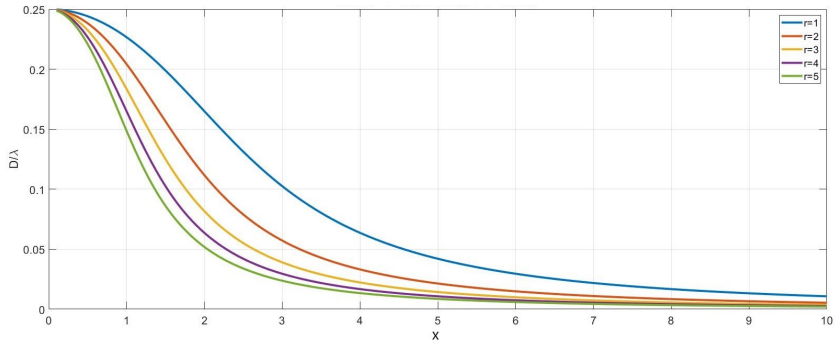

(b) Relative cavity depth as a function of the perforation constant and r

Figure 4.7: Relationship between constants calculated in Matlab

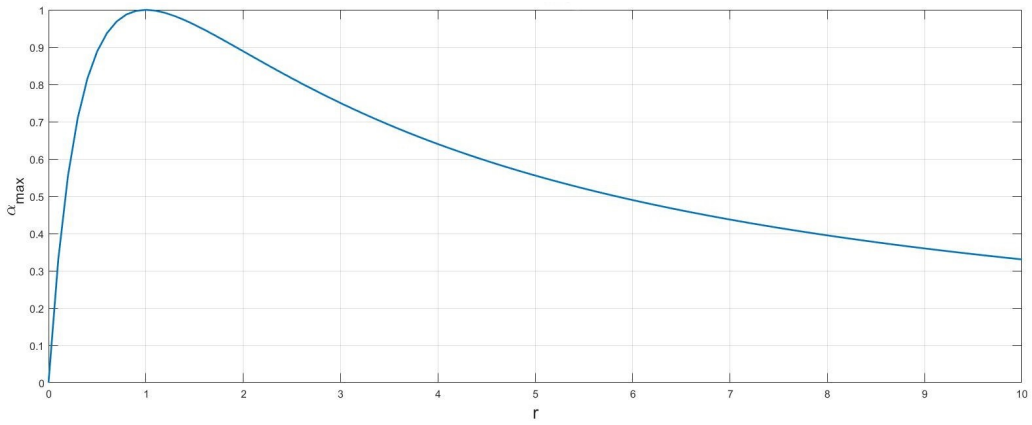

Figure 4.8: Variation of α_{max} with r

by Equation 4.29, but this only occurs when $g + 1/3$ is smaller than $(1 + r)^2$ (which it is in this case, 1.33<10.24).

To get a resonance frequency closer to 760 Hz, we would need to use an r value of approximately 1.8, but Maa clearly states that he uses a value slightly over 2. Using this r value, we get closer values in some cases (in frequency ratio and hole diameter) but a bigger error in others (cavity depth, perforation area ratio, separation of perforations, and maximum absorption

coefficient).

The absorption coefficient varying with the frequency and incidence angle is shown in the following graphs. The peak absorption bandwidth decreases as we move beyond the frequency interval into higher frequencies. The results in Figure 4.9 show that the absorption peak increases and moves to higher frequencies as the incidence angle increases, as Maa states.

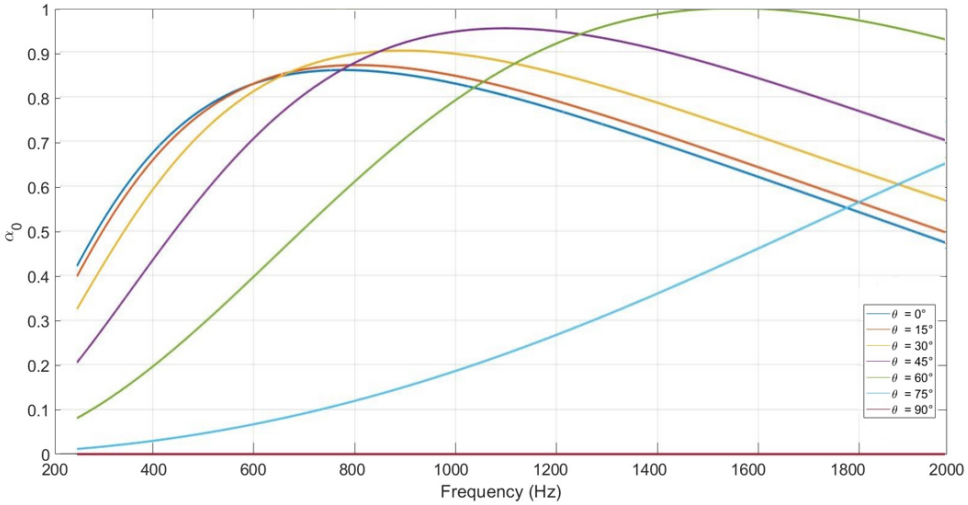

Figure 4.9: Absorption coefficient variance depending on the incidence angle.

Finding optimized solutions

The Matlab in-built simulated annealing optimization function requires a function to minimize in order to find the best possible solution. The function allows us to set a lower and upper limit to the design parameters that it has to find. Initially, the function was built to minimize the $|R|^2$ value, so the absorption coefficient would be as high as possible. This method had a significant issue, as the program could only be able to optimize for a single value in the frequency range. Therefore, changes were made inside the code, so the function would minimize the sum total average of all the $|R|^2$ in a range of frequencies. The main objective with this was to find the absorption coefficient curve most constant. Due to the random factor in the simulated annealing method, some of the solutions obtained were not ideal, with several maximum and minimum peaks.

To ignore those solutions, an iterative process was implemented in the code. This way, the method would continue to run the simulated annealing optimization function for a determinate number of times until the results would fulfill the conditions established. If the program reached the end of the iterative process without finding a solution, it would show the last solution calculated. Several conditions were attempted, starting with low and easy to achieve values, and gradually increasing the constraints as to find the limits of the panels with the boundary conditions that have already been given to the design parameters.

The boundary conditions for the design parameters are: perforation diameter [0.5, 1.5] mm, panel thickness [0.254, 5] mm, cavity distance [1, 8] cm, and perforation area [1, 18] %. While deciding the boundary conditions for the perforation diameter, the error of the 3D printer

had to be taken into account. After printing some test panel, it was discovered that the perforation diameter coming out was much smaller than the one specified in the CAD model. The smallest hole the printer can do is around 0.5-0.6 mm in diameter, so a 0.9 mm diameter is required in the cad model. Due to this, it is necessary to handle the uncertainty in the future acoustic tests and try to correlate the data as best as possible to calculate the error so it can be included in the code and the design.

Regarding the constraints for the iterative process, two types were uses depending on what was to search for. The first condition would only allow for a solution that had an absorption coefficient value above a threshold for the entirety of a wide range of frequencies. The other condition would also look for a high average absorption value.

The parameters obtained sometimes gave unrealistic values. While FDM printers can have high precision, some values are unattainable at the moment, mostly due to the nature of FDM and the layer height. In the available printer (STRATASYS Fortus 450mc), the smaller diameter made that was visible was of 0.8 mm and there were some issues with the printing. For this reason, some of the solutions obtained were adapted to more realistic values. A comparison between the "raw" configuration versus the "adapted" one is shown in Figure 4.10.

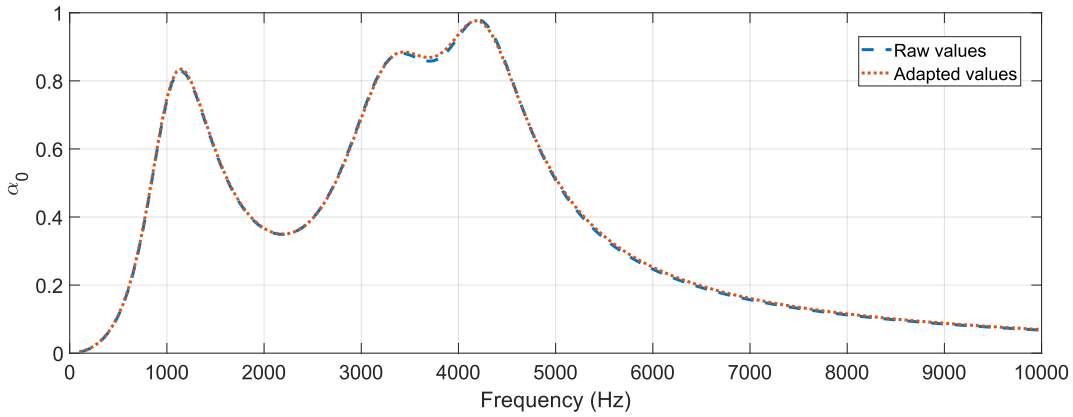

Figure 4.10: Comparison between the raw parameters obtained and the adapted values for manufacturing.

One common observation across all computed solutions where the lower limit for the diameter was set at 0.6 mm is a noticeable drop in the absorption coefficient between 1000 and 2000 Hz. The optimization algorithm consistently aimed to improve the absorption in the range of 3000 to 5000 Hz, but when the target frequency range was expanded, the resulting curve exhibited multiple peaks. Despite this, the code still provides satisfactory solutions within the specified range, although it may not be entirely adequate for the intended application of the panels.

With a better understanding of the printer's capabilities and the diameters it can achieve, it may be possible to reduce the lower limit for the diameter to around 0.5 to 0.55 mm. While this may not produce an absorption coefficient above 0.5 in the 1000–5000 Hz range, the resulting values could be close enough to justify the use of these panels for practical purposes. An alternative approach to achieve smaller diameters would be to use laser cutting, as the laser beam typically has a diameter of around 0.15 mm, allowing for more precise perforations.

In addition to the lower diameter limit, the current printer is encountering issues when printing panels with a high perforation density (e.g., over 100 holes), often leaving unfilled gaps within the panel. This affects the overall perforation area and may compromise the performance of the panels.

4.2.1 Panel design parameter iterations

In order to better adapt the parameters to more realistic values while not compromising the original absorption efficiency, it was necessary study and analyze how each parameter affect the absorption coefficient, over a thousand iterations were run for each case, varying one parameter while maintaining the others fixed, trying to find the best possible solution in each case. Using a three panel configuration for this analysis, Table 4.2 shows the fixed parameter used in each case, as well as variation (upper and lower limit) of the analysis. As a reference point, Figure 4.11 shows the absorption coefficient with the fixed parameters.

Table 4.2: Fixed parameters.

Parameter	**MPP1**	**MPP2**	**MPP3**	**Variation**
Panel Thickness (t)	1.2 mm	2.67 mm	4.47 mm	± 0.15 mm
Cavity Depth (D)	1.14 cm	1 cm	0.97 cm	± 0.15 mm
Cavity Diameter (d)	0.5 mm	0.5 mm	0.5mm	± 0.20 mm
Perforation Area (ϕ)	10%	10%	6%	±3%

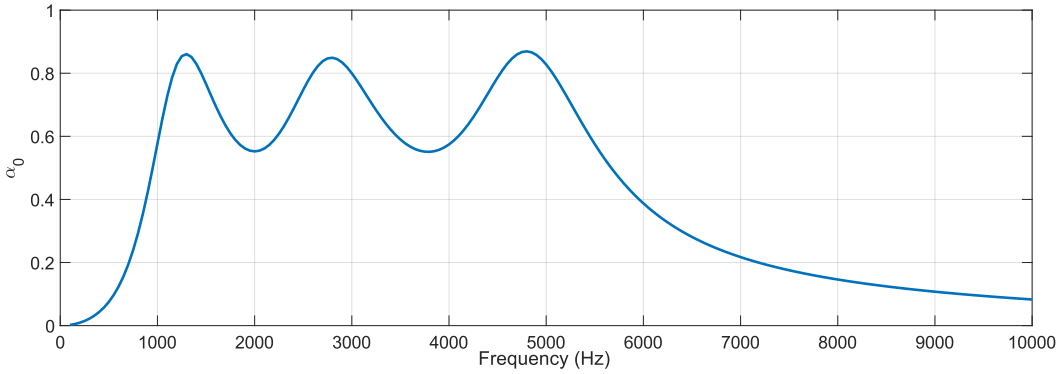

Figure 4.11: Absorption coefficient of the fixed parameters.

Figures 4.12 to 4.16 present the results obtained from the analysis. The cavity diameter impacts two distinct parameters: the perforation area and the number of holes. To explore these effects, two separate cases were considered. In one case, the cavity diameter is varied while keeping the number of perforations constant, while in the other case, the perforation area is held constant. For each iteration, the remaining parameter is recalculated accordingly to reflect the changes in the system.

From the figures, it is evident that the parameter most significantly influencing the absorption coefficient, with only minor variations, is the cavity diameter, as demonstrated in Figures 4.15 and 4.16. Changes in cavity diameter cause a dramatic alteration in the original absorption

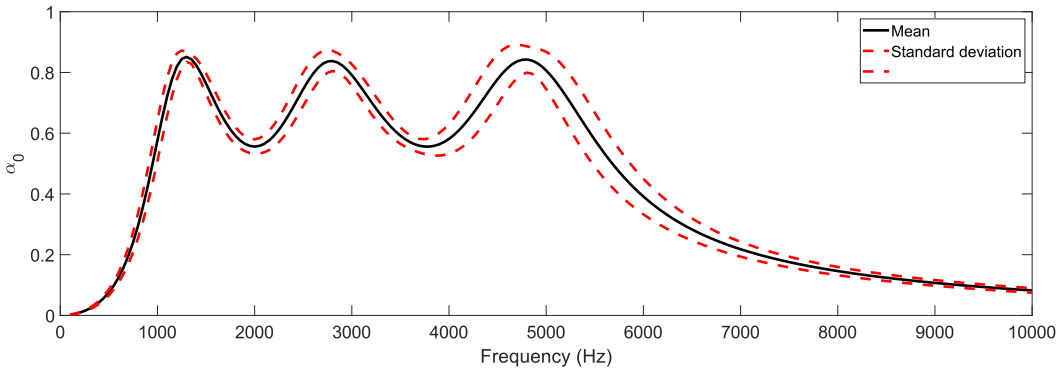

Figure 4.12: Absorption coefficient of different panels, varying the cavity depth ±0.15 mm.

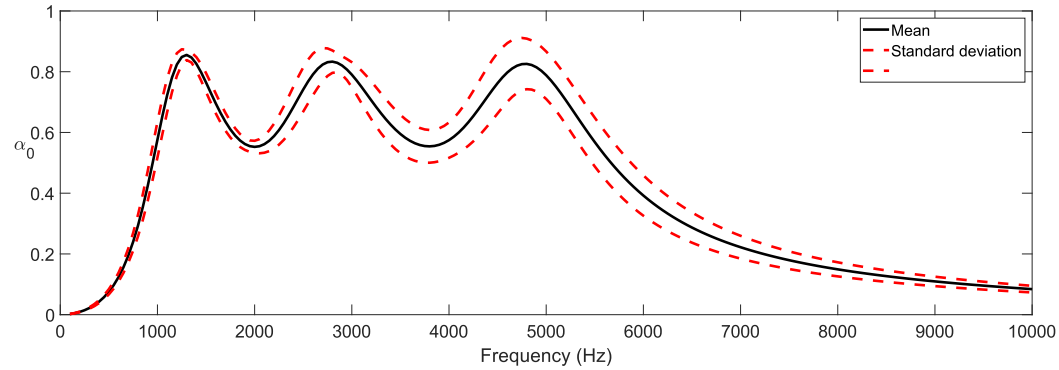

Figure 4.13: Absorption coefficient of different panels, varying the thickness (t) ±0.5 mm.

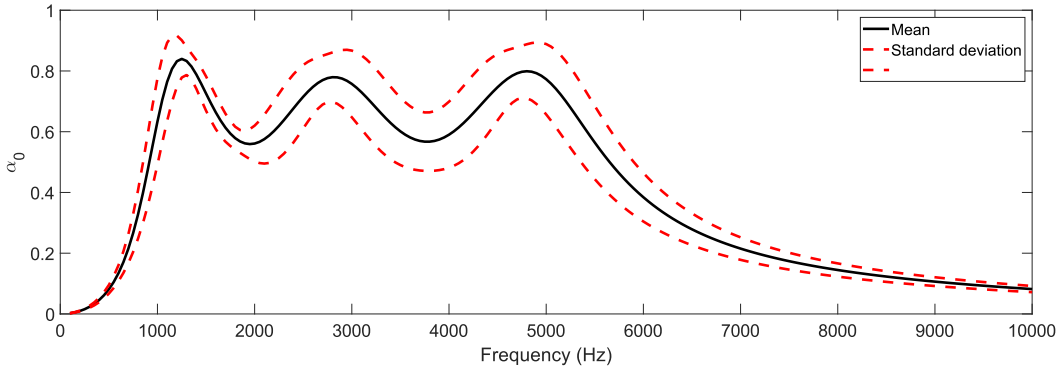

Figure 4.14: Absorption efficiency of different panels, varying the perforation area (ϕ) ±3%.

coefficient curve (Figure 4.11). In contrast, adjustments to cavity depth, panel thickness, and perforation area percentage result in curves that closely resemble the original, with only slight differences in the three primary peaks. Specifically, the first absorption peak remains nearly identical across all iterations when modifying panel thickness (Figure 4.13) or cavity depth (Figure 4.12). Varying the perforation area, whether independently (Figure 4.14) or in combination with the cavity diameter (Figure 4.15), introduces the most variability in the absorption coefficient curves across the different iterations. The three absorption peaks see

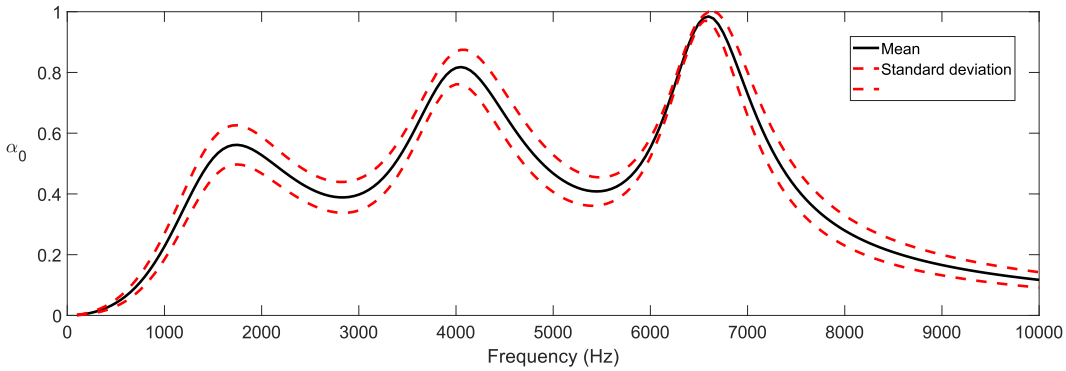

Figure 4.15: Absorption coefficient of different panels, varying the cavity diameter ±0.2 mm and maintaining the perforation area constant

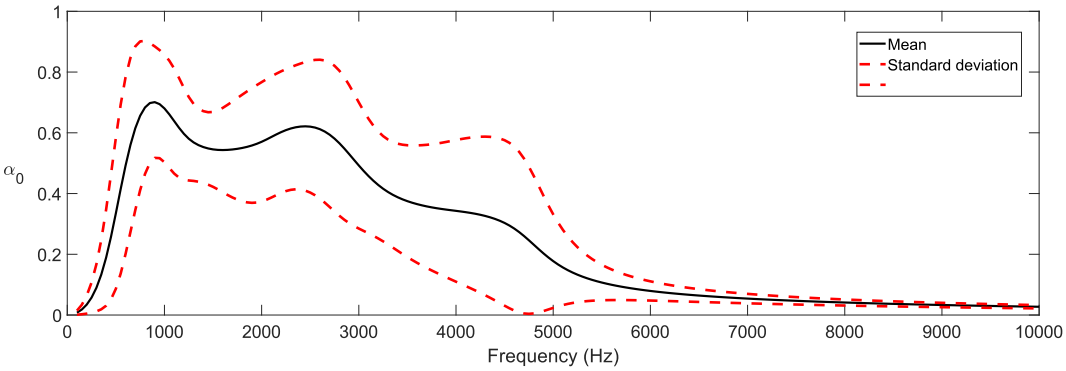

Figure 4.16: Absorption coefficient of different panels, varying the cavity diameter ±0.2 mm and maintaining the number of holes constant

the most variation of placement in these last two figures, while the variation of the perforation area moves up the peak in the frequency range; varying it along with the hole diameter moves it down.

4.3 Acoustic tests

4.3.1 Methodology

With the purpose of comparing the precision and efficiency of FDM printing of microperforated panels, several test cases were prepared. Up to 10 different single panel configurations were chosen, mainly changing the perforation diameter. For comparison, the panels were also fabricated in methacrylate (M), with laser cut perforations. In total, 17 tests (see Table 4.3) will be carried out with a single microperforated panel. The materials themselves do not influence the acoustic behavior of the panels, but the manufacturing method can, as it can affect the porosity of the panel or the quality of the perforations. The main objective is to compare the results obtained with the theoretical results, to check the vialability of 3D printed microperforations.

All panels have a diameter of 34 mm and, as for the perforation area parameter, it is an approximation, as the author made sure it would end up determining an integer as the total number of holes.

Table 4.3: Nominal design parameters of the test cases.

	d (mm)	**t (mm)**	**D (mm)**	**%**	**Material**
Case 1	0,4	0,5	1	3	M
Case 2	0,6	1	14	2,5	M
Case 3	0,6	2	7	5	M
Case 4	0,8	3	2.6	2,5	M/ULTEM
Case 5	1	5	9.2	6	M/ULTEM
Case 6	1,2	8	2.6	7	M/ULTEM
Case 7	1,2	2	3.6	6	M/ULTEM
Case 8	1,2	3	3.6	6	M/ULTEM
Case 9	1	2	3.6	6	M/ULTEM
Case 10	1	3	3.6	6	M/ULTEM
Case 11	0.9	4	5.2	4	M/ULTEM
Case 12	1.1	6	9.2	5	M/ULTEM

Two additional configurations were tested to compare to the theoretical results: one with 2 microperforated panels (Table 4.4) and another one with 3 panels (Table 4.5), made in both ULTEM™ 9085 and methacrylate. In both trials, we plan to print cylindrical support pieces in ABS of length D to facilitate assembly.

Table 4.4: Nominal design parameters of the two panel configuration

	d (mm)	**t (mm)**	**D (mm)**	**%**
Panel 1	1	2	10.5	4
Panel 2	1	2	13.9	6

Table 4.5: Nominal design parameters of the three panel configuration

	d (mm)	**t (mm)**	**D (mm)**	**%**
Panel 1	1	1	15	8,4
Panel 2	1	3	7	7,5
Panel 3	1	8	2	4

The tests were performed at the Leonardo Torres Quevedo Institute of Physical and Information Technologies, which is part of CSIC (*Consejo Superior de Investigaciones Científicas*), with the help of Francisco Simón Hidalgo and Álvaro Espinoza, part of the investigation group of Environmental Acoustics (GAA).

To evaluate the sound absorption performance of the test samples, the impedance tube method was employed. This widely recognized and reliable technique is commonly used to assess the sound absorption properties of materials, enabling the identification of frequency-dependent

absorption characteristics [235]. It adheres to established standards, such as ISO 10534-2 [236] and ASTM E 1050-19 [237]. In this method, the sample is positioned at one end of a straight, smooth, and airtight circular tube. A sound generator or loudspeaker is placed at the opposite end to produce sound waves. To prevent sound reflections from the source end, an absorbing termination is installed behind the sample [238].

Two primary measurement techniques are available for the impedance tube method: the standing wave method and the transfer function method [239]. Among these, the transfer function method is more commonly utilized today and was the chosen approach for the current tests. The reason that it is more used is that it is less sensitive to the positioning of microphones and provides more consistent results across a broader frequency range. In this setup, the software produces sound waves that are then amplified and strike the sample's surface; a portion of the sound energy is absorbed by the material, while the remainder is reflected, generating reflected waves. To capture the necessary data, two microphones are mounted along the tube. These microphones measure the sound pressure and frequency of the reflected waves, which are then analyzed to determine the impedance ratio and the sound absorption coefficient [240]. The transfer function between the two microphone signals is

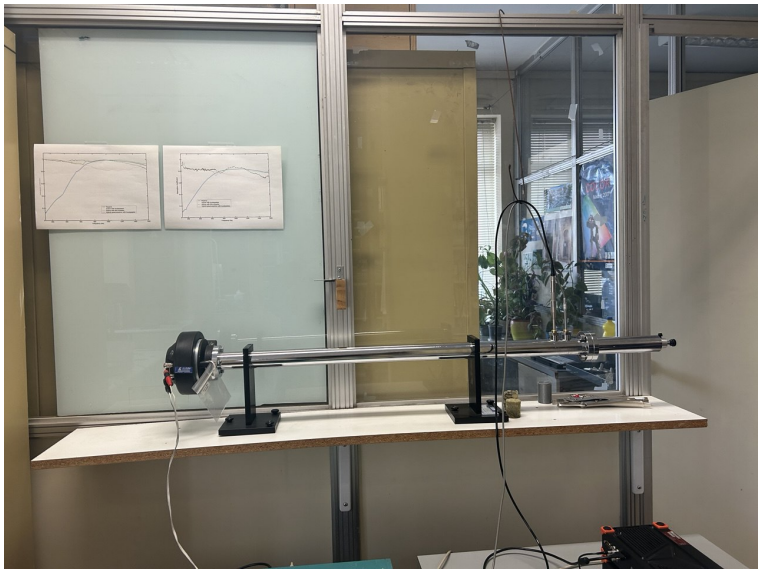

Figure 4.17: Impedance Tube used for the tests.

$$H_{21} = \frac{p_2}{p_1} = \frac{p_i e^{jkx_1} + p_r e^{-jkx_1}}{p_i e^{jkx_2} + p_r e^{-jkx_2}}. \tag{4.76}$$

The pressure reflection for normal incidence is:

$$r = \frac{H_{21} - e^{-jk(x_1 - x_2)}}{e^{jk(x_1 - x_2)} - H_{21}} \tag{4.77}$$

which is then plugged into the following equation to obtain the absorption coefficient values in the frequency range.

$$\alpha = 1 + |r|^2. \tag{4.78}$$

In microperforated panels, the absorption is mostly governed by the interaction of the sound waves with the small holes, which cause a local resonant effect, leading to a higher absorption at specific frequencies. The absorption happens because the perforations allow for sound waves to pass through and interact with the air behind the panel, causing the sound waves to dissipate as heat. In MPPs, the absorption coefficient usually peaks at the resonant frequency and then decreases as it moves further from its peak. The sharpness of the peak and overall profile are the key indicators of the panel's performance.

The configuration of the impedance tube is illustrated in Figure 4.18, while the specific tube used for the tests is shown in Figure 4.17.

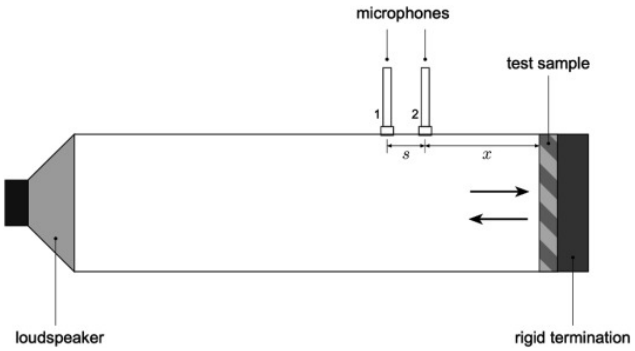

Figure 4.18: Schematic of the Impedance Tube test configuration, taken from Tie et al. [239]

The tube is slightly bigger in diameter, which facilitates the placement of the test sample. The first thing that one must place in the tube is a separation cylinder, of height "D" (cavity distance), which varies between cases. This separation cylinder has to be smaller in diameter than the sample, as it has to be placed on top of it, and thin, as to not cover holes in the sample. Due to the difference in diameter, there is a small gap between the sample and the tube inner wall, as shown in Figure 4.19. To avoid possible issues in the test, modeling clay is used to fill in the gap between the two, also fixing the sample positioning. The clay may slightly cover some of the holes of the test sample, as shown in Figure 4.20, but its effect on its performance is minimal, similar to the difference in results in Figure 4.10, when adapting the values obtained in the optimization process to more realistic values. The area of a hole of 1 mm in diameter represents less than 0.1% of the perforation area of a panel.

4.3.2 Results

Due to complications encountered during the printing process with ULTEM™ support material, as well as the excessive flexibility of the methacrylate plate, the Case 1 models (featuring a 1 mm thickness panel) could not be tested. For the analysis, a linear sweep was conducted, covering a frequency range from 60 Hz to 5 kHz, although the full sweep during testing spanned from 0 Hz to 20 kHz, as shown in Figure 4.22. The results presented show a high level of noise in some of the tests, like case 2 methacrylate panel and the original case 4

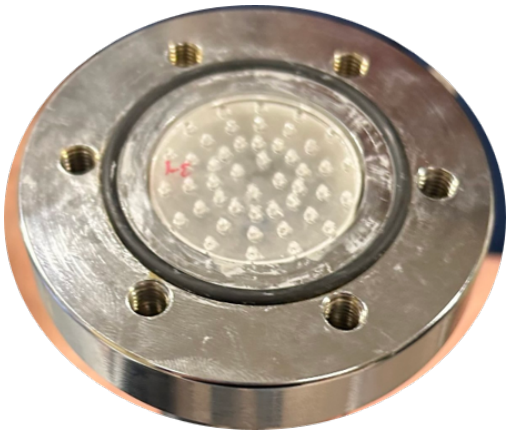

Figure 4.19: Placing of the sample in the tube, without the modeling clay.

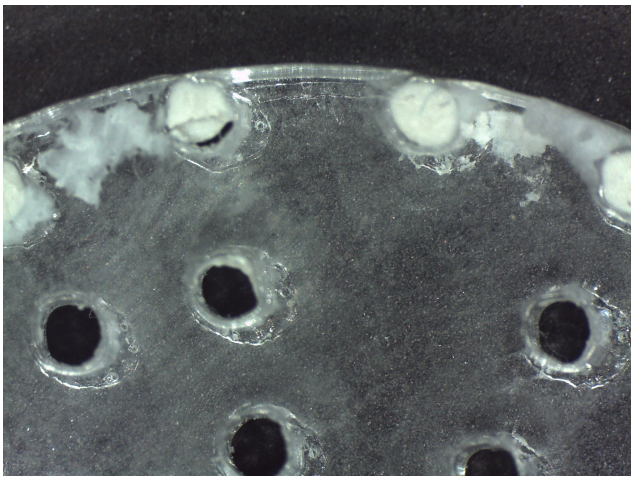

Figure 4.20: Clay covering some of the perforations in one of the samples.

ULTEM™ panel. The results for case 4 were very different in comparison with the rest of the panels tested, as the absorption curve was very low and did not have the typical shape of the curve. For this reason, a second case 4 sample was printed and tested. The absorption coefficient curve comparison is shown in Figure 4.21. As the second panel yielded better results, it will be the one used for further analysis.

The results for the single-panel cases are presented in Figures 4.23 to 4.33. These figures compare the results of different material samples within the same case (in the applied tests) against the theoretical absorption curve. The method used is the Equivalent Fluid Model (EF), as both the Maa model and the EF model obtain nearly identical results. In general, the absorption curves of the different materials do not align with each other, nor do they closely resemble the theoretical curve. Typically, the ULTEM™ samples exhibit their absorption peak earlier than the other materials in the applicable cases, with a lower peak compared to the methacrylate curve. The methacrylate curve, on the other hand, shows a peak further to the right when compared to the theoretical curve.

There are, however, a few cases where the curves for methacrylate and ULTEM™ show some

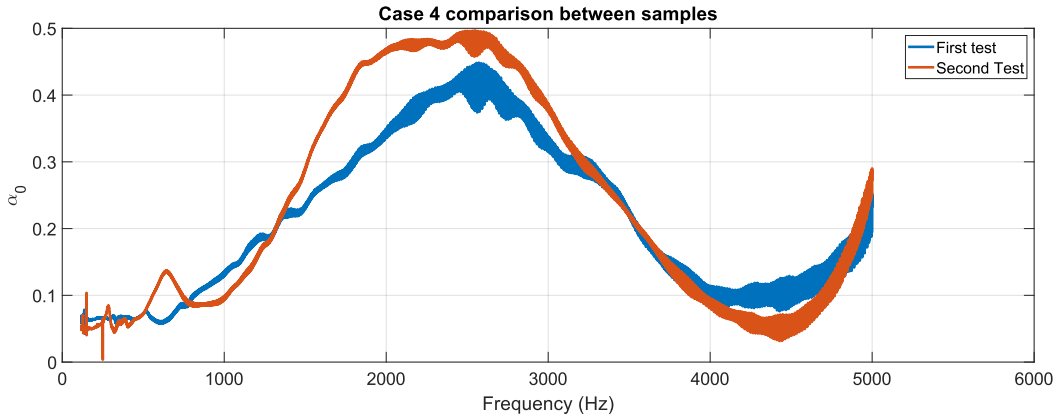

Figure 4.21: Comparison of the two case 4 panels tested.

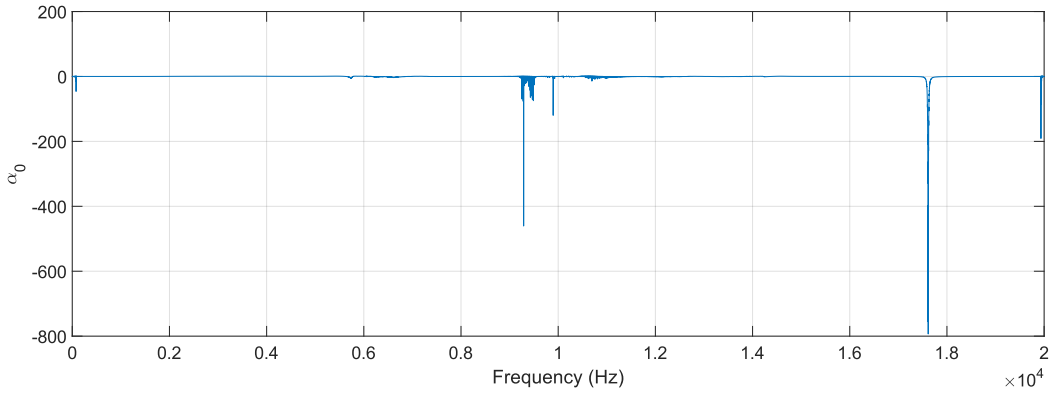

Figure 4.22: Full range of results in the test.

similarity, such as in Figures 4.26, 4.30, 4.32, and 4.33. In these instances, the ULTEM™ curves tend to have a lower but broader peak absorption. The theoretical curves generally exhibit a narrower peak, and except for Case 10 in Figure 4.31, the peaks are positioned similarly to the methacrylate curves.

In certain cases, such as in Cases 7, 8, and 9, the theoretical curves show significantly lower absorption with a broader peak. While most of the theoretical curves feature a single peak, the tested samples display valleys, and in some cases, the curves exhibit behavior typically seen in two-panel configurations, with two distinct peaks. The absorption coefficient curve for microperforated panels tends to have as many peaks as the number of panels in the configuration being tested.

Figure 4.34 and Figure 4.35 illustrate the results obtained for the two-panel and three-panel configurations. In the two-panel configuration, the expected two absorption peaks are observed, though they are shifted in frequency. The first peak is relatively close to the analytical prediction, but the absorption coefficient in the test exceeds that of the analytical solution. The second peak occurs more than 1 kHz later than the predicted second peak, and its absorption coefficient is slightly lower than expected.

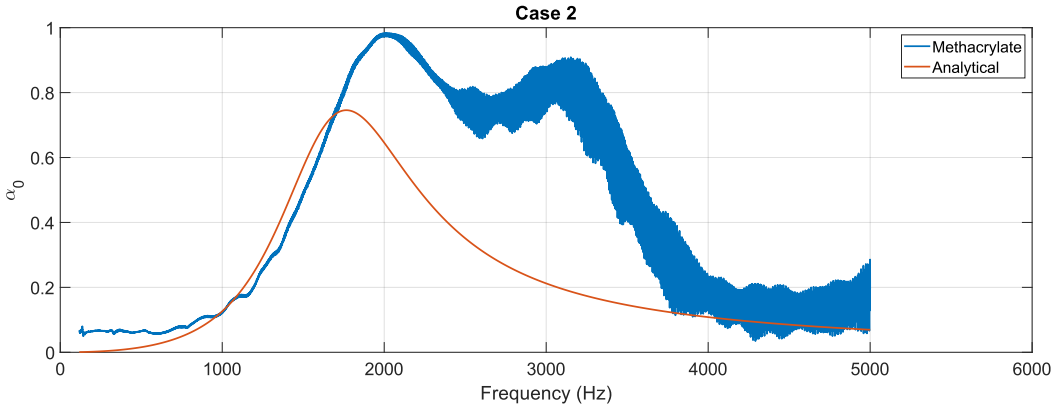

Figure 4.23: Test results of case 2.

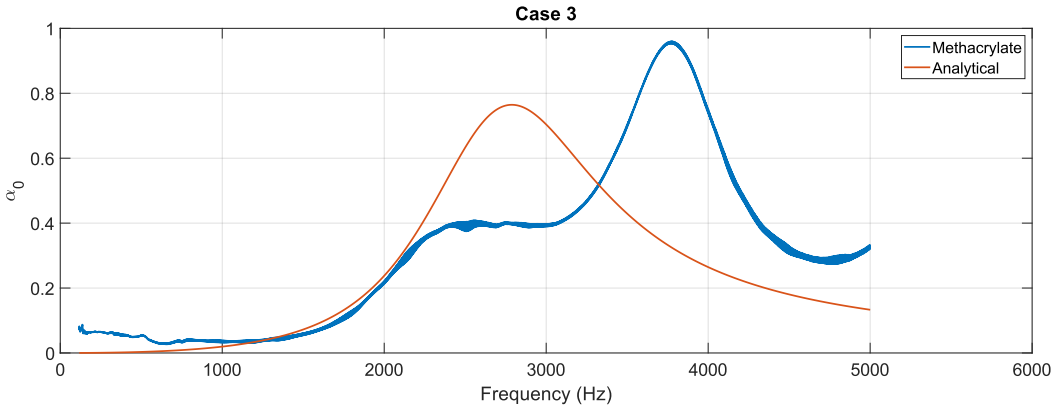

Figure 4.24: Test results of case 3.

For the three-panel configuration, the analysis range was extended to 5.6 kHz, as the third peak appeared later than anticipated based on the analytical absorption curve. Overall, the test results exceed expectations, with a broader average absorption observed across the analyzed frequency range. While the peaks do not align exactly with the analytical predictions, the first peak in the test, similar to the two-panel configuration, is reasonably close to the expected value.

Figures 4.36 to 4.39 are shown to compare the results between cases 7 to 10. These cases were chosen to compare and see how the hole diameter and sample thickness affected the sound absorption coefficient. In Figure 4.36 and Figure 4.37, the test samples have the same nominal hole diameter (1.2 mm for cases 7 and 8; 1 mm for cases 9 and 10), cavity distance and perforation area, only varying the thickness (2 mm in cases 7/9 and 3 mm in case 8/10). In Figures 4.38 and 4.39, the comparison is between the cases with the same thickness (cases 7 and 9, with 2 mm; cases 8 and 10 with 3 mm) but different hole diameter.

In Figures 4.36 and 4.37, we observed that the increase in thickness shifts the absorption peak to the left. In these two case comparisons, the only curves that remain similar are those of the methacrylate samples. For cases 7 and 8, the curve is nearly identical, both having a peak absorption coefficient of 1, while in cases 9 and 10, the absorption peak for case 10 is

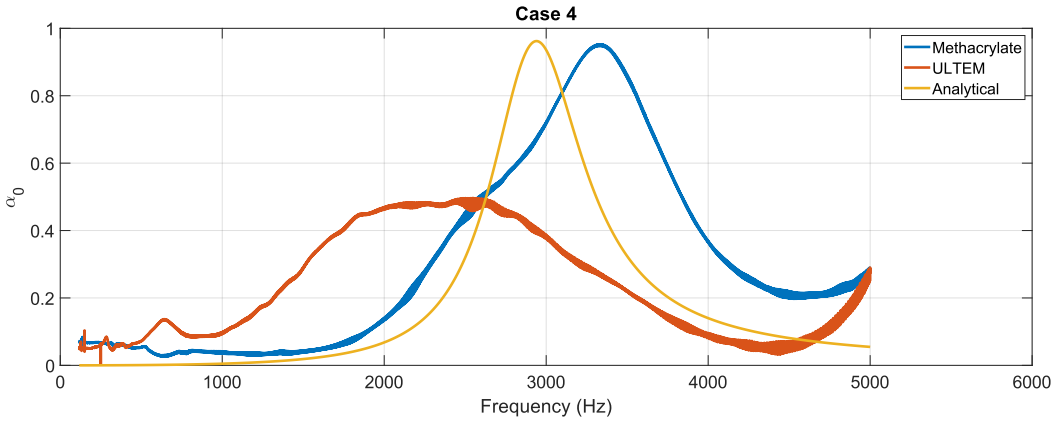

Figure 4.25: Test results of case 4.

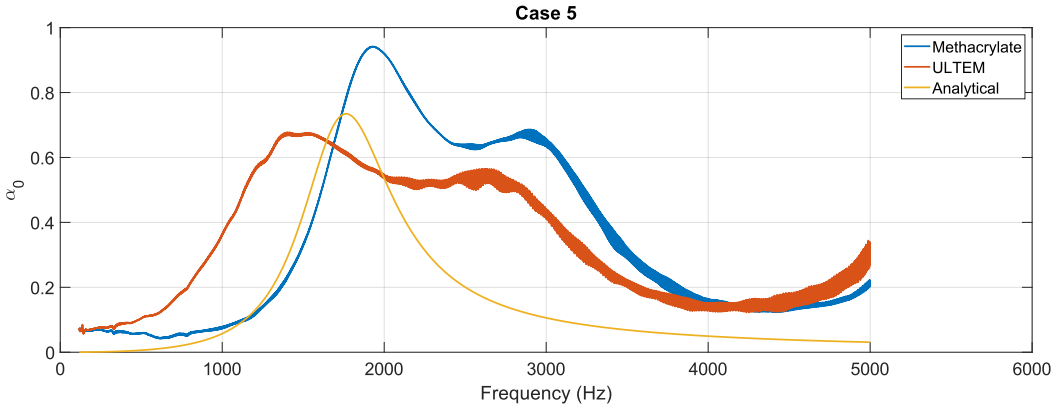

Figure 4.26: Test results of case 5.

broader and lower than case 9. It is interesting to see, in Figure 4.37, that the curves for case 9 in ULTEM™and case 10 in methacrylate, are nearly identical.

In Figures 4.38 and 4.39, we observe that the curves for both methacrylate and ULTEM™ materials show similar trends across the different cases. As the hole diameter decreases, the peak absorption frequency shifts to the right, and the absorption coefficient decreases in three out of the four cases. The only exception is Case 9 with the ULTEM™ sample, where the peak absorption coefficient increases. This sample also displays a unique behavior, with the curve showing a brief, more horizontal valley, unlike the Case 7 curve, which exhibits a more consistent upward trend leading to the peak.

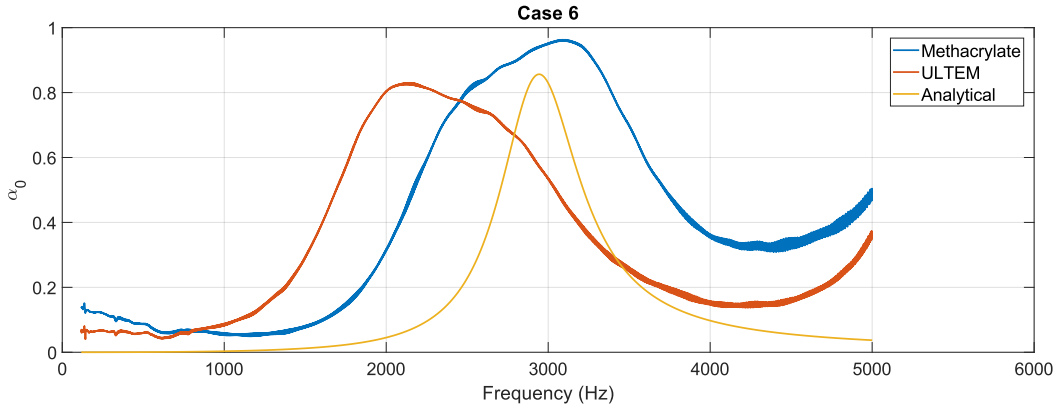

Figure 4.27: Test results of case 6.

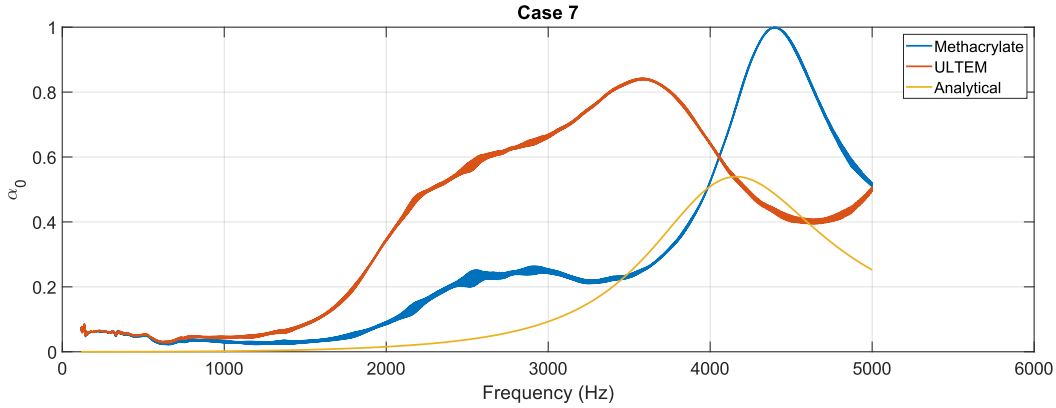

Figure 4.28: Test results of case 7.

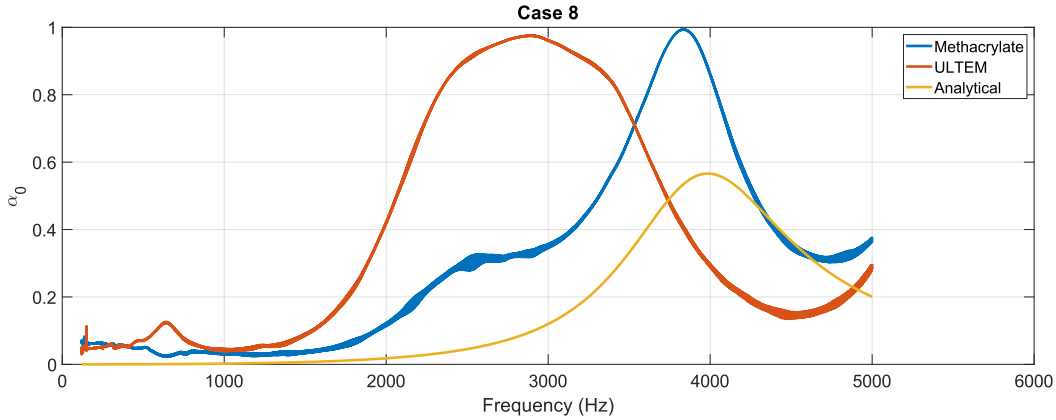

Figure 4.29: Test results of case 8.

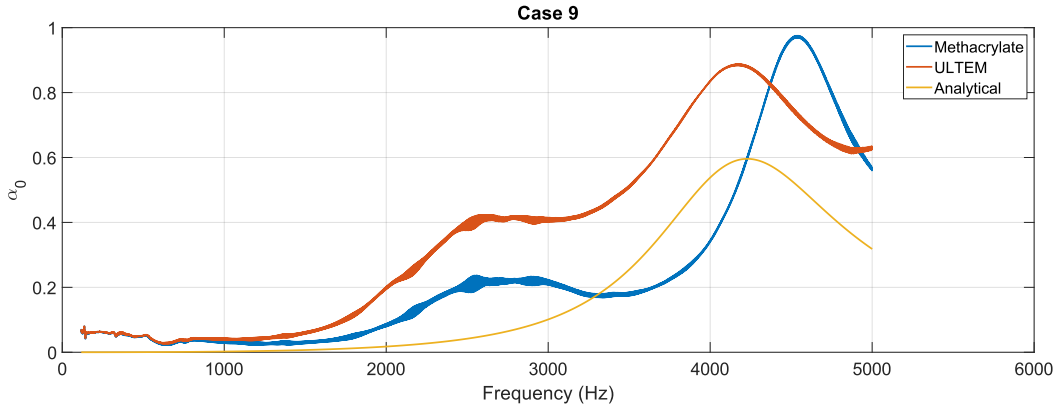

Figure 4.30: Test results of case 9.

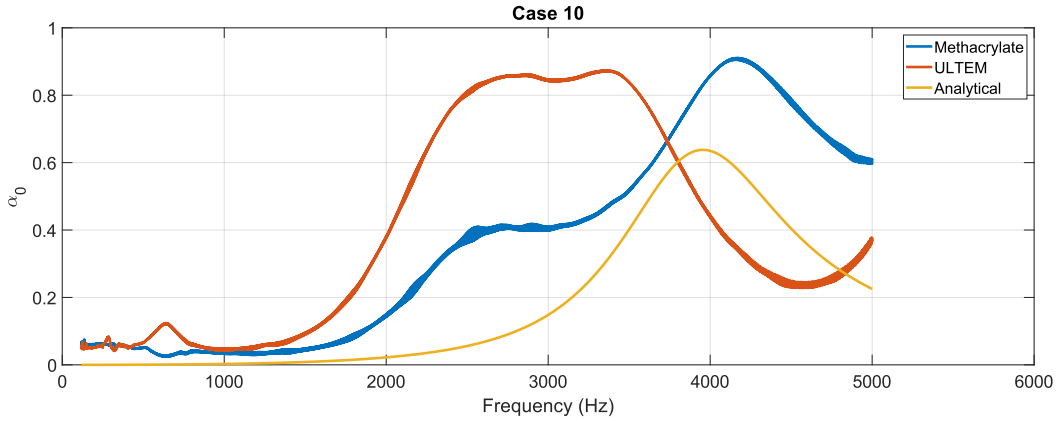

Figure 4.31: Test results of case 10.

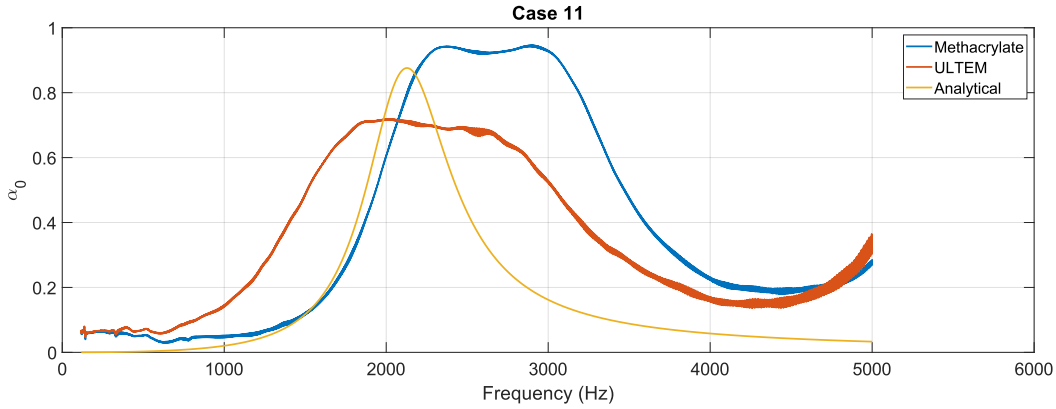

Figure 4.32: Test results of case 11.

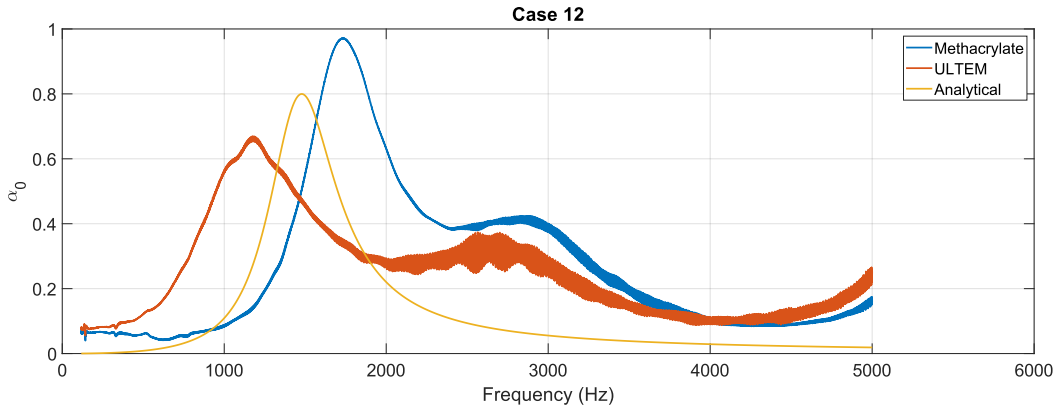

Figure 4.33: Test results of case 12.

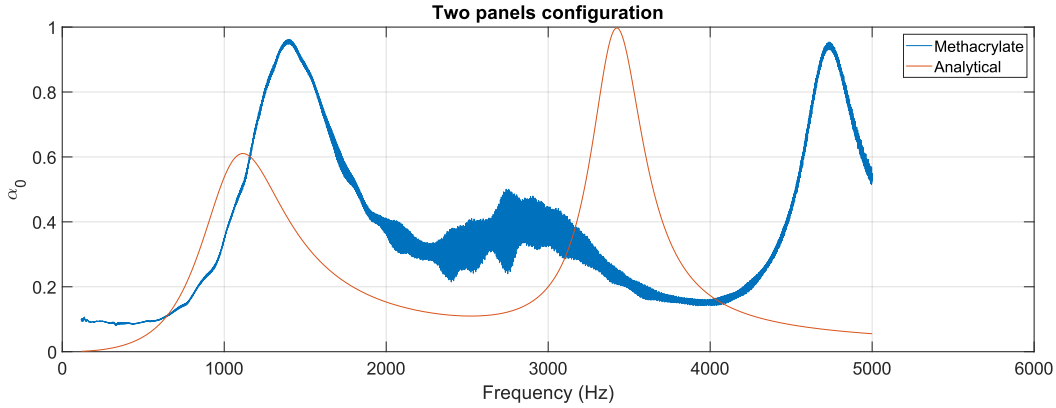

Figure 4.34: Test results for the two panel configuration.

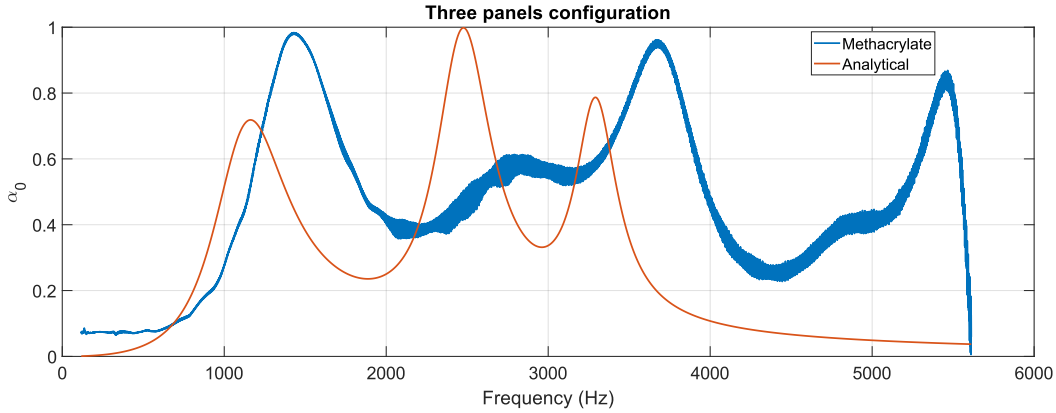

Figure 4.35: Test results for the three panel configuration.

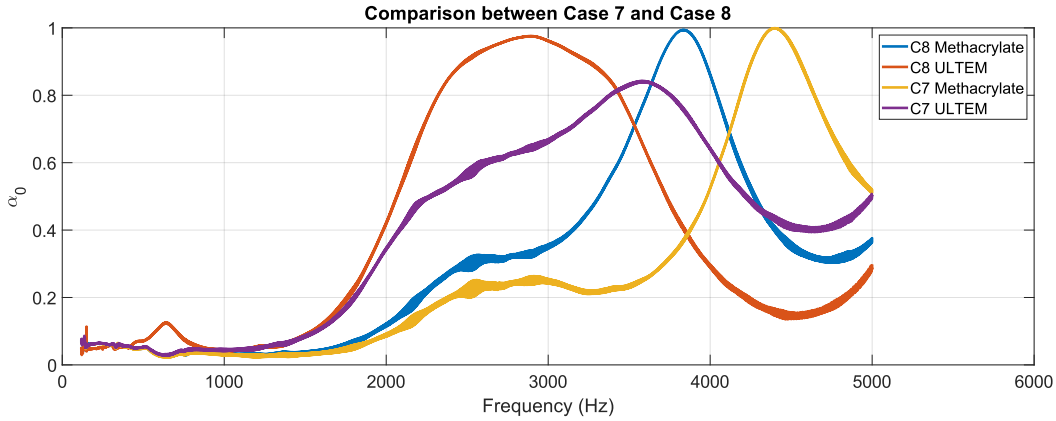

Figure 4.36: Comparison between cases 7 and 8, samples with the same design parameters except thickness.

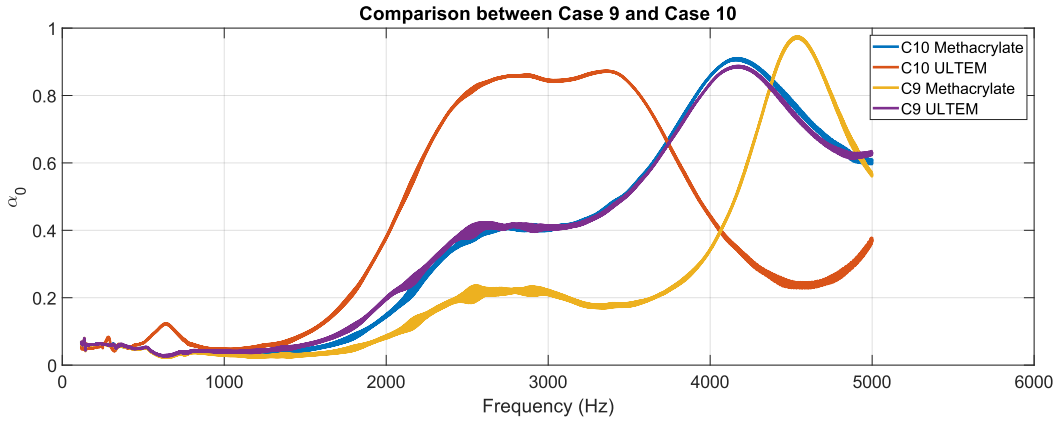

Figure 4.37: Comparison between cases 9 and 10, samples with the same design parameters except thickness.

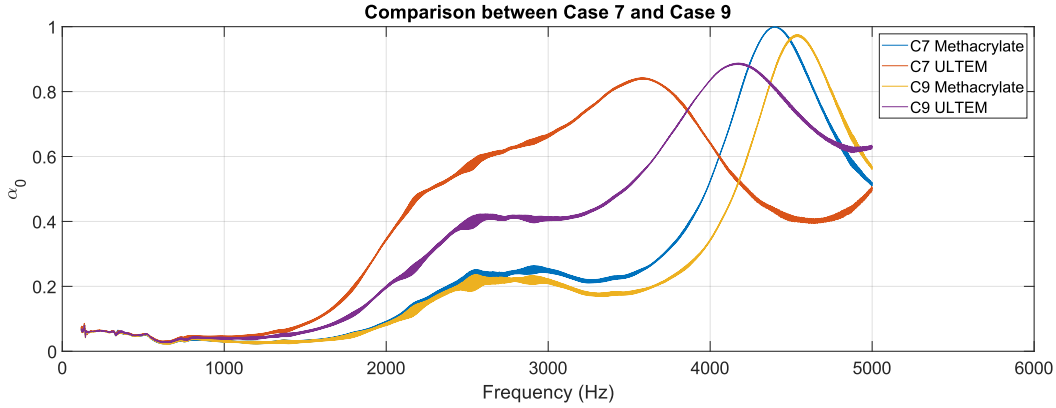

Figure 4.38: Comparison between cases 7 and 9, samples with the same design parameters except hole diameter.

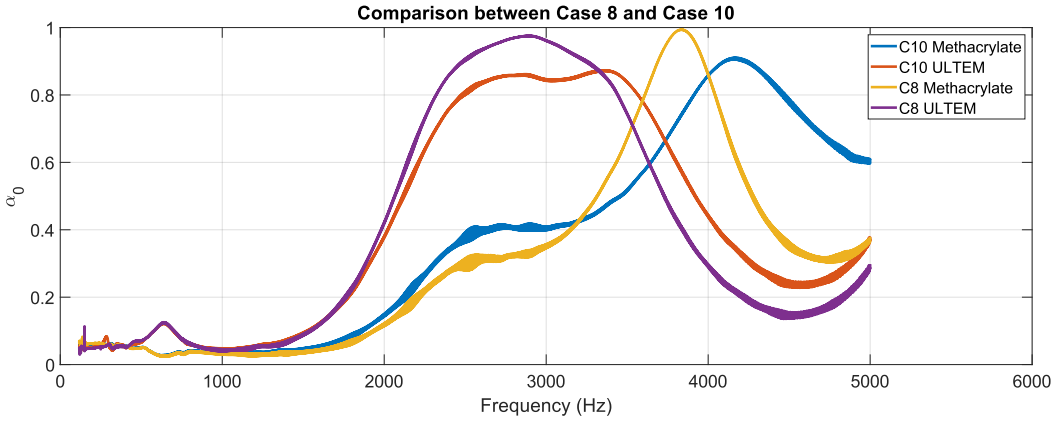

Figure 4.39: Comparison between cases 8 and 10, samples with the same design parameters except hole diameter.

Chapter 5

Discussion

In this chapter, the results from the acoustic tests are thoroughly analyzed and discussed. Building on the initial findings, additional tests are conducted to further investigate the properties of the materials under different conditions. These new tests include verifying the density of the materials to better understand their acoustic behavior and performance. Furthermore, other additive manufacturing methods and materials, which were previously unavailable at the university with high-quality production, are tested and incorporated into the analysis to expand the scope of the study. These supplementary tests aim to provide a more comprehensive understanding of how various materials and manufacturing techniques influence acoustic properties, offering valuable insights for future applications and research.

The chapter is organized into several concise sections, each addressing different issues and challenges that emerged from the acoustic tests. Each section delves into a specific aspect of the results, providing a detailed analysis of the factors that influenced the outcomes.

Defects in the geometry of the perforations

The tube impedance tests reveal a noticeable discrepancy between the theoretical curve and the sample curves, including those made from methacrylate. Given the manufacturing process and the various parameters influencing the curves, the first aspect to investigate is the perforations on the samples. On the thinner methacrylate panels, particularly those with the smallest nominal hole diameters, the perforations are the most irregular. This is evident in Figure 5.1, where the panels, with thicknesses of 2 and 3 mm and hole diameters of 0.6 and 0.8 mm, show pronounced irregularities. Ideally, the laser beam should maintain a cylindrical shape, but in practice, it exhibits divergence as it travels, resulting in a conical shape at greater distances. Another consequence of the irregular perforations can be observed in Figure 5.1b, where a higher perforation percentage (due to a greater number of holes) leads to some of the holes merging near the center of the panel. This occurs because of the circular pattern of the perforations and the reduced spacing between them in that area.

In panels with a thickness greater than 5 mm and a hole diameter of 1 mm, the perforations tend to be more circular. However, other issues arise, as shown in Figure 5.2. In these cases, the laser fails to complete some of the perforations, leaving material bumps within the holes